The hydrodynamic effects on a smaller underwater body in close proximity to a larger moving body

MAT SAAD, Khairul Anuar

National Centre for Maritime Engineering and Hydrodynamics

Australian Maritime College

Submitted in fulfilment of the requirement for

the degree of Doctor of Philosophy

University of Tasmania,

February 2016

Signed Statement

This thesis contains no material which has been accepted for a degree or diploma by the University or any other institution, except by way of the background information and duly acknowledged in the thesis, and to the best of my knowledge and belief no material previously published or written by another except where due acknowledgment is made in the text of the thesis, nor does the thesis contain any material that infringes copyright.

……..

MAT SAAD, Khairul Anuar

February, 2016

Authority of Access

This thesis may be made available for loan and limited copying and communication in accordance with the Copyright Act 1968.

……..

MAT SAAD, Khairul Anuar

February, 2016

Abstract

Today's underwater vehicles are extensively used in the marine, offshore, and defence industries for a range of tasks, including surveillance, intelligence data gathering, and maintenance. The hydrodynamic interactions between underwater vehicles operating in close proximity were investigated to determine the interaction mechanism and quantify the influence of varying parameters on the interaction effects. During their mission, Unmanned Underwater Vehicles (UUVs) are sometimes required to operate in close proximity to larger vehicles or bodies that can create complex flow patterns adversely affecting the smaller vehicle. Due to significant differences in size and speed, the latter is required to navigate through rapidly varying flow and pressure regimes, which can cause it to lose position and trajectory, resulting in mission failure and possible loss of vehicle.

This project investigates these effects through numerical modelling and experimental work. This consists of modelling the behaviour of the smaller vehicle in close proximity to a larger vehicle using Computational Fluid Dynamics (CFD) in order to understand the interaction between the two vehicles under different configurations and conditions. Given that the smaller vehicle is more susceptible to the interaction effects, its behaviour is the focus of this thesis.

The CFD results are validated through captive model scale experimental work in the Australian Maritime College towing tank using the forces and moments on the smaller vehicle due to the interaction. The work further investigates the issues involved in related numerical modelling and experimental techniques, and presents the approaches undertaken to address these issues.

The research focuses on the hydrodynamic characteristics which are pressure distribution and flow regime generated between the two vehicles as they operate in close proximity to identify the behaviour and trajectory of the smaller vehicle. Once the interactions between the underwater vehicles are determined, the magnitudes and trends of the forces and moments action on the smaller vehicle as it moves relative to the larger vehicle are quantified. This enabled the establishment of a safe operational envelop for the smaller UUV to operate around the larger vehicle, including low risk options to approach and depart the latter.

Acknowledgements

Alhamdulillah, with the name of Allah the Most Gracious, Merciful and Almighty and to Muhammad the Prophet of Allah Peace upon Him.

I would like to express my heartiest gratitude to my supervisor Professor Dev Ranmuthugala, Dr Jonathan Duffy and associate supervisor Dr Zhi Leong for their valuable guidance and advice for completing this wonderful project. They inspired me greatly to work on this project. They were willing to motivate and contribute tremendously to the project. I also would like to thank them for showing lots of example that are related to the topics of the project.

Besides, I would like to thank the AMC's Towing Tank staff and Model Development for providing me with a good environment and facilities to complete this project.

Finally, an honourable appreciation goes to my parents and families, friends and staff of Australian Maritime College (AMC) for their understanding and valuable supports in completing this project. Without the help of these people, I would face difficulties while doing this project.

Table of Contents

List of Figures

List of Tables

Nomenclature

B	Beam [m]
C_d	Drag coefficient
C_f	Skin friction coefficient
C_P	Surface pressure coefficient
C_t	Total resistance coefficient
D	Diameter [m] or Drag force [N]
Re	Reynolds number
H	Height from free surface to centre of SUBOFF [m]
H^*	Non-dimensional depth
k	Kinetic energy
L	Length [m]
LOA	Length overall [m]
P	Pressure [Pa]
R_f	Frictional resistance [N]
R_R	Residuary resistance [N]
R_t	Total resistance [N]
S	Surface area [m]
t	Time [s]
u	Velocity in x-direction [m/s]
v	Velocity in y-direction, or Overall velocity [m/s]
w	Velocity in z-direction [m/s]
y	Distance from the wall [m]

y^+	Dimensionless first node height
z	Height from datum point [m]
ε	Energy dissipation
μ	Dynamic (absolute) viscosity [kg/ms]
ρ	Density [kg/m]
ν	Kinematic viscosity [m/s]
τ	Shear stress [N/m]
ω	Energy frequency Ö
x	Longitudinal distance from datum point [m]
x^+	Dimensionless first node length
F	Force
M	Moment
C_F	Force coefficient
C_M	Moment coefficient

Abbreviations

AMC	Australian Maritime College
AUV	Autonomous Underwater Vehicles
AMECRC	Australian Maritime Engineering Cooperative Research Centre
BMT	BMT Design and Technology Pty Ltd
BSLRSM	Baseline Reynolds Stress Model
CFD	Computational Fluid Dynamics
DARPA	Defense Advanced Research Projects Agency
DOF	Degree of Freedom
DSTO	Defence Science and Technology Organisation
DTRC	David Taylor Research Center
EFD	Experimental Fluid Dynamics
FFT	Fast Fourier Transform
HPMM	Horizontal Planar Motion Mechanism
ITTC	International Towing Tank Conference
PMM	Planar Motion Mechanism
LES	Large Eddy Simulation
RANS	Reynolds Averaged Navier-Stokes
ROV	Remotely Operated Vehicles
SST	Shear Stress Transport
UUV	Unmanned Underwater Vehicles

Co-ordinate System

The co-ordinate system used in the present study is shown in Figure 0.1, unless stated otherwise. The origin is situated at midships of the submarine.

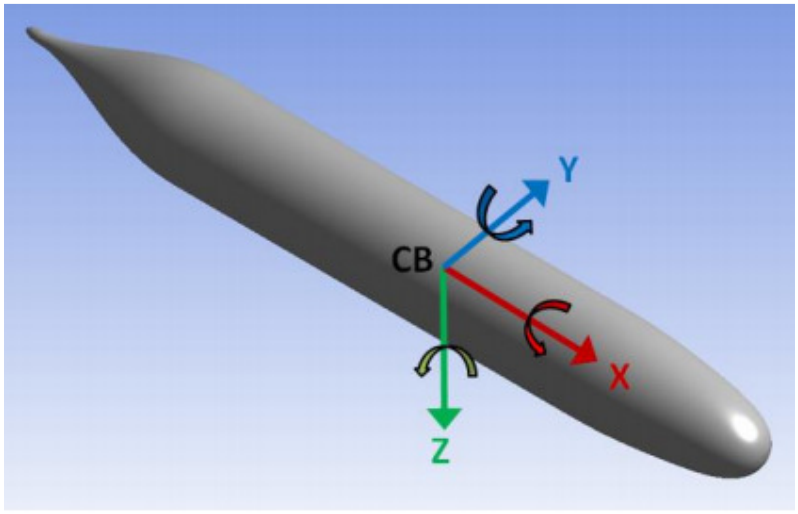

Figure 0.1: Co-ordinate system of the vehicle.

Chapter 1

Introduction

1.1 Background

Today's Unmanned Underwater Vehicles (UUV) are extensively used in the marine, offshore, and defence industries for a range of tasks, including surveillance, data gathering, operational, and maintenance activities. They may vary from simple, shallow water Remotely Operated Vehicles (ROV) to highly complex Autonomous Underwater Vehicles (AUV) which are able to carry out complicated tasks at extreme depths with predetermined mission plans and no real-time user intervention.

When a UUV is operating in close proximity to a larger underwater vehicle or surface ship, interaction with the complex flow patterns generated from the latter can potentially affect the ability of the UUV to maintain its trajectory (refer to Figure 1.1), which may result in mission failure including collision between the vehicles (Bacon Jr., 1995). As the smaller vehicle travels along the length of the larger vehicle, the flow around the hulls change, thus continuously varying the forces (surge, sway, and heave) and moments (roll, pitch, and yaw) action on the vehicles. Although the variations in these forces and moments usually do not affect the motion of the larger vehicle, they can be of sufficient magnitude to cause the smaller vehicle to deviate from its desired trajectory. These issues are significantly exacerbated if the small vehicle is launched or recovered from the larger vehicle (Fonfach, 2010). Thus, it is important that the vehicle is designed to deal with these variations and maintain its trajectory within acceptable thresholds. This includes designing the vehicle to be hydro-dynamically stable under these varying conditions and to develop an appropriate manoeuvring control system that is sufficiently robust and responsive to deal with external influences.

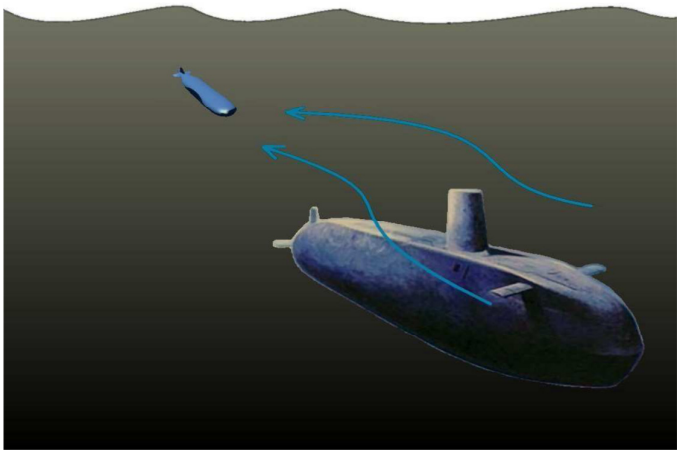

Figure 1.1: Underwater bodies manoeuvring in the vicinity of a moving submarine. (Bacon Jr., 1995).

Through Computational Fluid Dynamics (CFD) and Experimental Fluid Dynamics (EFD) it is possible to predict a vehicle's hydrodynamic characteristics, including its hydrodynamic derivatives and the effects of interaction between vehicles. This information can be used to optimise the vehicle design to achieve the required objectives (Husaini et al. 2009 and Jagadeesh, 2011), by tailoring the vehicle to meet specific operational requirements and to identify safe operational envelop for the vehicle. It also enables the path of vehicle to be numerically modelled to develop and tune the control system in order to improve the manoeuvring performance of the vehicle.

The Defence, Science and Technology Organisation (DSTO), together with the Australian Maritime College (AMC), are currently evaluating the hydrodynamics of AUV, ROV, and submarine platforms in an effort to develop their mission capabilities in the field and meet the requirements of the Royal Australian Navy. A series of numerical and experimental work has been carried out on DSTO and AMC owned underwater vehicles and representative models (Fitzgerald, 2009, Van Steel, 2010, Leong, 2011 and Neulist 2011) to identify their hydrodynamics characteristics. However, only few works have been carried out to investigate the interaction between two underwater vehicles. In addition, not much information is available in the public domain dealing with this topic.

1.2 Problem Definition and Aims

Launch and recovery of UUVs from a submerged host vehicle represents an opportunity to add flexibility to the vehicle's mission, but adds complexity to its design and operation. The ability of a submerged host vehicle, to deploy a ROV or AUV to a targeted mission location with minimum deviation offers unique advantages in mission duration, real time interrogation, and covert mission accomplishment. The ability to adequately control a vehicle as it transits from the submarine launch way to a point away from the host and back until finally rehoused represents a complex dynamics process. Usually the design of a directionally stable vehicle requires numerical modelling and experimental testing to investigate the forces, moments, and trajectory of the vehicle during the course of its mission and through the launch and recovery operations. The process is further complicated when the vehicle has to manoeuvre close to the larger host vehicle, within the wake region and high and low pressure field created by the host vehicle (Fedor, 2009).

The aim of this project is to understand the hydrodynamic characteristics of a UUV operating in close proximity to a larger vehicle such as a submarine or a larger underwater vehicle (Fortson, 1969, King, 1977 and Fedor, 2009). The work is carried out through numerical modelling using the commercial CFD software ANSYS-CFX to quantify the flow and pressure regime in the interaction zone and to predict the behaviour of a UUV when operating within this regime. The CFD results are validated and supplemented through captive model testing conducted in AMC's Towing Tank using scaled physical models of a UUV operating in close proximity to a larger underwater vehicle.

It is essential to understand and attempt to optimise the AUV design for the interaction flow field generated by calculating the pressure distribution upon the marine vehicle. A key advantage of CFD is that the operators are able to evaluate the hydrodynamic performance of a wide range of designs and scenarios numerically without the time, expense, and disruption required to make actual changes onsite or on physical models (Prestero, 2001, Griffin, 2002, Geisbert, 2007, Fedor, 2009 and Fonfach, 2010). CFD uses numerical methods to solve the fundamental non-linear

differential equations that describe fluid flow for predefined geometries and boundary conditions. The simulation can also be used to establish a safe operating envelop for close proximity operations and closer examination of the flow characteristics around the AUV.

However, one of the major challenges faced when using CFD as an analysis tool for hydrodynamics is that the computational results can vary greatly depending on the experience of the analyst, the settings utilised such as the boundary condition and the turbulence models, and the quality of the mesh model; thus necessitating validation through experimental or full scale data.

The numerical results of this study were validated using captive experimental testing of the two vehicles, with the validated model used to investigate a wider range of large to small vehicle diameter ratios and operational conditions, including different longitudinal and lateral positions of the small vehicle with respect to the larger vehicle. The CFD and EFD data was also used to identify safe trajectory pathways for a small AUV travelling in close proximity to a larger vehicle.

1.3 Research Objectives

The main objective of this research project was to improve the understanding of the hydrodynamic interaction forces and moment on a UUV operating in close proximity to a larger submerged vehicle in order to identify a safe operational envelop. This includes investigating:

- the flow pattern and pressure distribution on the smaller unmanned vehicle with a focus on the interaction drag force, side force, and yaw moment at varying lateral separations, longitudinal separations, and forward speeds (both vehicles moving at the same forward speed);
- the effects of varying the larger vehicle to smaller vehicle diameter ratio under the above conditions; and

- the identification of a safe operational trajectory and envelop for the smaller vehicle when operating close to the larger vehicle.

1.4 Description of Vehicles, Geometries and Models

Two models were used to perform the tests; the small vehicle (SUBOFF) and the larger vehicle (Larger Submarine Body). The smaller AUV was represented by the SUBOFF geometry that was specially developed for the AMC Towing Tank to be used in conjunction with the Horizontal Planar Motion Mechanism (HPMM), with the load balance located within the body. For the experimental work of this study, the diameter of each hull was limited by the Towing Tank dimensions. For example, the models must be sufficiently large to accommodate the required force balances and provide sufficient force and moment magnitudes to record sensible data, while being sufficiently small to fit within the Towing Tank without causing blockage or encroaching into the boundary layer regions of the tank. Due to the constraints imposed by the Towing Tank dimensions the larger body diameter was limited to 2.23 times the diameter of the smaller body. The diameter ratio of 2.23 between the vehicles is relatively low for a study, focusing on the flow and pressure regime around the larger body and its effects of the smaller AUV/ROV. Although the smaller diameter ratio reduces the dominance of the larger vehicle on the flow and pressure regime and the resulting behaviour of the smaller AUV/ROV, the results enable the CFD model to be validated while providing an insight into the trends as the speeds and longitudinal/lateral separations are varied. The description of each model is discussed below.

The SUBOFF hull used as the smaller AUV model has a diameter of 0.18m, and a length of 1.44m giving a length to diameter (L/D) ratio of 8. Initial CFD work was carried out using a larger body having a diameter ratio of 2.23:1 in comparison to the SUBOFF geometry thus providing sufficient difference between the sizes of the vehicles enabling the study to focus on quantifying the flow and pressure regime around the larger body and its effects of the smaller AUV/ROV. The study schedule will increase the vehicle diameter ratio to 12:1 once the CFD code is validated via the

experimental work, thus representing scenarios such as the interaction of an AUV with a submarine.

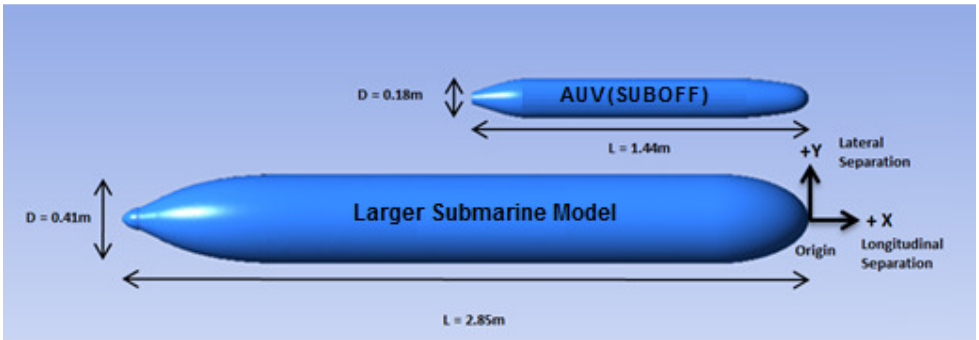

Figure 1.2: Illustration of the arrangement for EFD and CFD simulations.

1.5 Methodology

In order to understand the interaction between underwater vehicles and identify a suitable operational envelop for the smaller vehicle, the project was divided into the following phases, comprising the numerical, experimental, and the analysis phases. The first two phases were carried out in parallel, as their results were used to verify, validate, and supplement the two phases. For all cases investigated, the configuration ensured no vertical offset existed between the vehicles, as both vehicles were on the same horizontal plane.

Phase 1: Numerical Modelling

The numerical CFD modelling was carried out using ANSYS-CFX software Version 14 and consisted of a number of stages. Initially the two geometries were modelled separately to be verified and validated against physical experiment results. This was followed by the tandem modelling of the two geometries at a large to small vehicle diameter ratio of 2.23:1, which was the largest ratio that could be replicated in the tow tank experiments for validation due to the dimensions of the test facility. The modelling was carried out at a number of speeds and relative longitudinal and lateral distances between the vehicles (refer to Table 1.1). This has provided information on

the interaction forces and moments action on the vehicles at different positions and speeds, as well as providing flow visualisation data to assist in interpreting the results.

Table 1.1: The parameters used for the testing configuration at model scale and 2.23:1 diameter ratio.

Parameters	Units	Descriptions
Speed	m/s	0.25,0.5,0.85,1.0,and 1.2
Reynolds Number (x10^5)	-	4.04, 8.08, 13.74, 6.16, and 19.39
Lateral Separation Ratio	-	2.68, 3.03, 3.38, and 4.09
Longitudinal Separation Ratio	-	-0.26, -0.18, 0.02, 0.16
Hydrodynamics Forces	N	Drag Force and Sway Force
Moment	Nm	Yaw Moment

The validated CFD model was then extended to a large to small vehicle diameter ratio of 12:1 in order to quantify the interaction effects on a typical AUV operating in close proximity to a submarine.

Phase 2: Physical Experiment Tests

The physical experiment phase initially concentrated on the smaller vehicle geometry in order to validate the numerical model. This was followed by experiments involving the two vehicles in tandem at different longitudinal and lateral locations (refer to Figure 1.2) and a range of forward speeds, with the results used to validate and supplement the numerical results. The diameter ratio between the vehicles were restricted to 2.23:1, as the larger vehicle model was limited by the tow tank dimensions, while the smaller vehicle had to be sufficiently large to incorporate an internal force balance with sufficient magnitude and sensitivity to record sensible data across the experimental speed range. The experiments provided force and moment data on the smaller vehicle for different relative locations and various forward speeds. The experiments were repeated to identify error limits and repeatability effects.

Phase 3: Analysis

The data from CFD and EFD were analysed at the diameter ratio of 2.23:1 to quantify the interaction effects at different longitudinal and lateral separation distances, and the influence of forward speed on these forces and moments. This enabled the

identification of relative locations along the larger vehicle that provides the least disruption to the trajectory of the smaller vehicle, and thus a safe operational envelop for the vehicle.

The CFD results of the 12:1 diameter ratio simulations were then used to extend the study to replicate the operation of a typical AUV operating in close proximity to a submarine, again providing a guide for a safe operational trajectory and envelop.

1.6 Novel Aspects of the Research

The main objectives of this project were identifying the behaviour of a UUV operating in close proximity to a larger underwater body and to develop a safety envelop for the UUV. The novel components of the work and contributions to the knowledge in the field of underwater vehicle hydrodynamics and UUV manoeuvring include:

- a comprehensive set of numerical modelling which was conducted for a range of large to small vehicle diameter ratios, vehicle speeds, and relative positions (lateral and longitudinal separations); enhancing the understanding of interaction between two dissimilar sized underwater vehicles operating in close proximity. There is currently minimal data available in this area within the public domain.
- captive model scale experiments of two dissimilar sized underwater vehicles in the AMC Towing Tank to validate the numerical models for a wide range of cases (longitudinal and lateral separations and speed), and experimental data is currently lacking within the public domain, thus contributing to the knowledge within this area.
- numerical and experimental work to identify a safe operational envelop for a UUV operating in close proximity to a larger underwater vehicle.

1.7 Outline of Thesis

Research work completed in the past three years has been divided into chapters and is presented sequentially in this thesis.

A review of previous works on the prediction of interaction between underwater vehicles, hydrodynamic modelling using numerical methods, experimental work and hydrodynamics interaction between surface ships are given in Chapter 2.

Chapter 3 discusses the methods used in the testing. First, a detailed explanation of the experimental setup is given. This includes how the model was setup and positioned in the tow tank as well as the arrangement of the Horizontal Planar Motion Mechanism (HPMM), and testing equipment. Next, the test procedure is discussed followed by the steps necessary to reduce the data and perform drag, side, and yaw moment calculations on the model.

Chapter 4 outlines the (CFD) analysis that was undertaken during this project. This section covers the simulation setup, grid independence study and basic modelling methods undertaken during this project.

Chapter 5 presents the results of the study. Figures are presented that show the flow profiles around the vehicles for the test cases that were performed. Then the results of the drag and lift are shown and discussed.

Chapter 6 summarizes the study and formulates conclusions and recommendation based on the results in Chapter 5.

Chapter 2

Literature Review

The phenomenon of hydrodynamic interaction between surface ships is a subject of several research works. The interest to study the interaction problem started around the mid to late 1900s (Yung, 1978, Cheung, 1987 and Kazi 1995). However, research into the hydrodynamics of close proximity operations of underwater vehicles is limited within the public domain, let alone the manoeuvring characteristics of small vehicles such as ROV's or AUV's in close proximity to a larger underwater vehicle.

This chapter outlines the findings of relevant studies on the hydrodynamic interaction between underwater vehicles, the methods to investigate and quantify the interaction, and also a brief overview of the interaction behaviour between surface ships due to the limited number of such studies for underwater vehicles.

2.1 Interaction between Underwater Vehicles

Two solid bodies approaching each other in fluid are not rare in nature. Situations where two submerged bodies operate in close proximity to each other can be found in military application, such as when a torpedo is launched from a submarine (refer to Figure 2.1) or when an unmanned underwater vehicle operates close to another underwater vehicle (refer to Figure 2.2).

When an AUV is operating in close proximity to a larger vehicle, interaction with the complex flow patterns generated from the latter can potentially affect the ability of the AUV to maintain its trajectory, which may result in mission failure including collision between the vehicles.

The manoeuvrability and stability of a submarine, as well as the ability to compensate for disturbance depend on the hydrodynamics forces generated by the control surfaces. Underwater vehicles are frequently unstable (Barlow et al. 1999) and would be unusable without active operation of the control surfaces.

Figure 2.1: A torpedo launched from a submarine. (Bacon, 2010).

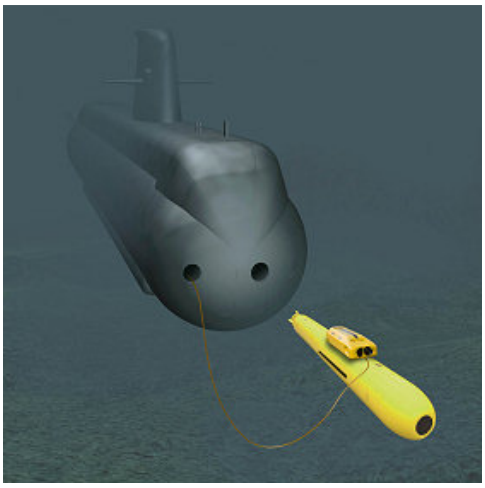

Figure 2.2: Recovery of a ROV via a submarine.
(ROV-Online, 2008).

2.2 Hydrodynamic Modelling Using Numerical Methods

A key advantage of numerical methods is that it is a non-intrusive virtual modelling technique that allows operators to evaluate the performance of a wide range of designs and scenarios numerically without the time, expense, and disruption required to make actual changes onsite or on physical models (Widjaja et al. 2007 and Tu et al. 2008). For the prediction of the interaction behaviour between underwater vehicles, the numerical model must be able to account for the viscous flow near the body, the potential flow away from the body, the three dimensional geometry effects on the flow, as well as the body to body interactions in order to accurately predict the forces and moment action on the submerged vehicles due to the interaction.

2.2.1 Hydrodynamic Interaction between Underwater Vehicles

Riggle (1996) used a combination of potential flow and empirical models to examine the trajectory effect of launch and recovery of a UUV from a mother (host) vessel. Figure 2.3 shows the basic configuration and geometry associated with a UUV and the host vessel. Four types of launching methods were investigated; straight launch, launch with yaw manoeuvre, launch with yaw and deceleration manoeuvre, and straight launch at zero speed. Data was obtained for the forces and moments at various points of advance along the launchway centreline. The vehicle was advanced from a position farthest aft, corresponds to the aft end of the propulsor duct flush with the forward edge of the guide to position 10 inches forward of this reference (100 inches full scale). This range of transverse starts with the vehicle fully within the launchway and extends to a position with the aft end of the propulsor duct approximately even with the forward most point of the launchway. From the comparison of trajectory runs, it is clear that the forces and moment model implemented into a six degree of freedom motion algorithm can solve control forces versus time for any desired trajectory. Host vessel speed effects are incorporated. The smoothing technique account for the inevitable mismatch between the experimentally derived interaction models to the parametric coefficient based on hydrodynamic forces in open water and allows for geometrically similar models to be tested using

the existing experimental result. However, it is important to note that this solution is specific to the launchway environment and experiments which need to be repeated for the empirical model if the UUV is located elsewhere around the mothership. Furthermore, potential flow methods tend to over predict the pressure recovery at the stern of the vehicle due to the negligence of viscous effects. Therefore, numerical approaches using CFD will be the focus for the remainder of this chapter.

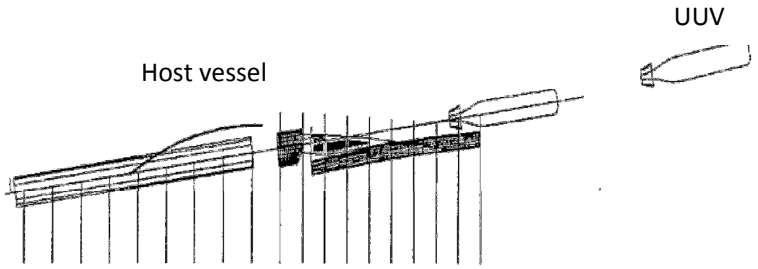

Figure 2.3: Basic configuration of a UUV and the host vessel. (Riggle, 1996).

Fedor (2009) performed three-dimensional steady state CFD simulations to determine a feasible position around a submarine for a recovery system of a UUV (refer to Figure 2.4). Based on the force predictions and flow visualisation of the flow pressure and vortices around the submarine, Fedor found that the position that was beside the sail contributes the least disturbance and wake compared to the other positions.

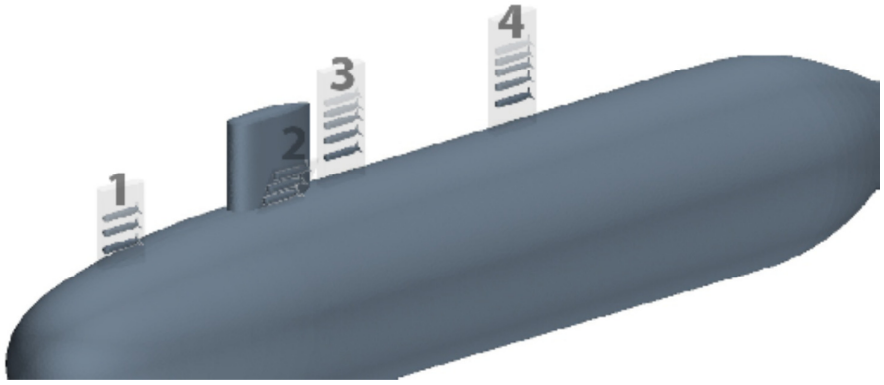

Figure 2.4: The position on the submarine where recovery UUV simulations. (Fedor, 2009).

Husaini et al. (2009) and Jagadeesh (2011) used two-dimensional (2-D) steady state CFD simulations to investigate the drag force around multiple AUVs in different cooperative configurations as shown in Figure 2.5. The inline configuration in their studies was found to offer the least drag on the vehicle.

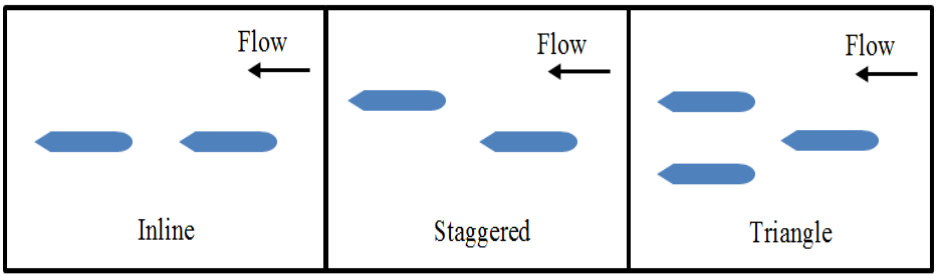

Figure 2.5: Cooperative configurations. Muhamad et al. (2009) and Jagadeesh (2011).

While Fedor (2009), Husaini et al. (2009) and Jagadeesh (2011) offer an insight into the interaction effects between underwater vehicles, the parameters surrounding the broader extent of the interaction behaviour are not discussed or characterised (relative position, relative size, and relative speed). Fedor's investigation focused on very limited locations close to the submarine, thus the means for the AUV to approach the regions investigated were not discussed and the behaviour of the AUV at other positions relative to the submarine are not characterised. The studies by Husaini et al. and Jagadeesh focus on underwater vehicles of the same size and 2-D in nature; thus the magnitude of the interaction forces and moments on an AUV in proximity to a larger vehicle such as a submarine were not established and only findings on the relative trends between the cooperative configurations can be drawn. Furthermore, their studies were purely simulation-based, thus lacking experimental data to validate the predictions of the numerical models.

2.2.2 Hydrodynamic Characteristics of Underwater Vehicles

Through Computational Fluid Dynamics (CFD) and Experimental Fluid Dynamics (EFD), it is possible to predict a vehicle's hydrodynamic characteristics including its hydrodynamic derivatives, which in turn can be used to model, develop, and upgrade

the manoeuvring performance of the vehicle. The CFD and EFD data also enables the designer to optimise the vehicle design to achieve the required objectives.

Based on the force predictions and flow visualisation of the flow pressure and vortices around the vessels using CFD, Fedor (2009) found that fore region of the submarine sail offers the least disturbance compared to the other region around the submarine. However, in order to develop the control algorithm for the vehicle, it is important to develop a six degree-of-freedom (6-DOF) model that can capture the hydrodynamics of a UUV in relative motion to another vessel, hence requiring three-dimensional (3-D) model within a dynamic environment.

Leong (2012) showed that CFD is able to predict the forces and moments action on an underwater vehicle in motion, with the predictions well within experimental measurements. Among the various flow model used, RANS-based simulations using the Baseline Reynolds Stress Model (BSLRSM) have shown to offer good agreement with experimental measurements with substantial lower simulation time and cost compared to Large Eddy Simulations (LES). Thus, this thesis aims to evaluate the performance of BSLRSM in capturing hydrodynamic interaction effects between underwater vehicles.

An important factor to achieve accurate Computational Fluid Dynamics (CFD) results is the generation of the mesh. It is with the mesh that the geometry of the simulation is defined and at each node within the mesh that each equation is solved. As discussed in Widjaja et al. (2007) and Tu et al. (2008) a good quality mesh must have sufficient mesh density to capture the boundary layers and flow features. There are two meshing techniques most commonly used in CFD i.e. structured mesh (hexahedra elements) and unstructured mesh (tetrahedral elements). Although structured meshing is often considered more accurate, Lou et al. (2000) states that the unstructured meshing technique is becoming more accepted with the inclusion on inflation theories, which form the basis of the meshing approach used in this study.

Bull (1996) states that a variety of validation techniques must be investigated to ensure all hydrodynamic characteristics and flow structures are accurately

represented. Bull recommends comparing the CFD and experimental results for the following parameters:

- drag coefficent (C_d or C_t);
- pressure coefficient (C_p);
- skin friction coefficent (C_f);
- boundary layer profiles of axial velocity; and
- wake harmonics.

Bull (1996) also suggests that validation between CFD and experimental results for underwater vehicles should begin with C_d or C_t as it is the most stable of the coefficients. The C_f should be compared last as it is the least stable and therefore the most difficult parameter to replicate. Figure 2.6 shows the comparison of C_p and C_f against experimental data. The CFD predictions are represented as solid lines and the experimental data as symbols. It is noted that the C_p (left) correlates quite well with the experimental data with small exceptions at the forward end of the hull. The C_f (right) shows slight deviations throughout with the largest error at the tail end.

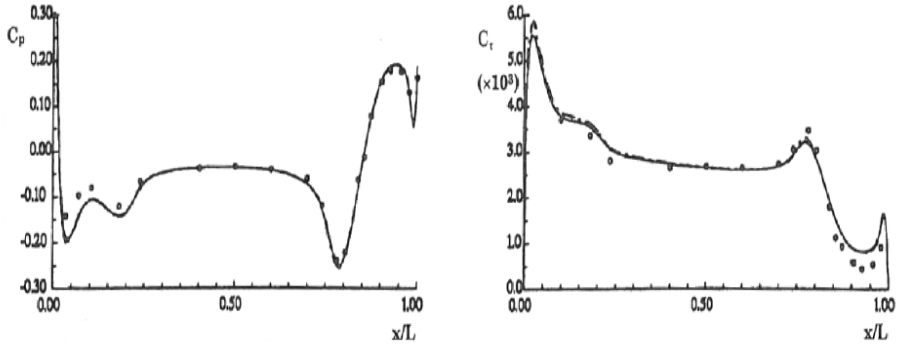

Figure 2.6: C_p (left) & C_f (right) along the SUBOFF hull at Re = 1.2E+07. (Bull, 1996).

Moinuddin et al. (2004) conducted CFD simulations on the turbulent flow around an external corner of a square member to investigate the degree to which the CFD predicted skin friction coefficient (C_f) replicated the experimental data. Initially, poor correlation between the two was found. However, through further mesh refinement

and the use of various turbulence models and techniques, reduced the difference between CFD and experimental data was reduced at various locations along the model between 5.3% and 9.7%. It was found that the CFD over predicted the C_f in comparison to experimental results over the entire length of the body. It was concluded that the C_f distribution obtained through CFD was in reasonable agreement with the experimental data and the percentage difference between the two is a function of errors within the wall boundary conditions and experimental uncertainty.

Widjaja et al. (2007) also found a similar correlation when comparing the coefficients predicted through CFD with those found experimentally. Figure 2.7 shows Widjaja's comparison of C_p and C_f against experimental data. The C_p (left) shows a very good comparison while the C_f (right) shows slight deviations, similar to that discovered by Bull (1996).

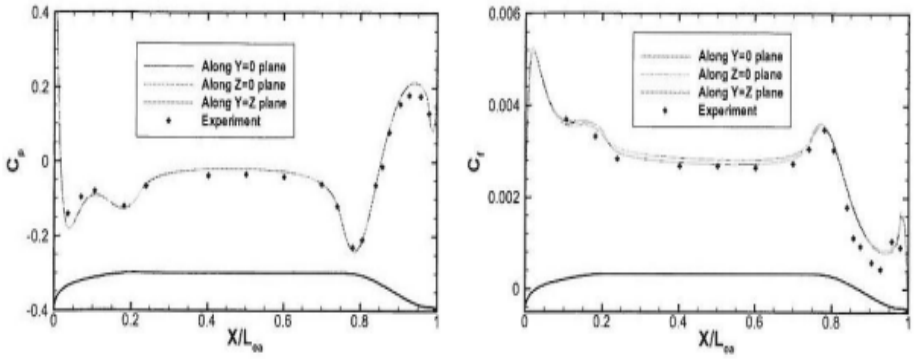

Figure 2.7: C_p (left) & C_f (right) along the SUBOFF hull at Re = 1.2E+07. (Widjaja, 2007).

Fell (2009) compared the CFD predicted pressure and skin friction coefficients with experimental data for the fully appended SUBOFF geometry as shown in Figure 2.8. Good correlation was found between numerical and experimental C_p along the majority of the body length with only small discrepancies at the aft end (x/L greater than 0.9). Differences in the same area but of a larger scale were found when comparing numerical and experimental C_f values along the SUBOFF geometry length. Significant refinement of the mesh density in the discrepancy areas resulted in minimal or no improvement to the C_p and C_f predictions. This suggests that the discrepancy may be due to the limitation of the Shear Stress Transport (SST)

turbulence model used in the study in capturing the swirling flows present in the stern region of the SUBOFF rudders and body.

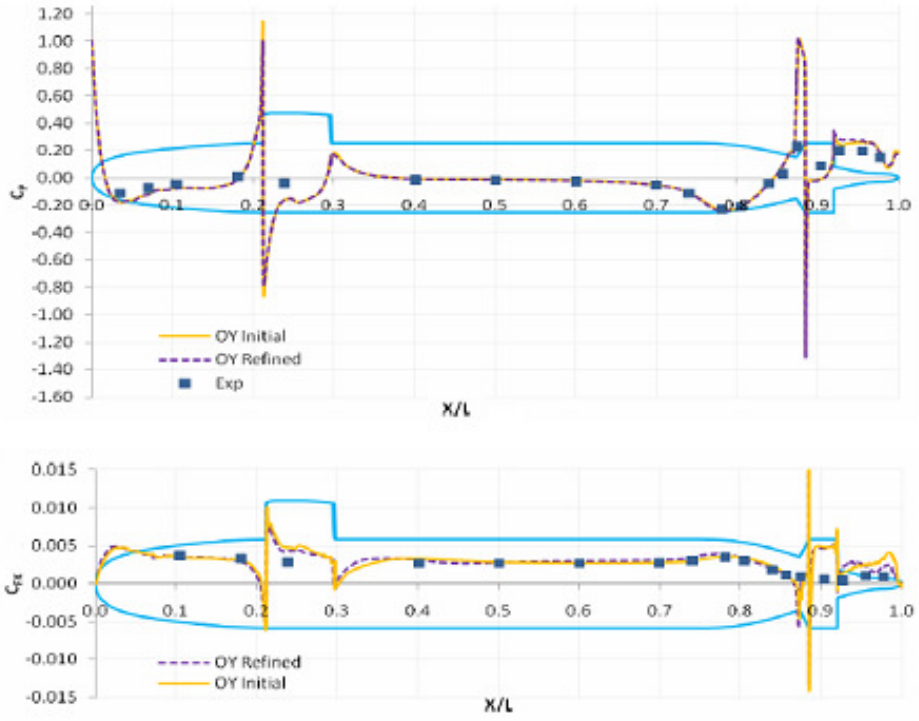

Figure 2.8: C_p (top) & C_f (bottom) along the SUBOFF hull. (Fell, 2009).

2.3 Experimental Work

Based on past studies, there are no experimental studies characterising the interaction behaviour between underwater vehicles in the public domain. While there have been aerodynamic interactions studies for air and land vehicles (Landry, 1997, Rajamani, 2006 and Weihs et al. 2006), the findings may not be applicable to underwater vehicles due to the compressibility of air. Thus, the following section focuses on the experimental work conducted on underwater vehicles in general, with the aim to obtain a basis to be used for the design of the work on the hydrodynamic interaction.

2.3.1 Experimental Work on Underwater Vehicles

Experimental research into submarine hull forms dates back to the early 1900s in which model tests were performed to determine the hydrodynamic characteristics of what was then a revolutionary type of vessel. Chase (1911) focused on measuring the resistance of four ship shape submarine bodies in the surfaced, awash and submerged conditions. This was carried out by using a strut arrangement between the towing carriage and the model as shown in Figure 2.9 in the surfaced condition.

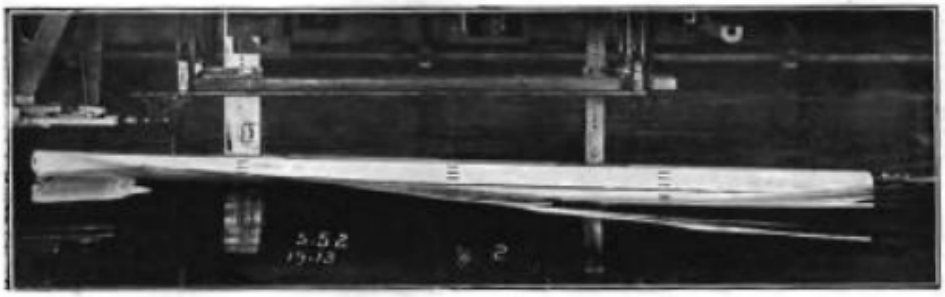

Figure 2.9: Surface condition submarine model testing apparatus. (Chase, 1911).

Vertical struts were used to hold the model at the required depth and run to determine the resistance. After each test the struts were run independently to determine their contribution to the overall measured resistance. The model resistance was found by subtracting the strut resistance from the combined strut and model resistance reading. This method is far from ideal and that this will not necessarily provide an accurate representation of the actual model resistance. A reason for this would be due to the end effects of the naked strut as it is run through the water which would increase its resistance. Therefore, the strut contribution to the resistance will be overestimated resulting in an underestimation of the actual model resistance.

A systematic series of bodies of revolution were tested by Gertler (1950). This research focused on experimental measurement of model resistance at deep submergence and the changes imposed by altering five parameters: fineness ratio, prismatic coefficient, nose radius, tail radius and position of the maximum section. A series of 24 models were constructed and tested at deep depths using a strut type apparatus similar to that used by Chase (1911) as shown in Figure 2.10.

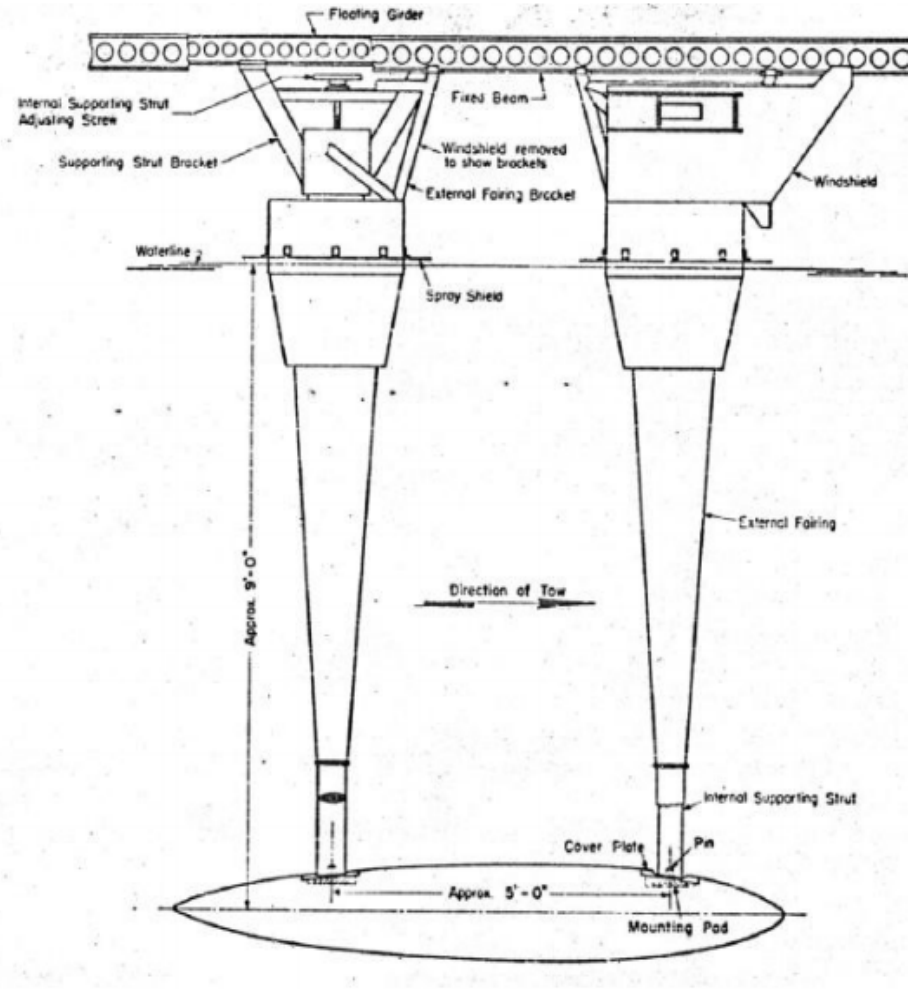

Figure 2.10: Schematic diagram of submarine model towing apparatus.
(Gertler, 1950).

A small amount of testing was carried out by Gertler to measure the additional component of wave making resistance in the near surface condition. Results are provided for four models tested in the snorkelling condition using a different apparatus configuration. In comparison to Chase (1911)'s experimental rig, Gertler's experimental rig employed a tapered strut design to improve the rigidity of the struts and a reduced strut cross section at the point of attachment to the model in order to reduce the influence of the struts on the model resistance measurements. However, the actual influence of the struts on the measure resistance was not identified.

Feldman (1987) conducted straight line and rotating arm captive model tests at the David Taylor Research Centre (DTRC). Straight line tests were performed using a

vertical and horizontal Planar Motion Mechanism (PMM). Feldman's PMM testing included the determination of control derivatives and hydrodynamic force and moment coefficients associated with variations in angle of attack, angle of drift, and over and under propulsion of a torpedo-shaped underwater vehicle model.

Feldman found that the hydrodynamic derivatives vary with Reynolds number and there appeared to be a higher Reynolds number which the hydrodynamic coefficients no longer significantly changed. Through comparisons between captive model tests and full-scale trials, Feldman deduced that if experiments were performed at higher Reynolds numbers approximately 14×10^6, the scale effects between the model and full scale vehicle were negligible.

Groves, Huang and Chang (1989) from the Defence Advance Research Project Agency DARPA published a paper that defined the geometry of the SUBOFF model. This axisymmetric model was created to facilitate open research into submarine model experimental methods on a non-classified hull form as well as validation of CFD codes by having a generic geometry available.

Two physical models, number 5470 and number 5471, were built and tested independently by the David Taylor Research Center DTRC to minimise experimental errors. Groves et al. (1989) defines the SUBOFF model in a number of different configurations. The model was tested extensively at the DTRC wind tunnel using two supports struts to minimise the effects on the flow. However, as with all experiments there is a degree of uncertainty associated with the data that needs to be accounted for when validating CFD results. Groves et al. (1989) found that the uncertainty of the velocity profiles were approximately 2.2% due to the use of hot film velocity measurements and an uncertainty of 0.15% associated with the pressure coefficients.

Roddy (1990) investigated the stability and control characteristics of the DARPA SUBOFF model with testing carried out on a series of different appendage configurations. This was undertaken by straight line deep submergence captive model testing in the vertical and horizontal planes using the DARPA SUBOFF model with a length of 4.356m. The model was mounted via two vertical struts spaced 1.83m apart as shown in Figure 2.11. The purpose of this investigation was to determine the

control derivatives and hydrodynamic force, and moment coefficients to be used in the submarine equations of motion to determine dynamic stability.

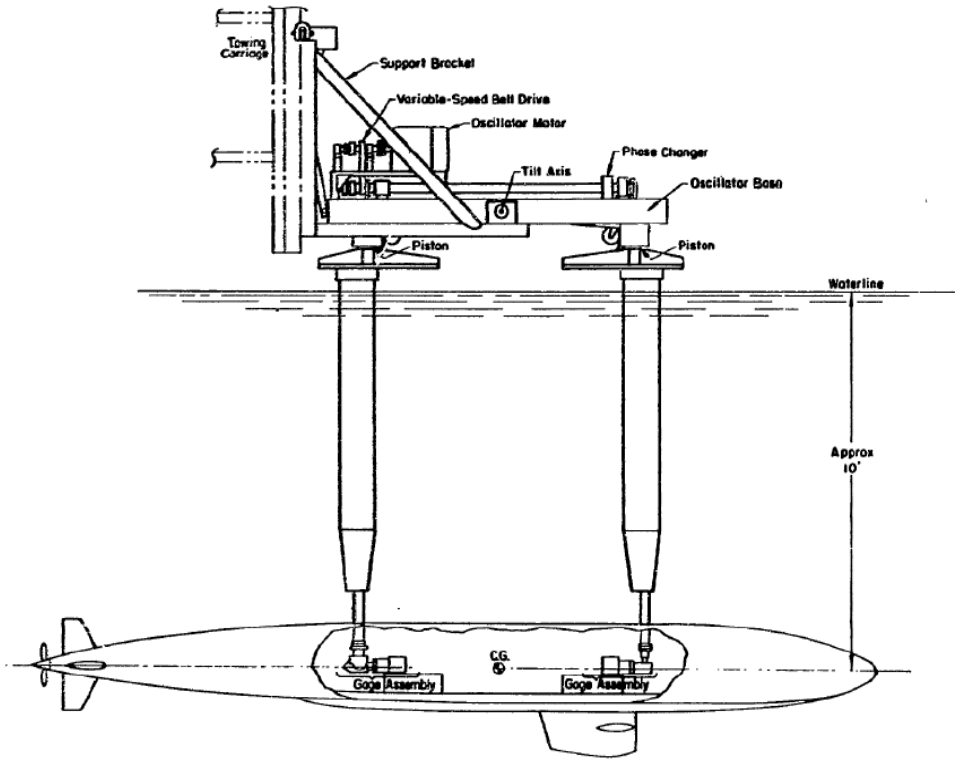

Figure 2.11: DARPA SUBOFF model testing apparatus. (Roddy, 1990).

Roddy noted that many sources of bias and precision errors were introduced into experiments of this nature. Changes in load cell calibration over time were predicted to result in bias errors of around 0.5%. This issue was addressed by checking the transducer calibration 30 times over the three days testing period.

When conducting experimental testing of models in wind tunnels and towing tanks, the methods of mounting the model to the test rig require important consideration as the mounting post(s) can have a significant effect on the results. De Moss (2007) identified the most common mounting arrangement for underwater vehicles, which is stern sting connection is attached to a force balance. However, De Moss further states that with this mounting arrangement several problems may arise directly affecting the accuracy of the experimental results including: flow distortion and interface drag

caused by the sting and geometrical inaccuracies due to the model modifications required to accommodate the stern connection.

Dress (1990) conducted model tests on a submerged sphere using a sting mounting arrangement and a magnetic suspension balance system in an attempt to quantify the uncertainties between model mounting arrangements. Dress compared the drag coefficients of each system as shown in Figure 2.12 and found a decrease in total drag when using the sting mounting arrangement. It was concluded that an apparent increase in the slenderness ratio occurs as the sting effectively acts as an extension of the body. This effect, combined with interruption of the separated wake at the stern of the body reduces the total measured drag.

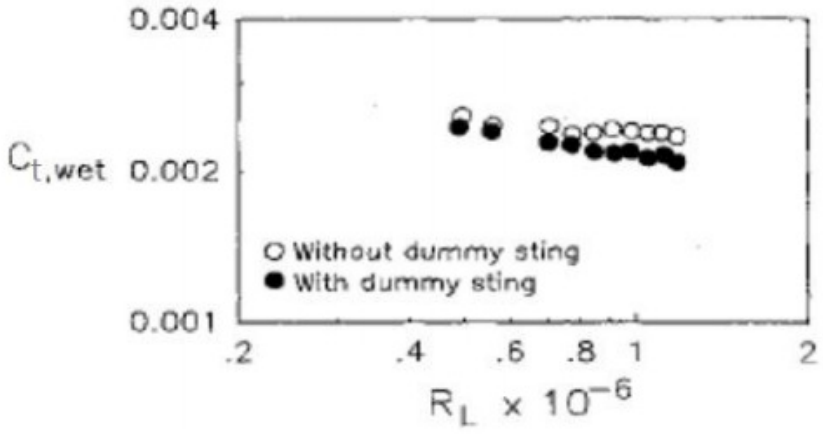

Figure 2.12: Drag coefficients measured using sting and suspension balance systems. (Dress, 1990).

Experimental testing was carried out by mounting the SUBOFF model on a curve sting attached to the HPMM. The strongback cylinder was located inside the SUBOFF model. The model was attached to the strongback by forward mounted AMTI 100lb. load cell. A mounting arrangement incorporating a slider secured the model in the aft position. This allowed freedom of movement and prevented pre-stressing the model in the axial direction.

Van Steel (2010) and Neulist (2011) used captive model towing tank testing and CFD to identify and quantify the effects of depth, speed and appendages on the generation of surface waves for a submarine travelling near the free surface.

The experimental work focused on straight line, zero incidences towing tank testing to determine submarine hull resistance as a function of speed and depth from the free surface. This work was used to validate the ANSYS CFD numerical analysis, which also involved investigation of the effects created by the sting mounting arrangement.

Model testing by Van Steel (2010) built on the work made by Wilson-Haffenden (2009) by the addition of a sail appendage to the model along with inclusion of turbulent flow tripping using Hama strips along the sail leading edge.

Two load cells were used in the testing apparatus. A 6-DOF load cell was mounted in the forward position and a 1-DOF load cell on a slider, configured to measure vertical axis forces and free to move in the longitudinal axis was positioned aft as shown in Figure 2.13. The addition of an aft load cell to the testing configuration was implemented by Van Steel which was not previously used by Wilson-Haffenden. Validation testing was carried out with a maximum difference of 3.54% to the testing results from Wilson-Haffenden.

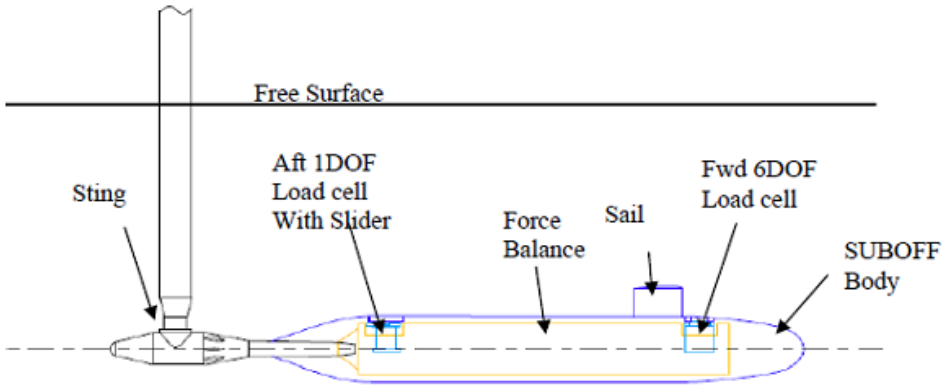

Figure 2.13: SUBOFF testing apparatus. (Van Steel, 2010).

Model testing by Neulist (2011) was built on the work made by Van Steel (2010) by changing the slider with flexure mounted at the aft load cell position. This was conducted to compare the results obtained. The aft load cell was changed from the XTRAN 1-DOF with the slide to the AMTI 6-DOF for the flexure.

A comparison between results for axial resistance with the slide and with the flexure is shown in Figures 2.14, 2.15 and 2.16 at an H* of 3.30, 2.20 and 1.10 respectively. This demonstrates excellent repeatability of results between the flexure mounting and slide mounting for the aft load cell. The small degree of difference between results is rarely greater than 6% above a Froude number of 0.10. This is an acceptable margin of experimental error calculated by ITTC 7.5-02 01-02 (1999) and ITTC 7.5-02 02-04 (2002b). These results prove that the use of the flexure mounting for the aft load cell provides directly comparable results to the slide mechanism. This gives confidence in using the flexure with a 6-DOF load cell to provide accurate results in any future testing that is carried out. The use of flexure is the preferred option for future testing due to the added capability it provides in measuring forces in all three axes.

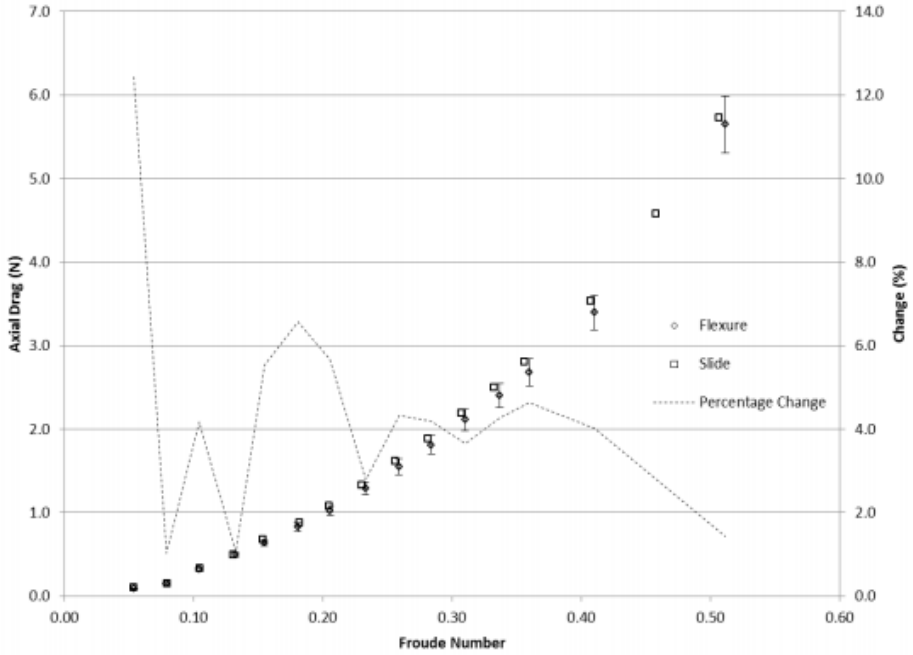

Figure 2.14: Flexure and slide axial resistance comparison at an H* of 3.30. (Neulist, 2011).

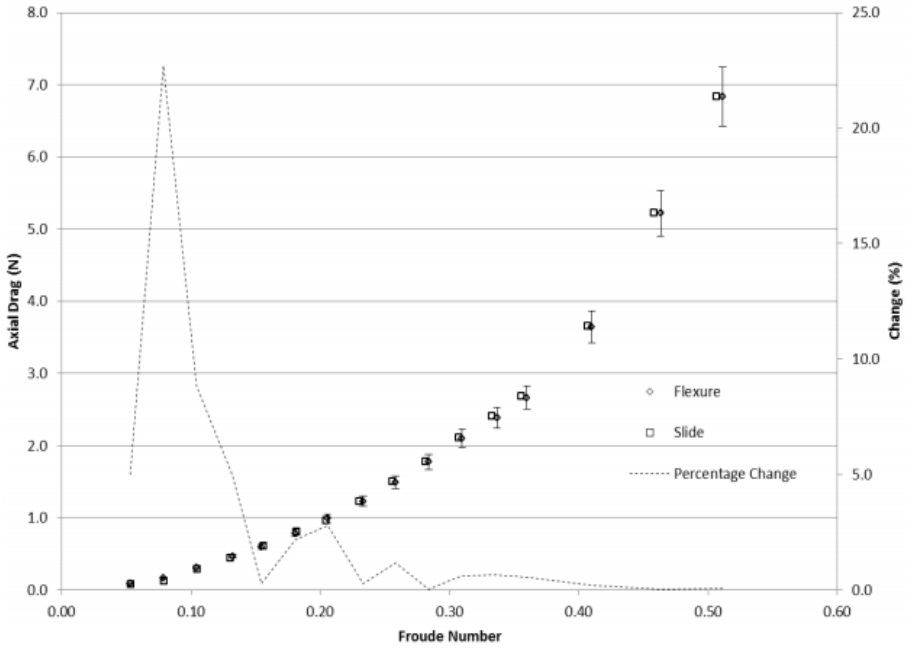

Figure 2.15: Flexure and slide axial resistance comparison at an H* of 2.20. (Neulist, 2011).

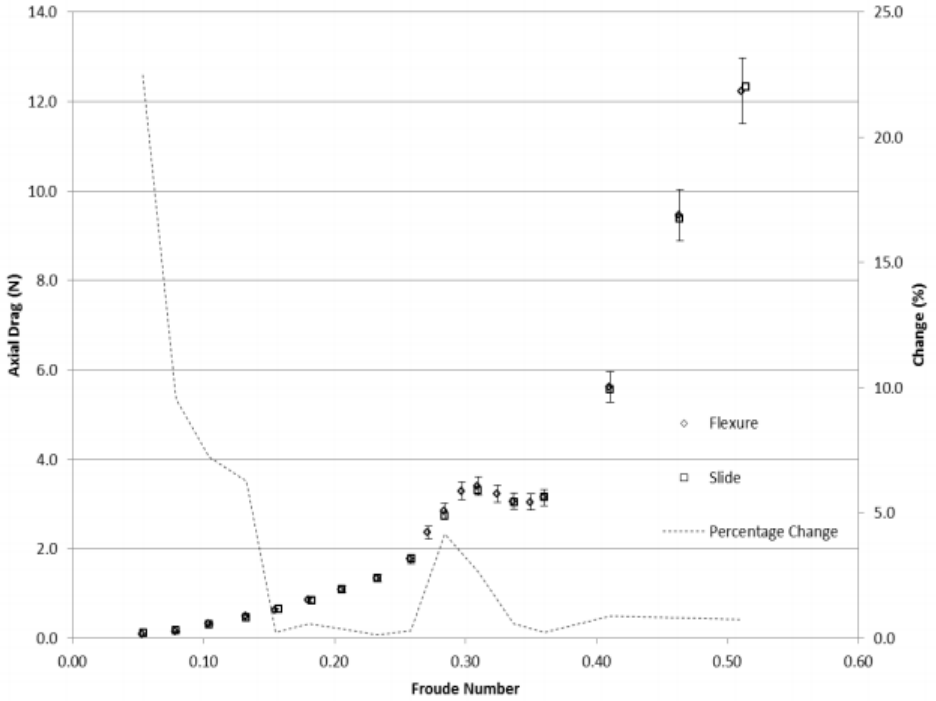

Figure 2.16: Flexure and slide axial resistance comparison at an H* of 1.10. (Neulist, 2011).

Van Steel (2010) experimental work focused on straight line, zero incidences towing tank testing to determine submarine hull resistance as a function of speed and depth from the free surface. This work was used to validate the ANSYS CFD numerical analysis, which also involved investigation of the effects created by the sting mounting arrangement. Experiments indicated that the effects of wave making resistance at depths greater than non-dimensional depth (H*) of 3.30 were negligible. Van Steel concluded that the wave making by the submarine model and the superposition of wave peaks and troughs have a noticeable effect on heave and pitch on the submarine when operating close to the free surface.

2.3.2 Turbulence Stimulation

The inability to scale the viscosity of water for model tests can result in experiments being conducted under laminar conditions when the equivalent full scale flow is turbulent. Due to the differences in C_f values between laminar and turbulent flow regimes, the inability to successfully produce turbulent flow in model testing will provide results that do not adequately represent full scale.

The primary purpose of a turbulence stimulation device is to effectively and efficiently transits the boundary layer flow from laminar to a sustained fully turbulent state at a specific location and in a coherent manner. Hama (1956) describes an efficient tripping device to be one that provides a consistent and fixed stimulation with the least parasitic drag caused by the device. The laminar to turbulent transition phenomenon of the boundary layer surrounding a body in relative motion continues to be thoroughly investigated. Schlichting et al. (1999) indicates that the transition of the boundary layer surrounding a solid body is highly dependent on the Reynolds number, pressure distribution, surface roughness condition, and the turbulence intensity of the encountered flow.

Todd (1948) states that the turbulence stimulation devices most commonly used in model tests are:

- sand strips at or in the region of the bow;
- a strut ahead of the bow;
- pins or other forms of specified individual projections fitted near the bow; and
- a trip wire at 5% of the length between perpendiculars from the bow.

After comparing two and three dimensional tripping devices, Hama (1956) concludes that a three-dimensional device such as a row of pins or spheres is the more superior in fixing a transition point which is constant stimulation. This is because a three-dimensional device is more direct in producing a three-dimensional vortex loop, which is confirmed to be directly responsible for transition as soon as the vortex shedding occurs.

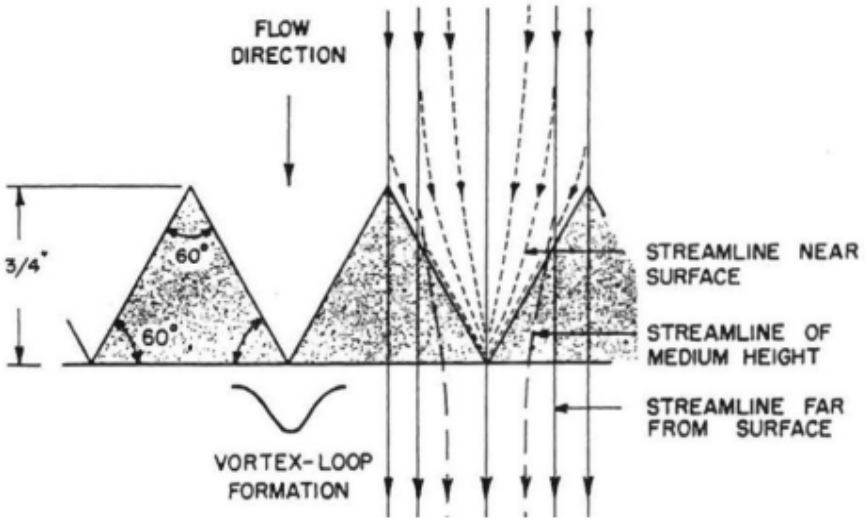

Figure 2.17: Hama strip geometry and flow streamlines.

Figure 2.17 shows the plan view of a series of triangular patches used for turbulence stimulation, commonly referred to as a Hama strip. This arrangement directly produces three dimensional vortex loops with more efficiency in shedding and therefore appears to provide a simple yet better way of tripping laminar boundary layers than any other known stimulation device (Hama, 1956).

The trend of the resistance coefficient curve is a good indication of whether a turbulence stimulation device is effective or not. Generally, the resistance curve of a

turbulent flow is at its greatest at low speeds and gradually decreases with increasing speed without any spikes or fluctuations. The Schoenherr line is a representation of the average value of skin friction coefficients from available flat plate skin friction data for fully turbulent flow. The Schoenherr line is shown in Figure 2.18 as an average of various flat plate skin friction coefficients and is defined as,

$$\frac{0.242}{\sqrt{C_f}} = log_{10} RC_f \qquad 2.1$$

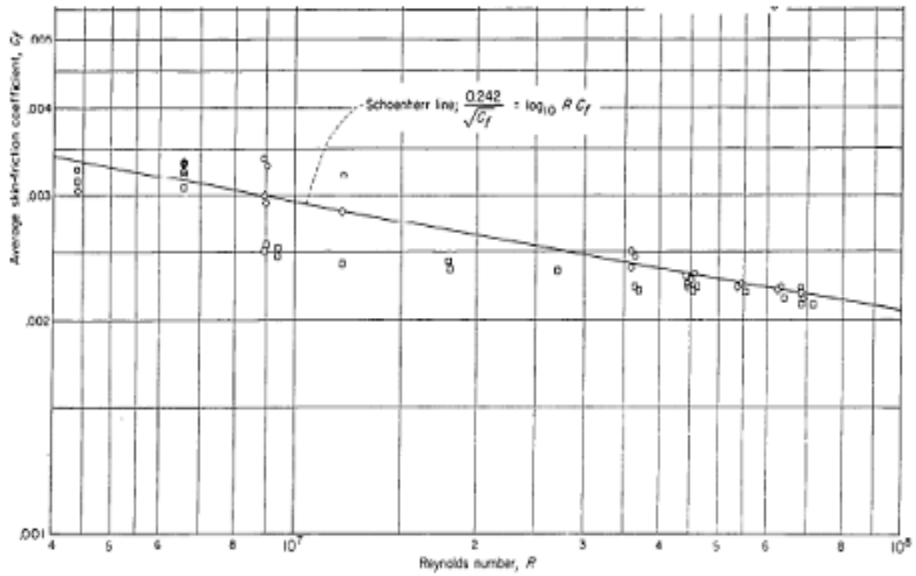

Figure 2.18: Schoenherr line as a representation of flat plate skin fricion data.

The trend of the Schoenherr line is often used to compare experimental data to determine whether a flow is laminar or turbulent as it is a known turbulent resistant coefficient curve. Figure 2.19 shows a comparison of C_f for three-dimensional bodies with and without turbulence stimulation found by Hoerner (1958). It is noted that the bodies with turbulence stimulation was efficient and therefore its follows the trend of the Schoenherr line.

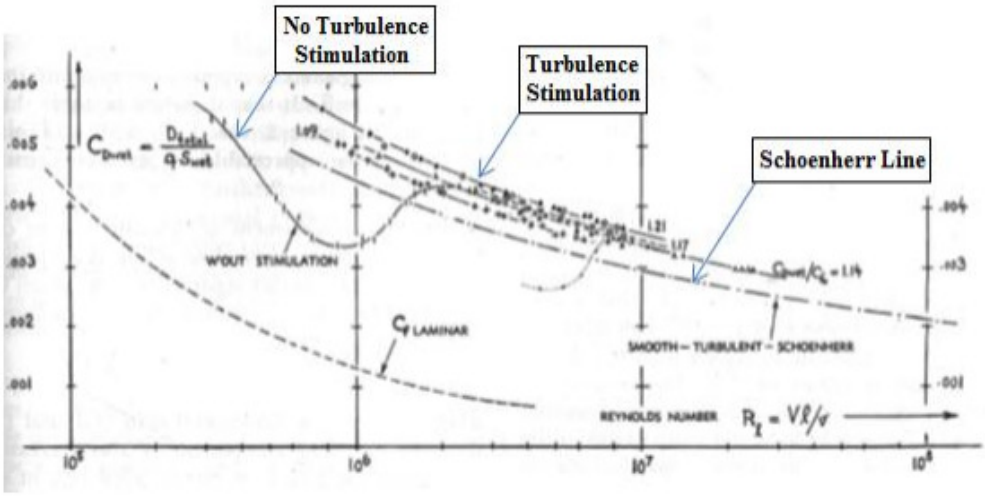

Figure 2.19: Frictional resistance coefficient for bodies with and without turbulence stimulation. (Hoerner, 1958).

Neulist (2010) found a series of Hama strips located at 5% of LOA from the bow with varying nominal thickness between 0.30mm and 1.50mm. The strips were tested on the SUBOFF model to select an efficient turbulent flow stimulation device. The Hama strips were compared to a condition with studs fitted at 10% of LOA and a bare hull condition with no turbulence stimulation. The #4 Hama strip with a nominal thickness of 0.60mm was found to be the most efficient turbulence stimulation device. This strip produced turbulent flow in the low speed region determined by comparison of C_d values, without the excessive levels of parasitic drag caused by thicker strips. The #4 Hama strip produced C_d values similar to the studs located at 10% of LOA.

Relaminarisation of the boundary layer along the hull form was not detected through flow visualisation techniques carried out. However, an investigation using high quality flow visualisation methods will provide further analysis of the production and maintenance of a turbulent boundary layer around the SUBOFF model.

2.4 Hydrodynamic Interaction between Surface Ships

Due to the limited studies on the hydrodynamic interaction between underwater vehicles in the public domain, the literature review is extended to surface ships in order to draw similar parallels on the behaviour of the hydrodynamic interaction.

The interaction problem in navigation is usually produced when the ships are moving in restricted waterways, such as harbours or canals (King, 1977). The encounter of two vessels can fall into one of two main categories. The first case is when a ship passes on reciprocal courses or overtakes another at a close distance, which commonly happens when sailing in narrow channels. The second case is when a ship manoeuvres close to another during an operation such as when a tug provides assistance to a ship (lightering, etc). In the interaction problem the flow around the ship hulls is modified, generating additional forces and moments in the horizontal plane on the ships (surge and side forces, and yaw moment).

The interaction phenomenon is also influenced and caused by the two navigation boundaries, which are the bottom and the lateral boundaries of the navigation area. The former, is usually given by introducing depth dependent hydrodynamic coefficients. The latter is limited by bank or quay walls, causing a bank effect to a ship navigating in parallel course thus, producing the hydrodynamic interaction forces on a ship in a channel towards or away from the nearby obstacles (Ch´ng, 1991 and 1993). Some examples are shown in Figure 2.20.

Figure 2.20: Interaction between ships and their boundary: a) A vessel is assisted by a tug near the harbour; b) Two ships sailing in a river in head encounter; c) Manoeuvring when overtaking between two ships in calm water; d) Ship sailing in a narrow canal.

The phenomenon produced in the interaction problem can cause serious accidents, when it is not considered. Chatterton (1994) comments on the famous accident of the passenger liner Queen Elizabeth II, where the vessel was sailing at high speed in shallow waters. The suction force created between the bottom and the ship caused the Queen Elizabeth II to run aground off the Cutty Hunk Island.

Fonfach (2010) performed a numerical study to simulate the hydrodynamic interaction between a tug and a tanker ship in shallow waters. The study examined the effects of lateral separation, longitudinal separation, and speeds of a tug while operating close to a tanker. When the differences in the ship dimensions are large, the effect produced during the interaction between ships increases and the risk of accident is higher for the smaller ship. A typical situation which involves differences in ship dimensions is the ship-tug assistance. When a tug assists a ship, the position of the tug with the assisted ship and the lateral distance, can be constantly changing. The

consecutive positions of a tug when it is approaching to assist a ship are shown in Figure 2.21.

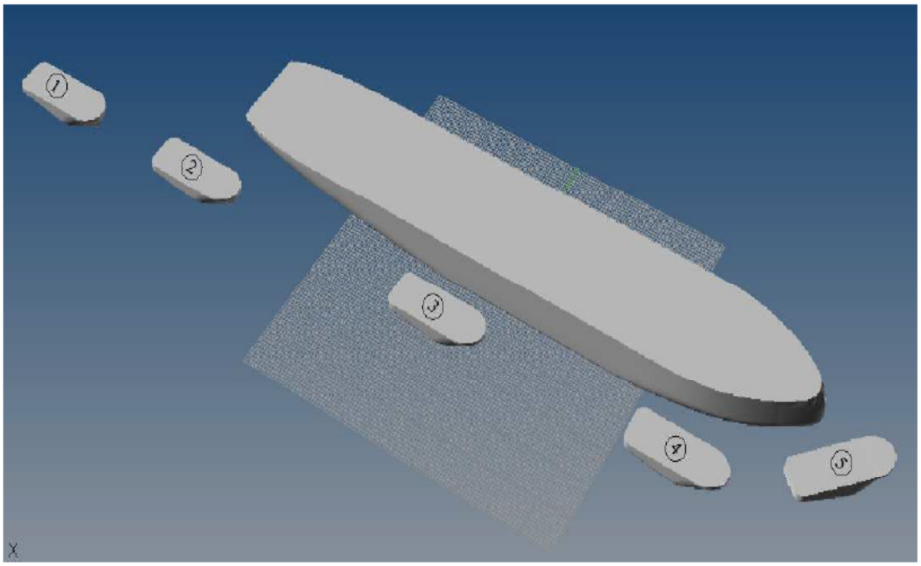

Figure 2.21: The position on a tug operating close to a tanker ship. (Fonfach, 2010).

When the tug is near the stern of the ship (position 1), an increase in its velocity may occur due to the flow velocity from the aft of the ship. In close proximity to the ship hull, a low pressure moves the tug to the ship's direction. For ships in ballast condition, or ships having particular overhanging stern, the tug can easily go to position 2, generating damages to its hull or superstructure.

Going forward and near the hull (position 3), the tug is under the action of an important suction force in the direction of the ship hull, and negative yaw moment (based on right-handed Cartesian frame of reference) is due to the accumulated water in the tug bow. When the tug is attracted by the ship, it is in general difficult to recover its course. When the tug is in position 4 (side of the bow) it enters an area of high pressure, the negative yaw moment is growing, and must be compensated by the appropriate use of the rudder and propeller to avoid the risk of accident.

In position 5 when the tug is near the bow, a strong negative side force on the stern brings the tug to the front and under the bow with the risk of capsizing. Then, proper operational condition must be applied. The study of the interference when a tug is

operating near another ship is important to define the prediction of the manoeuvring characteristics of the tug and is useful to optimize the waterway operation. Therefore, developing a model which is able to predict the interaction forces with accuracy while considering restricted waters and course keeping of ships, is necessary.

Greets (2011) conducted an experiment using an azimuth stern drive tug towed together with the model of a container carrier. Forces and moments on the tug model were measured for a range of relative positions and drift angle at multiple forward speeds. He found that an interaction of side force was clearly present and changing when the tug sailing along the hull of the container vessel. The highest side forces appeared when the tug's centre of the gravity was at a longitudinal position of about 1.5 length of the container vessel measured from the stern of the vessel. Both interaction side force and yawing moment decreased with increasing lateral distance between container vessel and tug. Therefore, a changing interaction surge force, side force, and yaw moment, were experienced along the length of the container vessel. To keep station, the tug was generally required to sail with constant drift angle applying a constant azimuth angle to counterbalance the yaw moment and side force. This phenomenon will diminish when moving further forward and to the side away from the assisted vessels.

Kriebel (2005) carried out an experimental measurement of the interaction forces and moments on a moored ship due to a passing ship moving parallel to the moored ship. Variations in the model tests were included, considering changes in the passing vessel speed, vessel displacement, water depth, and separation between the two ships. The experimental data were analysed in two ways. First, the empirical equations were developed, describing variation in the peak mooring loads with changes in the parameters. Second, two existing models were evaluated in experimental tests to determine their ability to predict the measured mooring loads.

Duffy (2011) conducted an experimental model test for the berthed ship. It's measured the surge force, side force and yaw moment at three different channel geometries (refer to Figure 2.22). The influences of waterway geometry on magnitude of the peaks and the form of the time domain interaction forces and moment have been quantified. Therefore, the interaction forces and moment on the berthed ship

were similar for the test cases with varying degrees of lateral channel restriction. The magnitude of the peak interaction surge force was the largest for the narrow channel configuration, and then the side force was experienced with the widest channel configuration. Furthermore, the maximum berthed ship motions and maximum mooring line loads predicted using the idealised forces and moment were generally similar to those predicted with the measured forces and moment.

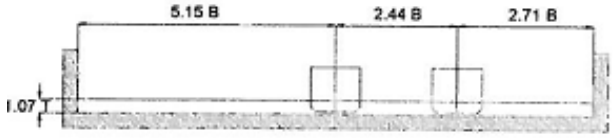

Channel cross section for Case A

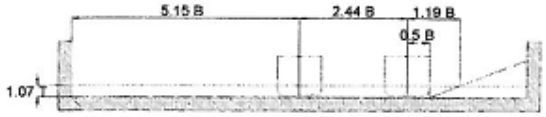

Channel cross section for Case B

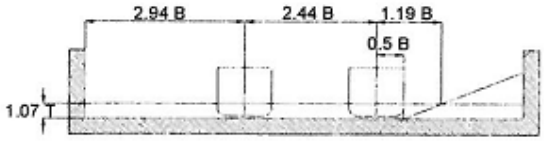

Channel cross section for Case C

Figure 2.22: Three geometries channel cross section. (Duffy, 2011).

In order to improve the accuracy of the prediction of interaction forces and moments between ships, a semi-empirical method was developed by Brix (1993), estimating the time histories of the forces and moments in the horizontal plane due to interaction with another ship as a function of geometry speed and environmental parameters, based on his previous work (Brix, 1979). The method to estimate the forces and moments action on a ship during an overtaking manoeuvre was presented in the Manoeuvring Technical Manual. Here approximations were formulated for the maximum values of the longitudinal and transverse forces and for the yawing moment. The method was subjected to some restrictions: it was only valid for overtaking manoeuvres. Thus, the influence of water depth was not taken into account, and also the ratio of ships' lengths is limited. Brix states: "Besides some

theoretical approaches and experimental results, no reliable results are available except of a semi empirical nature."

Vantorre et al. (2002) reported results from a large series of ship-ship interaction model experiments using an empirical method to calculate the extreme peaks in typical time traces of interaction forces. The investigation was carried out for four ship models in shallow water towing tank, covering a large variety of parameters such as overtaking/overtaken, speeds, distances, and water depths. They suggested that it is impossible to develop a full empirical method taking into account all the possible parameters that influence the interaction forces between two ships passing each other.

Based on the studies on the hydrodynamic interactions between surface ships, it is deduced that the interaction effects between underwater vehicles will depend on the: relative size between the submerged vehicles, lateral separation distance, longitudinal relative positions, vehicle speeds, hull shapes, submerged depths, and water depth.

Chapter 3

Experimental Fluid Dynamics (EFD)

3.1 Introduction

When an Autonomous Underwater Vehicle (AUV) is moving in close proximity to a submarine, interaction between the hydrodynamic pressure fields surrounding each underwater body can impose rapid changes in the forces acting on the AUV. This can potentially affect the ability of the latter to maintain its trajectory, which may result in mission failure including collision between the vehicles. Model scale experiments were conducted in the AMC towing tank facility to investigate the interaction forces and moments on an AUV (represented by SUBOFF) in close proximity to a larger body. The tests were conducted for different longitudinal and lateral offsets between the submarine and the AUV. The aim of the experimental testing was to quantify the interaction drag force, side force and yaw moment on the AUV when moving in close proximity to a larger body and to validate CFD predictions. The experimental results, in conjunction with the CFD predictions, will be used to identify the operation region when the interaction forces and moments are minimal.

3.2 AMC Towing Tank

The physical model scale experiments were conducted at the AMC Towing Tank (refer to Figure 3.1). The tank is 100m long, 3.55m wide and has a maximum water depth of approximately 1.5m. For these tests, the water depth was set to 1.5m.

A towing carriage is mounted on rails above the tank and is free to travel the entire length of the tank. The velocity of the carriage can be varied up to a maximum of 4.6m/s. The carriage houses on-board data acquisition (DAQ) and signal conditioning systems.

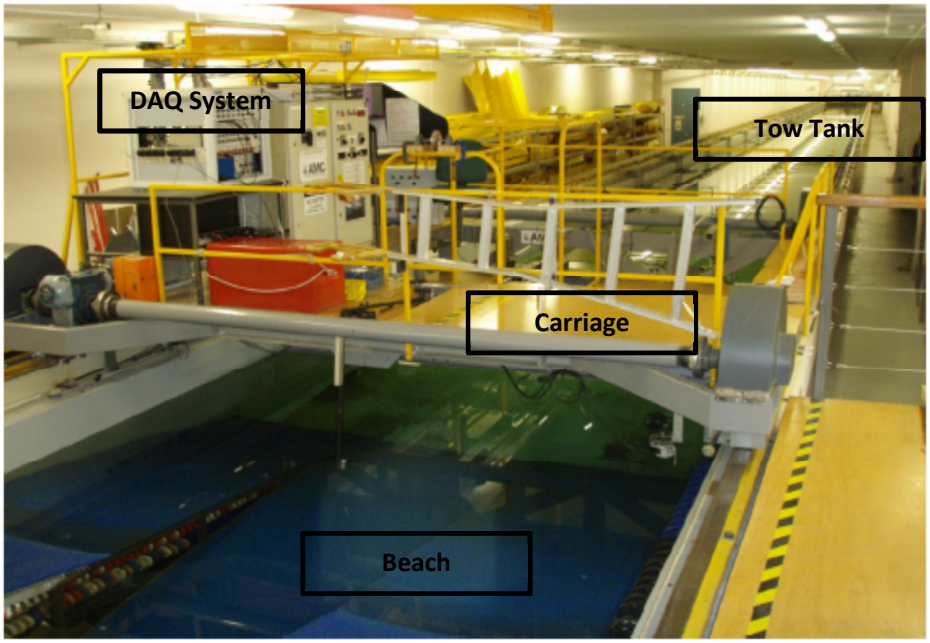

Figure 3.1: AMC's Towing Tank.

3.3 Model Details

Two models were used to perform the tests; the small body representing the AUV (SUBOFF) and the larger body representing the submarine (Larger Submarine Body). The smaller AUV was represented by the SUBOFF geometry that was specially developed for the AMC Towing Tank to be used in conjunction with the Horizontal Planar Motion Mechanism (HPMM), with the force balance located within the body. To minimise blockage effects due to the Towing Tank boundaries, the larger body was restricted to 2.23 times the diameter of the SUBOFF hull form. The diameter ratio of 2.23 between the vehicles is relatively low for a study focusing on the flow and pressure regime around the larger body and its effects on the smaller AUV. Although the smaller diameter ratio reduces the dominance of the larger body on the flow and pressure regime and the resulting behaviour of the smaller AUV, the results enable the CFD model to be validated while providing an insight into the trends as the speeds and longitudinal/lateral separations are varied. The description of each model is discussed below.

3.3.1 AUV Model (SUBOFF) (AMC-09-28)

SUBOFF was used as the AUV model for this project. SUBOFF is an axisymmetric submarine model created by the Submarine Technology Program Office of DARPA in 1989 to assist in the research and development of submarines. The geometry of the SUBOFF model was defined and published by Groves et al. (1989), who mathematically defined the dimensional proportions of the SUBOFF hull form and a range of appendages that can be fitted to the model.

The SUBOFF model is a non-classified generic hull form to facilitate a coordinated approach to verification of CFD codes against model experimentation. This was achieved through the creation of an accurately defined and publically available submarine body to be used purely for research purposes, in order to enable the sharing of information in CFD and experimental programs.

The SUBOFF model is shown with the sail appendage and a Hama strip as tested in the current project in Figure 3.2. The SUBOFF model defined by DARPA includes a wide range of other appendages including stern control surfaces. For the tests in the current project, only the sail appendage was attached to the model.

The AMC SUBOFF model was built at a scale ratio of 1:2.81 compared to the DARPA SUBOFF model giving an overall length of 1.56m and diameter of 0.18m. In order to mount the model to the test rig through the stern section the aft most 0.12m of the model was removed giving an overall length of 1.44m. The principal dimensions of the model are shown in Figures 3.3 and 3.4.

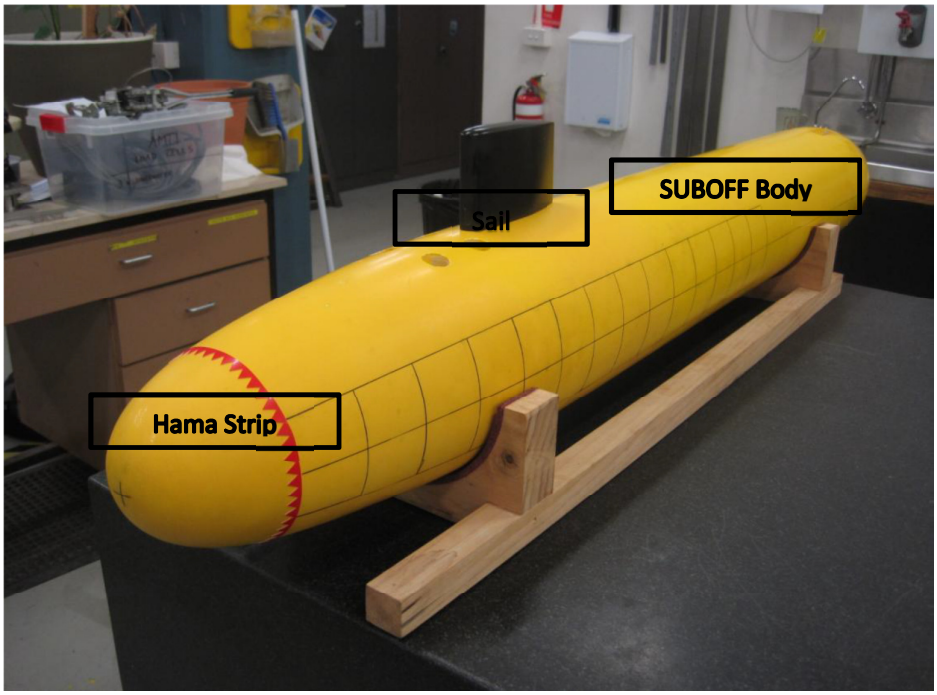

Figure 3.2: AMC SUBOFF model with sail and Hama strip.

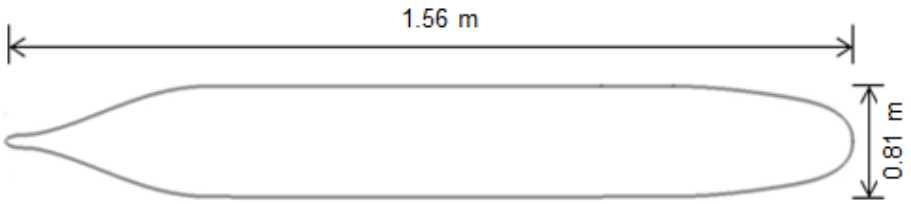

Figure 3.3: AMC SUBOFF original model principal dimensions.

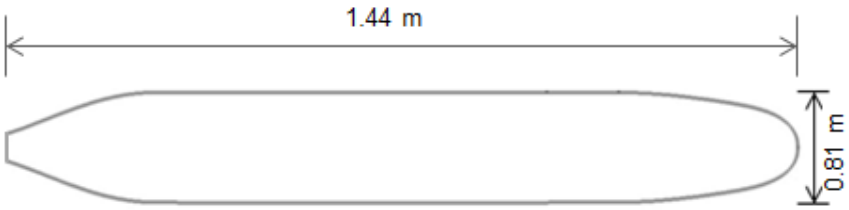

Figure 3.4: AMC SUBOFF with aft most 0.12m removed model dimensions.

3.3.2 Larger Submarine Body (AMC-11-21)

Due to the dimensions of the Towing Tank, the size of the larger body was restricted to a diameter of 2.23 times the SUBOFF diameter. The larger body had a diameter of 0.41m and length of 2.85m and was divided into five sections to aid in the construction process; dome, body, fairing, end cap and strut, as shown in Figure 3.5.

The larger submarine body was fully developed at AMC and was constructed to meet specific requirements of the Towing Tank facility. The body was constructed from PVC pipe and reinforced with a wooden frame and fiberglass, as shown in Figure 3.6. The dome and fairing sections were constructed using reinforced fibreglass. The end cap was constructed using laminated wood to achieve smoother curvature to minimise disruptions to the flow. The dome, end cap and fairing are shown in Figure 3.7. The struts were made from extruded aluminium with an elliptical section to minimise the disturbance to the flow. The struts are shown in Figure 3.8

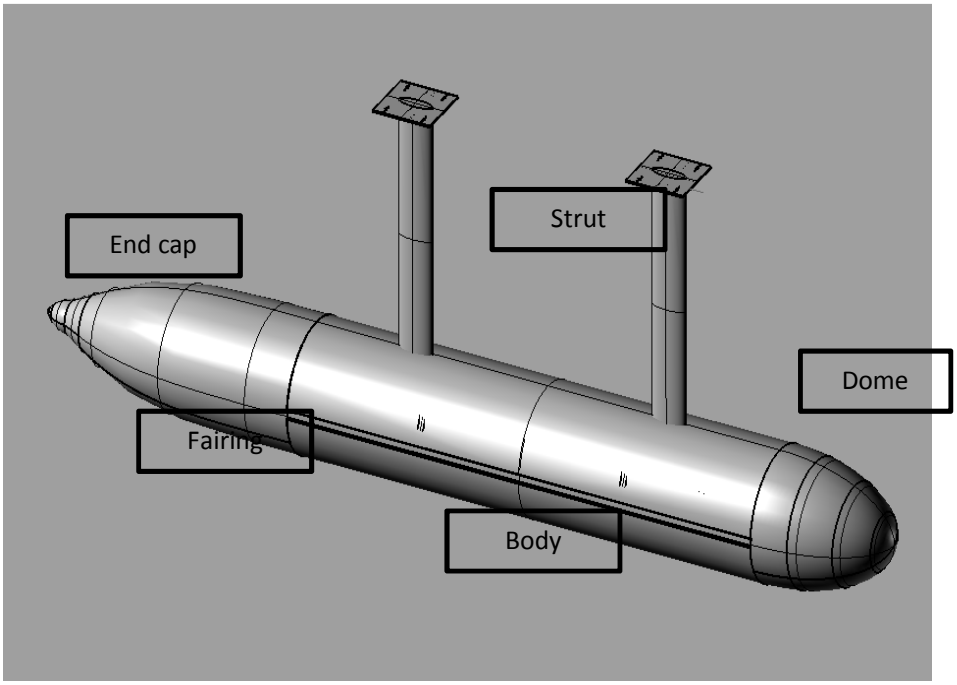

Figure 3.5: Larger submarine body model layout.

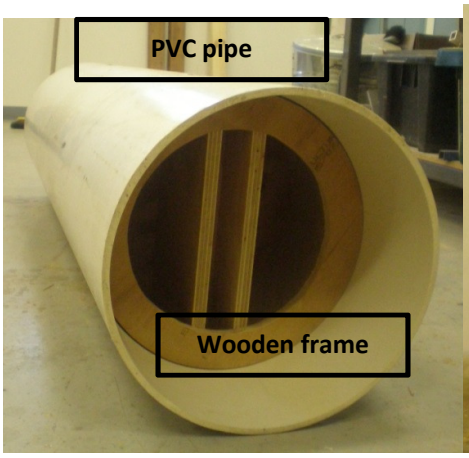

Figure 3.6: Body with wooden frame support.

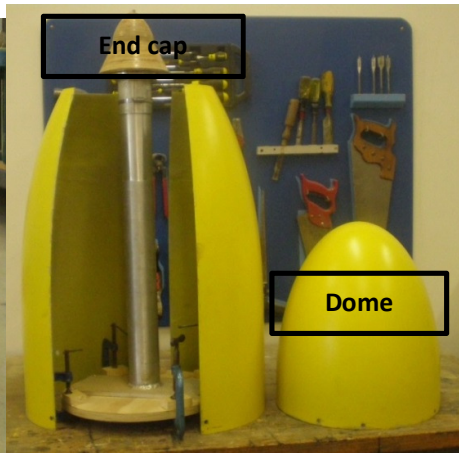

Figure 3.7: Dome, end cap and fairing.

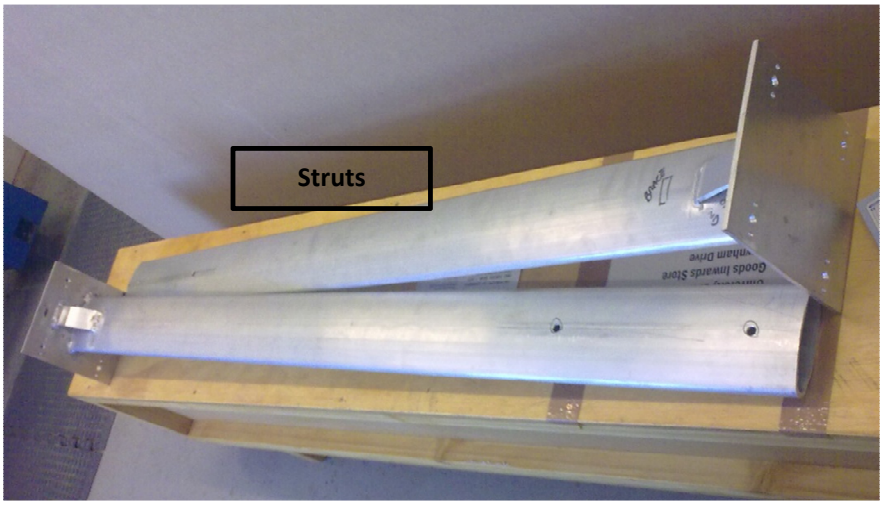

Figure 3.8: Struts.

3.4 Test Rig

3.4.1 AUV Model Test Rig

The AUV model (SUBOFF) was attached to the Towing Tank carriage via the Horizontal Planar Motion Mechanism (HPMM). The HPMM was designed by Defence Science and Technology Organisation (DSTO) and developed with AMC to provide pure yaw and pure side motion to captive models allowing the analysis of

vessel hydrodynamic manoeuvring characteristics (Anderson et al. 1995). For this investigation however, the HPMM was used in the static condition, where the model was rigidly attached to the HPMM, aligned parallel to the Towing Tank centreline and used to acquire different lateral positions of the AUV (SUBOFF) relative to the larger submarine body. The HPMM, attached to the AMC towing tank carriage, is shown in Figure 3.9 and the SUBOFF model attached to the HPMM is shown in Figure 3.10. The HPMM was used as it enables the lateral separation between the small body and the larger body to be changed easily.

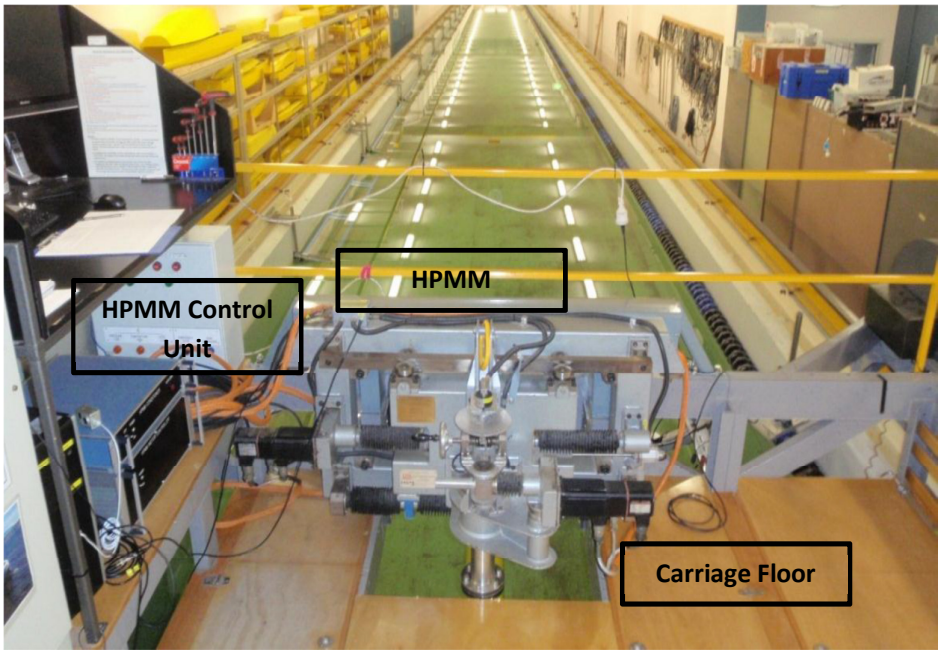

Figure 3.9: HPMM fitted to the AMC Towing Tank carriage.

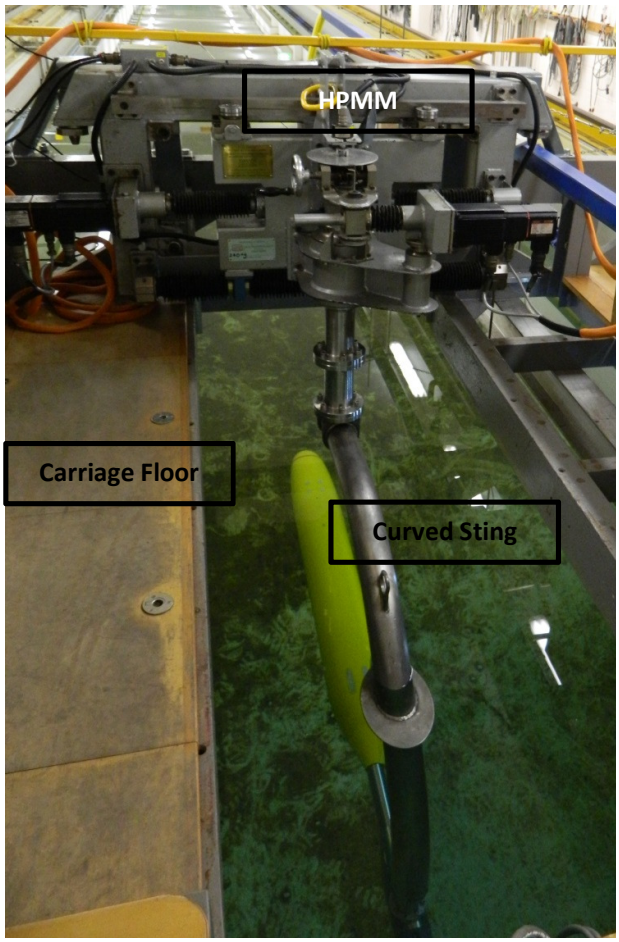

Figure 3.10: SUBOFF attached to the HPMM via the curved sting.

A schematic of the AUV test rig is shown in Figure 3.11. The model is attached to a sting which enters the model through the aft section of the hull. The sting is attached to a curved sting which is attached to the base of the HPMM. The model was flooded for the tests, with a gap between the horizontal sting and the aft section of the model to enable measurement of the forces on the model. The hydrodynamic forces on the AUV model were measured using two waterproof load cells mounted in-line within the force balance located inside the SUBOFF geometry. The aft and forward 6 degree of freedom (DOF) load cells were used to measure the drag and side forces. For the validation of the CFD model, the experiments were conducted under steady-state conditions, where the vehicles were moved together at constant forward speed, with the force balance within the SUBOFF model recording the drag and side forces on the AUV due to the interaction of the two vehicles. The yaw moment was calculated from the forward and aft side forces.

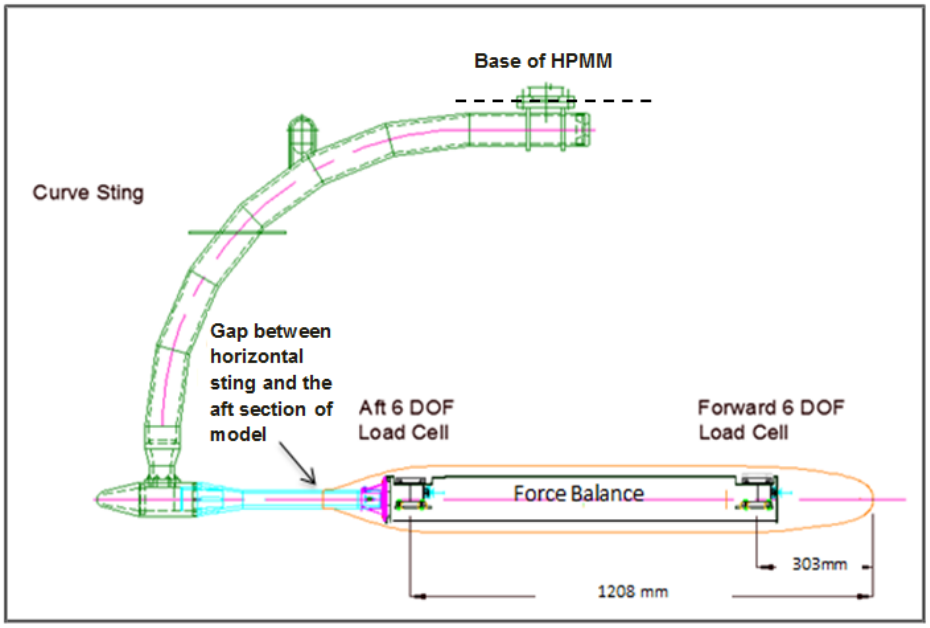

Figure 3.11: The AUV (SUBOFF) fitted to the force balance.

3.4.2 Larger Submarine Body Test Rig

The rig to hold the larger submarine body was developed using an aluminium I-beam attached to the Towing Tank carriage and supported by a rectangular hollow section steel beam (refer to Figure 3.12). The mechanism for holding the model was specifically designed to obtain the desired range of longitudinal separations between the models and to withstand the loads applied by the model.

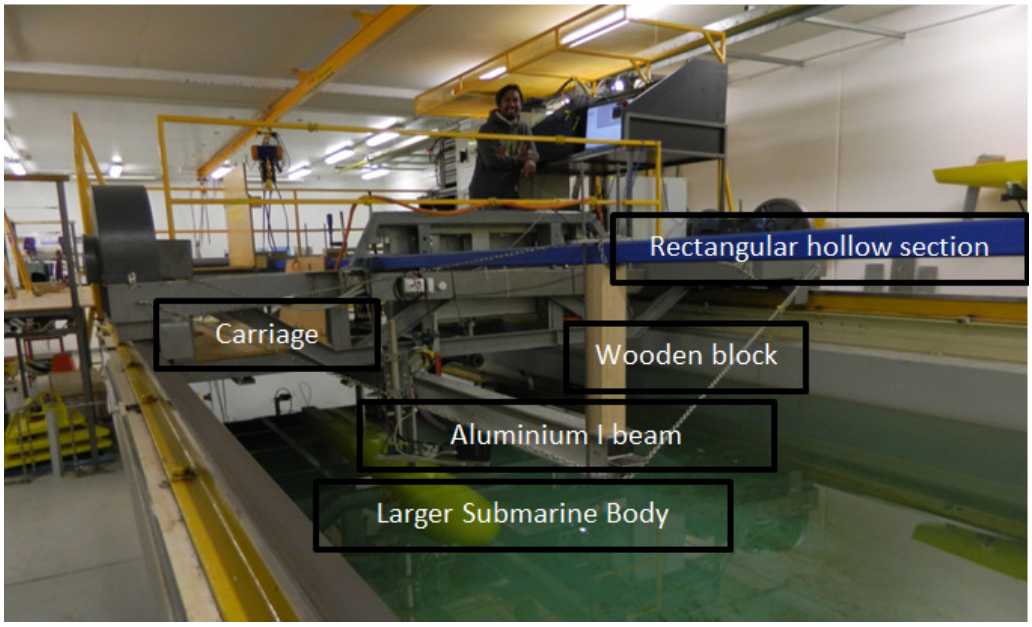

Figure 3.12: Test rig designed with the larger submarine body attached.

3.5 Test Program

The model scale tests were conducted with various forward speeds, lateral separations and longitudinal separations. The drag and side forces were measured using the test rig shown in Figure 3.12. The conditions tested are given in Table 3.1. Both models were moving parallel to each other at the same forward speed.

Figure 3.13 shows the plan view arrangement of the model configurations used for the CFD and EFD work. The lateral separations are based on the distance between the nose tips of the two bodies. The longitudinal separations are measured from the nose tip of the larger body to the smaller vehicle, with 'positive' identifying the latter in front of the larger body and 'negative' representing the reverse. The longitudinal and lateral separations are defined as per the following ratios:

$$\text{Longitudinal Separation Ratio, RLong} = \frac{\text{Distance SUBOFF nose tip to origin}}{\text{L}_{\text{Larger Submarine Body}}} \quad 3.1$$

$$\text{Lateral Separation Ratio, RLat} = \frac{\text{Lateral Separation Gap}}{\text{D}_{\text{Larger Submarine Body}}} \quad 3.2$$

Figure 3.14 shows the front view arrangement of the model configuration. The AUV model was located with the vertical distance from the calm free surface to the centreline of the SUBOFF model being 2.33 times the SUBOFF diameter. Previous work with this model shows that at this depth the free surface effects are negligible (Renilson et al. 2011). The larger submarine body was also positioned with the vertical distance from the calm free surface to its centreline as 2.33 times the SUBOFF diameter.

The diameter of each hull was limited by the Towing Tank dimensions. For example, the models must be sufficiently large to accommodate the required force balances and provide sufficient force and moment magnitudes to record sensible data, while being sufficiently small to fit within the Towing Tank without causing blockage or encroaching into the boundary layer regions of the tank. Due to the constraints imposed by the Towing Tank dimensions, the larger body diameter was limited to 2.23 times the diameter of the smaller body. This ratio is lower than some real world scenarios. The EFD results have been used to validate the CFD for the tested cases. Once this was achieved, the CFD was used to predict interaction forces and moments for more realistic cases.

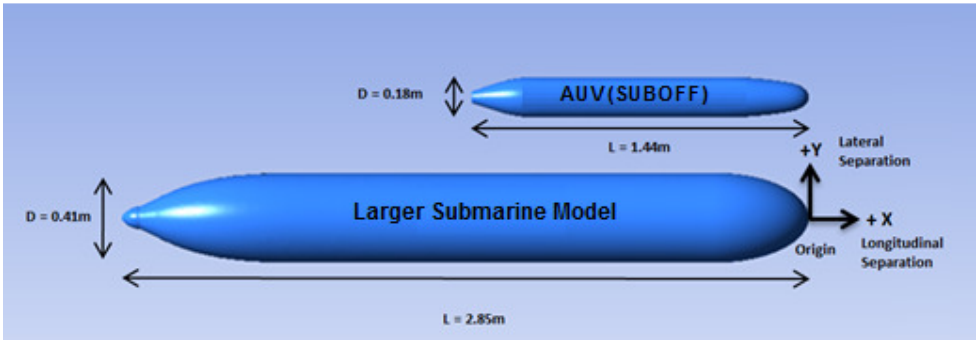

Figure 3.13**:** Illustration of the arrangement for both EFD and CFD (plan view).

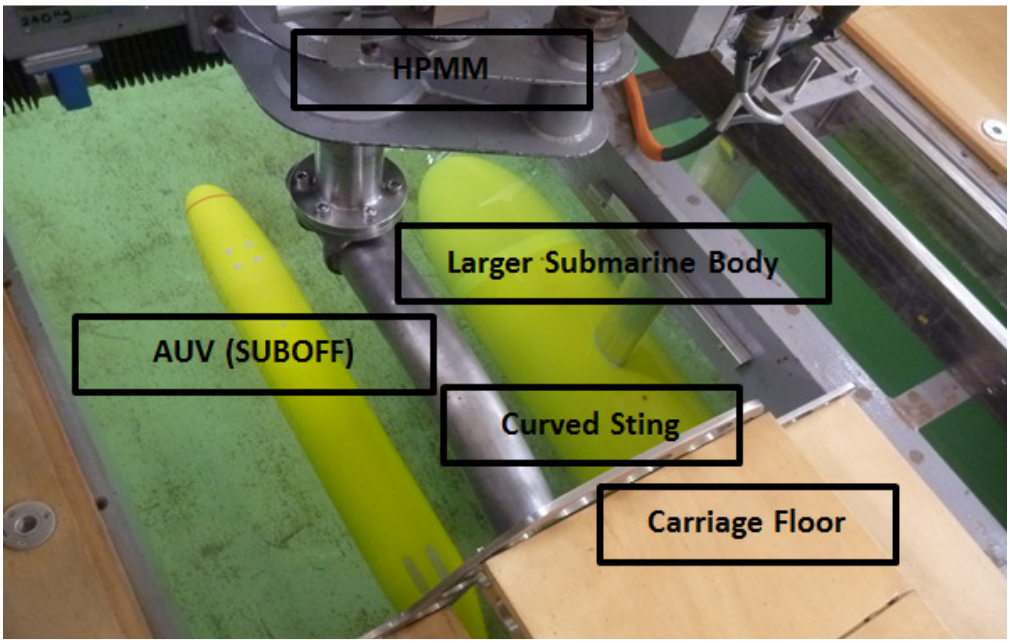

Figure 3.14: Illustration of the arrangement for both models submerged.

Table 3.1: Test program.

Condition	Longitudinal Separation Ratio	Lateral Separation Ratio	Reynolds Number ($x10^5$)
1-9	0.02	2.68, 3.03, 3.38, 4.09	4.04, 8.08, 13.74, 16.16, 19.39
10-13	0.16	2.68, 3.03, 3.38, 4.09	4.04, 8.08, 13.74, 16.16, 19.39
14-17	-0.26	2.68, 3.03, 3.38, 4.09	4.04, 8.08, 13.74, 16.16, 19.39
18-21	-0.18	2.68, 3.03, 3.38, 4.09	4.04, 8.08, 13.74, 16.16, 19.39

3.6 Instrumentation

3.6.1 Load Cells

The SUBOFF model was fitted with two 6-DOF MC3-6-100 AMTI waterproof load cells; one forward of midships and the other aft of midships (refer to Figure 3.13). The principal load cell specifications are provided in Table 3.2.

Table 3.2: Load cell specifications.

Model	Serial Number	Capacity x-direction	Capacity y-direction	Position
[-]	[-]	[N]	[N]	[-]
AMTI	M3631	222	222	Fwd
AMTI	M3633	222	222	Aft

The load cells were calibrated twice during the testing and included all items of the measurement chain, including signal conditioner, amplifier, filter and analogue to digital converter. This was done by applying an incremental load and recording the output voltage. The range of calibration exceeded the range of values measured in the experiments and the calibration factors varied less than 0.5% over the entire test program.

In cases where the load cells experienced loads in multiple directions, tests were conducted to ensure that cross load did not adversely affect the force measurements. For example, calibrations were performed for side force both with and without a vertical force applied to ensure that the calibration factor was not influenced by the vertical force. It was found that the error due to the load in the perpendicular axis was negligible.

An assessment of the load cells used in this testing application was made by considering the range of forces measured on the AMC SUBOFF model. There is

limited choice of load cells with a suitable range capacity available at the AMC Towing Tank to be used in this type of experiment due to the requirement that the system is completely waterproof. This has resulted in the selection of an AMTI 6-DOF 100lb load cell with a 222N capacity in the x direction and a 222N capacity in the z direction. The maximum loads measured in this series of testing were 12N in surge and 10N in heave representing 5.41% and 2.25% of the respective load cell axis capacity. An investigation was conducted to source waterproof load cells of suitable physical size with a more appropriate maximum load range, however nothing suitable was found.

The speed of the towing carriage was measured using a Red Lion rotary pulse generator attached to a dedicated wheel.

The signals from each instrument were recorded using a computer via a National Instruments AT-MIO-16E10 Multifunction Data Acquisition Card, which was controlled by in-house data acquisition software.

3.7 Experimental Setup

A series of tests were conducted on the SUBOFF model prior to undertaking the proper test program to determine if the model was at zero angle of attack. This was conducted by varying the angle of attack by small angles (bow to port through bow to starboard) to find the position where the side force was negligible on the SUBOFF. The angle of attack where the side force converged to a minimal value was taken as the test position. A visual check was performed to confirm.

The alignment of the larger model was determined by measuring its location relative to the SUBOFF's test position. The alignment of the model in the vertical plane was assessed by sighting through an inspection window in the side of the Towing Tank.

The experimental setup is shown in Figure 3.15, clearly illustrating the locations of the AUV (SUBOFF) and the larger submarine body (AMC-11-21) for the case with

0.16 longitudinal and 3.03 lateral separation ratios. The forces on the latter were not recorded, as the objective of the work was to quantify the forces and the behaviour of the smaller body due to the interaction. A series of tests were conducted in the Towing Tank for the range of lateral and longitudinal separations at different speeds as mentioned earlier in Table 3.1, with the data gathered for each run consisting of the surge force and side force in the forward and aft 6-DOF load cells.

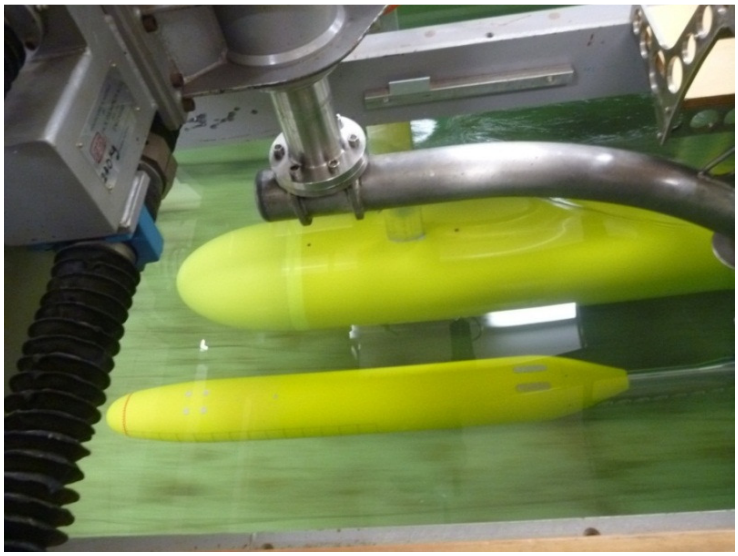

Figure 3.15: Arrangement for the captive model test.

3.8 Experimental Procedure and Data Acquisition

The model tests were performed in a straight line, zero incidence configurations at pre-determined speeds. Initial readings of all instruments were taken prior to each run and were checked between runs to ensure that no notable drift had occurred. The carriage was accelerated to the predetermined speed and the recordings were started at a designated longitudinal location in the tank to maintain consistency. Data acquisition commenced after a constant speed had been reached and the models were at steady state. The sample rate was set at 200Hz with the number of samples recorded varying with the speed of the model. The raw signal was processed through a band-pass filter, an amplifier, and a signal conditioner. A 1 Hz low pass filter was

applied to each force channel. The signal was then sent to an analogue to digital converter to be processed using in house software.

For steady state cases the mean values of each test run were derived afterwards from the time series, selecting a time window where the measurement values had stabilised. Sufficient time was allowed between consecutive runs to achieve calm water conditions.

Leong (2010) provides an overview evaluation of the experimental concepts and the methods and procedures utilised during model tests, as seen in Figure 3.16.

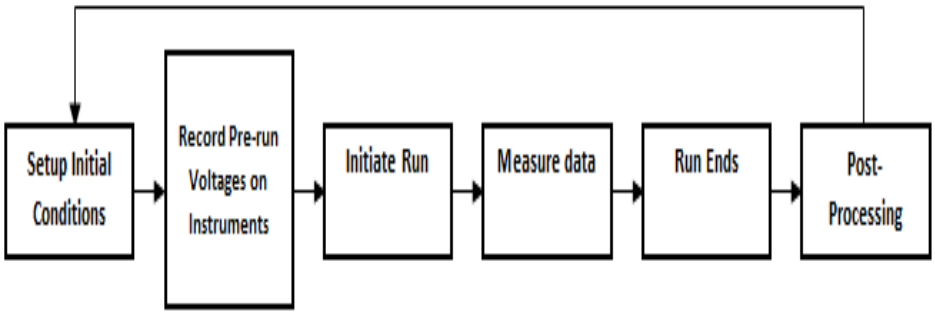

Figure 3.16: Summary of experimental procedure.

3.9 Uncertainty Analysis

An uncertainty analysis on measurements obtained from the experiments was completed using the methods of ITTC 7.5-02 01-02 (1999) and ITTC 7.5-02 02-04 (2002b), which were also used by Van Steel (2010). Single and multiple uncertainties were calculated from a group of four repeated runs under the same condition. For the best determination of uncertainties, ITTC recommends the use of up to 15 repeats in calculations. Uncertainty bars are presented on selected results in subsequent sections of the thesis. Values used in the uncertainty assessment are provided in Appendix B.

Chapter 4

Computational Fluid Dynamics (CFD)

4.1 Background

Computational Fluid Dynamics (CFD) is a fluid prediction tool which combines fluid mechanics theory with computer science to obtain an approximate solution to fluid flow and other related phenomena. In CFD, the partial differential equations that represent the system need to be transformed into a form that enables a numerical solution. The solution of the former involves closed form expressions giving continuous variation of the dependent variables through the domain. In a numerical solution, the continuum of values is separated into a finite number of discrete points, referred to as discretisation. This is done by dividing the domain into a grid, with the grid points being the discrete points. Tu et al. (2008) explains that the process of obtaining the computational solution consists of two stages. The first stage involves the conversion of the partial differential equations and auxiliary conditions into a system of discrete algebraic equations, also known as discretisation. The resulting discrete algebraic equations can then be solved for variables at the grid points through an iterative process. The accuracy of the solution is dependent on the similarity between the partial differential equations and the algebraic equations.

In RANS simulation, the entire fluid domain is meshed and the RANS equations are solved over the individual cell before the variables are approximated at the cell centres. As discussed in Lou et al. (2000), Tu et al. (2008) and Widjaja et al. (2007) a good quality mesh with sufficient density to capture the boundary layers and flow features is essential. In regions where the flow is expected to be complex, the mesh density must be refined to allow the CFD simulations to resolve the flow boundary layers. Husaini et al. (2009) summarized that a good quality mesh will give comparable values to those obtained from compatible experimental work. Nevertheless, the computational results can vary greatly depending on the experience

of the analyst, the settings utilised such as the boundary condition and the turbulence models, and the quality of the mesh model; thus necessitating validation through the experimental work in this study (refer to Chapter 5 for the validation work).

A number of research projects (Sarkar, 1997, Mohammadi, 1997 and Toxopeus, 2008) have focused on numerically or computationally predicting the manoeuvring characteristics of small vehicles such as ROVs or AUVs operating in close proximity to a larger underwater vehicle such as a submarine.

This research work attempts to address this situation, focusing on the following three main areas:

- to enable accurate and efficient prediction of forces and moment acting on the smaller submerged vehicle;
- to predict viscous flow near the small body; and
- to analyse the potential flow around the small body.

Each of these components is necessary to predict the manoeuvring characteristics due to the interaction between two underwater vehicles.

Turbulent flows are significantly affected by the presence of solid boundaries, where the viscosity-affected regions (the boundary layer) have large velocity and pressure gradients. Due to the presence of these solid boundaries, the flow behaviour and turbulence structure are considerably different from free turbulent flows, which must be accounted for when using CFD (Malalasekera et al. 2007). This necessitates a suitable near wall treatment (wall functions or near wall modelling) and corresponding turbulence model in order to appropriately model the boundary layer effects.

4.2 Reynolds-Average Navier-Stokes (RANS) Equations

CFD simulations using Reynolds-Average Navier-Stokes (RANS) equations have proven to be a very useful tool to predict the flow around underwater vehicles such as AUVs and obtain supplementary hydrodynamic information through options such as flow visualisation (Phillips et al. 2010, Tyagi and Sen, 2002 and Zhang, 2010). The RANS equations are used in most commercial CFD packages, including ANSYS CFX, which was used in this project.

RANS CFD simulations have proven to be a powerful design tool in identifying the flow around submerged bodies and predicting the resulting hydrodynamic forces and moments. This method simplifies the Navier-Stokes equations for turbulent flow situations by averaging the different flow components and has been shown to provide reasonably accurate results for steady state flow conditions (Gorski, 2002).

Considering the conservation of mass of the fluid gives the continuity equation for the fluid in the conservation form as,

$$\frac{\partial \rho}{\partial \bar{t}} + \nabla(\rho V) = 0 \qquad 4.1$$

where ρ is the density, V is the velocity, ∇ is the divergence of the vector field, and t is time. Applying Newton's second law, that is the conservation of momentum, to the fluid, the Navier-Stokes equations for compressible Newtonian fluids are obtained as,

$$\rho \frac{du}{dt} = \rho g_x - \frac{\partial p}{\partial x} + \mu * \left(\frac{\partial^2 u}{\partial x^2} + v\frac{\partial^2 u}{\partial y^2} + w\frac{\partial^2 u}{\partial z^2}\right) \qquad 4.2$$

$$\rho \frac{dv}{dt} = \rho g_y - \frac{\partial p}{\partial y} + \mu * \left(\frac{\partial^2 v}{\partial x^2} + v\frac{\partial^2 v}{\partial y^2} + w\frac{\partial^2 v}{\partial z^2}\right) \qquad 4.3$$

$$\rho \frac{dw}{dt} = \rho g_z - \frac{\partial p}{\partial z} + \mu + \left(\frac{\partial^2 w}{\partial x^2} + v\frac{\partial^2 w}{\partial y^2} + w\frac{\partial^2 w}{\partial z^2}\right) \qquad 4.4$$

Where x, y, and z are the body axis Cartesian coordinates in the x, y, z-directions, u, v, and w are the linear velocities in those directions, μ is dynamics viscosity, g is gravitational constant, τ is the shear stress, σ is the normal stress, and p is pressure. Similarly, considering the conservation of energy, by applying the first law of thermodynamics, will give the energy equation. However, in this study the fluid is assumed to be isothermal, thus the thermodynamic equations are eliminated from the solution algorithm.

Other numerical approaches include Direct Numerical Simulation (DNS), Large Eddy Simulation (LES), and Detached Eddy Simulation (DES). These methods involve discretising the Navier-Stokes equations through high order numerical techniques, although more accurate, requires significantly greater computational power compared to an equivalent RANS model (Wilcox, 1994 and Apsley, 2004).

In the transition and turbulent flow regimes, the fluid elements carry out fluctuation in all directions and develop a highly complex flow that is time-varying and random (refer to Figure 4.1(a)). The fluid elements carry out fluctuations in all directions and consist of eddies of varying sizes that continually appear and disintegrate. Eddies produce, diffuse, and dissipate energy within the flow.

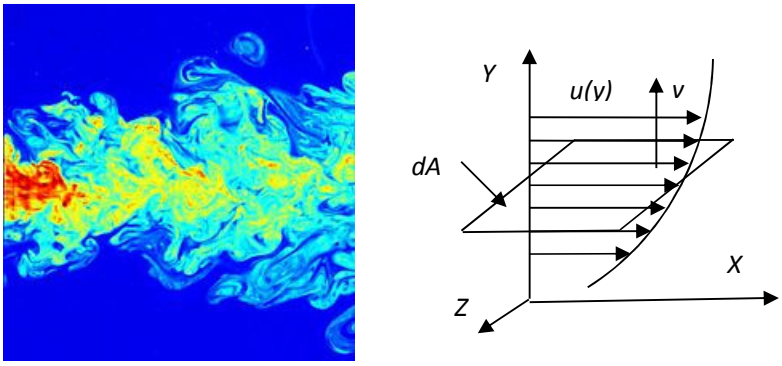

Figure 4.1: Turbulent flow (a) flow visualisation (b) Reynolds stress

Turbulence has flow in all directions. Therefore, a flow stream in the X direction having a velocity of u will also have a velocity in the Y direction, which is v as shown in Figure 1(b). Both u and v will have mean and fluctuating velocities given by,

$$u = \bar{u} + u' \quad (4.5)$$

$$v = \bar{v} + v' \quad (4.6)$$

where the bar ($\bar{}$) denotes the mean component and prime (') denotes the fluctuating component. This fluctuating flow in the XY plane results in an apparent or additional shear stresses (in addition to the stresses in laminar flow) in the XY plane denoted by τ'_{xy}. This together with the equivalent apparent shear stresses due to turbulence in the other two coordinate directions, all referred to as Reynolds Stresses, are defined as,

$$\tau'_{xy} = -\rho\overline{u'v'} \quad (4.7)$$

$$\tau'_{yz} = -\rho\overline{v'w'} \quad (4.8)$$

$$\tau'_{zx} = -\rho\overline{w'u'} \quad (4.9)$$

In order to deal with this unsystematic fluctuation of turbulence, the Navier-Stokes equations are simplified by taking the mean value of the sum of the steady component and fluctuation components, instead of solving the equations directly, thus giving the RANS equations as presented below,

$$\rho\left(\bar{u}\frac{\partial\bar{u}}{\partial\bar{x}} + \bar{v}\frac{\partial\bar{u}}{\partial\bar{y}} + \bar{w}\frac{\partial\bar{u}}{\partial\bar{z}}\right) = -\frac{\partial\bar{p}}{\partial\bar{x}} + \mu\Delta\bar{u} - \rho\left(\frac{\partial\sigma'_x}{\partial\bar{x}} + \frac{\partial\tau'_{xy}}{\partial\bar{y}} + \frac{\partial\tau'_{xz}}{\partial\bar{z}}\right) \quad (4.10)$$

$$\rho\left(\bar{u}\frac{\partial\bar{v}}{\partial\bar{x}} + \bar{v}\frac{\partial\bar{v}}{\partial\bar{y}} + \bar{w}\frac{\partial\bar{v}}{\partial\bar{z}}\right) = -\frac{\partial\bar{p}}{\partial\bar{y}} + \mu\Delta\bar{v} - \rho\left(\frac{\partial\tau'_{xy}}{\partial\bar{x}} + \frac{\partial\sigma'_y}{\partial\bar{y}} + \frac{\partial\tau'_{yz}}{\partial\bar{z}}\right) \quad (4.11)$$

$$\rho\left(\bar{u}\frac{\partial\bar{w}}{\partial\bar{x}} + \bar{v}\frac{\partial\bar{w}}{\partial\bar{y}} + \bar{w}\frac{\partial\bar{w}}{\partial\bar{z}}\right) = -\frac{\partial\bar{p}}{\partial\bar{x}} + \mu\Delta\bar{w} - \rho\left(\frac{\partial\tau'_{xz}}{\partial\bar{x}} + \frac{\partial\tau'_{yz}}{\partial\bar{y}} + \frac{\partial\sigma'_z}{\partial\bar{z}}\right) \quad (4.12)$$

Due to the coupling of the fluctuating and mean motions, the Navier-Stokes equations yield additional Reynolds stress terms and additional unknowns, which are dependent on the turbulent fluctuations. Thus, additional equations are required to enable closure of the set of equations, which are provided through turbulence models that links the

turbulent shear stresses with the mean fluid motion. A comprehensive description of RANS equations and related theories are given in Tu et al. (2008).

4.3 Turbulent Boundary Layer

All fluid flows are described as either laminar, turbulent, or at a transition between the two (refer to Figure 4.2). Laminar fluid flows over a body have a smooth velocity gradient. The flow velocity is zero at the wall and gradually increases as it moves away until eventually reaching the free stream velocity. The velocity of each layer or streamline is affected by the shear stresses between the fluid particles of the layer directly beneath. Due to the steady, systematic nature of laminar flow, computational prediction is performed with relative ease. In the transition and turbulent flow regimes, the fluid elements unsystematically fluctuate in all directions developing a highly complex flow that is both time-varying and random.

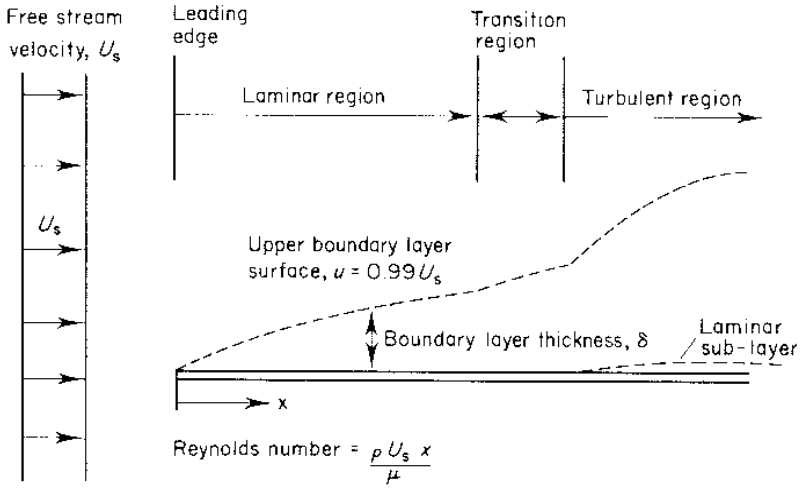

Figure 4.2: Boundary layer on a flat plate immersed in a fluid. (Douglas, Gasiorek, and Swaffield, 2000).

Turbulent flow can develop in the free stream or be induced by surface roughness. Most engineering fluid flow problems involve turbulent flow, making computation and fluid flow prediction exceptionally difficult. By introducing turbulence models it

is possible to simplify turbulent flow in order to reduce computational time whilst still providing solutions to an acceptable level of accuracy.

Turbulence models are used by many CFD programs to capture the flow within the boundary layer. This is done by dividing the boundary layer into three sub layers as shown in Figure 4.3. In the viscous wall layer, the flow is not yet influenced by the free stream and is dominated by viscous stresses. This layer is extremely thin and the sheer stress can be assumed to remain approximately constant and equal to the wall shear stress throughout the layer.

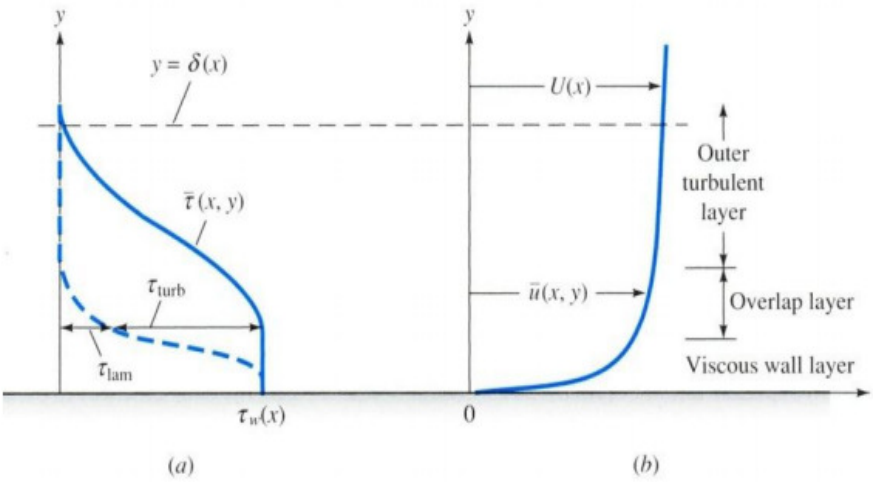

Figure 4.3: Velocity and shear distribution near a solid boundary (a) shear (b) velocity. (White, 2007).

In the overlap layer both viscous and turbulent forces are present. The more dominant force depends on the Reynolds number, the surface roughness condition, the initial turbulence intensity of the flow, and the pressure distribution over the body. If the viscous forces dominate within the overlap layer, the flow will remain laminar and the thickness of the layer will decrease. However, if the turbulent forces are dominant, momentum will transit the flow into turbulence and the thickness of the layer will increase.

In the outer turbulent layer the flow is generally turbulent and the flow is no longer influenced by the viscous stresses of the wall. A brief derivation of the equations used

to predict the flow in each layer is presented in Appendix A – Near Wall Modelling Theory.

As stated earlier, the inclusion of the Reynolds Stresses to the Navier Stokes equations introduces additional unknowns, requiring additional equations to solve for all unknowns. Therefore, a variety of turbulence models are introduced for closure of the RANS equations. The different turbulence models used within CFD simulations have their own applications, advantages, and disadvantages. Thus, it is important for the CFD user to understand the most suitable turbulence model for the flow being analysed to obtain accurate results coupled with computational efficiency. Some common turbulence models are briefly explained in the next sub-section. The following are some relevant definitions and explanations.

The thickness of the viscous wall layer (δv) is given as,

$$\delta_v = \frac{v}{u_\tau} \tag{4.13}$$

where u_τ is the wall friction velocity, which is the characteristics velocity for turbulent flows at a given wall shear stress (τ_w) and is defined as,

$$u_\tau = \sqrt{\frac{\overline{\tau_w}}{\rho}} \tag{4.14}$$

The stretched or characteristic wall coordinate (y^+) for the wall layer is given by,

$$y^+ = \frac{y}{\delta_v} \tag{4.15}$$

It can be shown (Schlichting and Gersten, 2000) that the velocity distribution within the wall layer is given by,

$$\frac{du^+}{dy^+} + \tau_t^+ = 1 \tag{4.16}$$

where $u^+ = \bar{u}/u_\tau$, $\tau_t^+ = \tau_t/(\rho u_\tau^2)$, and τ_t is the turbulent shear stress. The boundary conditions at the wall being $y^+ = 0$ and $\partial u^+/\partial y^+ = 1$. Since the solutions for outer layer and wall layer have to match up where they meet, there exists an overlap layer as shown in Figure 4.3 that agrees to the boundary conditions of the two adjacent layers. It has been shown that for the overlap layer at high *Re*, the velocity distribution is given by (Schlichting and Gersten, 2000),

$$\hat{y}\frac{du^+}{d\hat{y}} = \frac{1}{\kappa} = constant \qquad 4.17$$

where $\hat{y}$ is an intermediate coordinate for the overlap layer and the constant κ is the *Karman Constant* and is found through experiments as 0.41. At the boundary of the wall layer the velocity is given by,

$$\lim_{y\to\infty} u^+(y^+) = \frac{1}{\kappa}\ln y^+ + C^+ \qquad 4.18$$

with the constant C^+ depending on wall roughness and is 5.0 for a smooth wall. The above equation is referred to as the *logarithmic overlap law*, which describes how the velocity profile $u^+(y^+)$ behaves as $y^+ \to \infty$. Most boundary layer situations in turbulent flow at high *Re* exhibit a thin wall layer with the same velocity profile. Thus, the above rule applies to these situations, and is therefore referred to as the *universal law of the wall* or the *wall function* (Schlichting and Gersten, 2000). The distributions of $u^+(y^+)$ and $\tau^+(y^+)$ in the layers obtained through measurements and the above equations are given in Figure 4.4 (a) and (b). Thus, within this region the profiles can be obtained without solving the RANS equations. Beyond this, it follows the equations for the outer layer. For the region close to the wall the velocity profile is,

$0 \le y^+ \le 5$	pure viscous wall layer $u^+ = y^+$
$5 \le y^+ \le 70$	buffer layer $u^+ = y^+ - A(y^+)^4$
$70 \le y^+$	overlap layer $\frac{1}{\kappa}\ln y^+ + C^+$

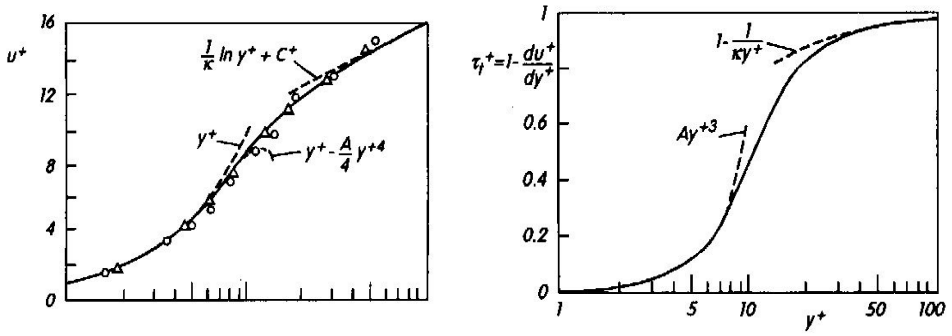

(a) (b)

Figure 4.4: Universal law of the wall (a) velocity distribution $u^+(y^+)$ (b) shear stress $\tau^+(y^+)$ (Schlichting and Gersten, 2000)

When developing mesh models, the treatment of the boundary layer is important as it enables the capture of the flow around the vehicle, with special consideration to areas where there is high curvature, flow separation, stagnation regions, surface irregularities, etc. The actual process will depend on the CFD package, turbulence model utilised, and the modelling and simulation techniques applied by the user. This includes resolving flow into the wall layer by inserting mesh nodes into that region, which is right up to the surface. This is preferred when dealing with areas of concern as identified above. On the other hand, the mesh can be terminated in the overlap layer, allowing the flow and stress within the region close to the boundary to be predicted using the correct wall function approximation defined earlier.

The non-dimensional distance to the wall (y^+) is used in CFD to describe the first mesh cell height for a particular flow conditions, thus directly affecting the solution and flow resolving techniques within the boundary layer region. In this study the ANSYS (2008) recommended method given below is used to calculate the initial first cell height,

$$\Delta y = L y^+ \sqrt{80} Re^{\left(\frac{-13}{14}\right)} \qquad 4.19$$

where Δy is the actual distance between the wall and first node, Re is Reynolds Number based on the length scale, L is the length of vehicle, and y^+ is desired non-dimensionless wall distance.

4.4 Turbulence Models

The simplest of turbulence models is the mixing length model, which assumes the majority of the kinetic energy is stored in the largest eddies. Malalareskera et al. (2007) explains, “If we accept that there is a strong connection between the mean flow and the behaviour of the largest eddies, we can attempt to link the characteristic velocity scale of the eddies with the mean flow properties”. Prandtl (2009) derived an algebraic expression that relates the mixing length of the eddies to the Reynolds stresses. As this method does not require any additional equations, it is also known as a zero equation model.

The next group of models are known as the one equation models, where a transport equation is solved for a turbulent quantity (usually the turbulent kinetic energy) and a second turbulent quantity (usually a turbulent length scale) is obtained from an algebraic expression (Davidson, 2003). A commonly used equation is the Spallarat-Allmaras model. In both of these methods there is still need to specify the mixing length and hence knowledge of the flow must be assumed before the equations are solved.

The two equation models use two transport equations to resolve the unknowns, by determining the eddy lengths and scales by the use of the eddy dissipation ε. This allows the flow to be fully described without any prior knowledge of the flow, as it eliminates the use of mixing length approximations. Davidson (2003) explains, “Two transport equations are derived which describe transport of two scalars, for example the turbulent kinetic energy and its dissipation ε. The Reynolds stress tensor is then computed using an assumption which relates the Reynolds stress tensor to the velocity gradients and an eddy viscosity”. As these models only have two additional transport equations, they remain relatively simple while still fully accounting for the flow.

4.4.1 k-ε Turbulence Model

The k-ε turbulence model is one of the most widely used and validated turbulence models. It has achieved success in calculating a wide variety of thin shear layer and recirculating flows without the need for case by case adjustment of the model constants (Malalasekera et al. 2007). The k-ε turbulence model is a two equation model that uses transportation equations to determine the balance of the kinetic energy of the fluctuations (k) and the energy dissipation (ε). The equations in the model are given as,

For the kinetic energy of the fluctuations (k)

$$\frac{\partial}{\partial t}(\rho k) + \frac{\partial}{\partial t}(\rho k u_i) = \frac{\partial}{\partial t}\left[\left(\mu + \frac{\mu_t}{\sigma_k}\right)\frac{\partial k}{\partial x_j}\right] + P_k + P_b - \rho\epsilon - Y_M + S_k \qquad 4.20$$

For the energy dissipation (ε)

$$\frac{\partial}{\partial t}(\rho \epsilon) + \frac{\partial}{\partial t}(\rho \epsilon u_i) = \frac{\partial}{\partial t}\left[\left(\mu + \frac{\mu_t}{\sigma_\epsilon}\right)\frac{\partial \epsilon}{\partial x_j}\right] + C_{1\epsilon}\frac{\epsilon}{k}(P_k + C_{3\epsilon}P_b) - C_{2\epsilon}\rho\frac{\epsilon^2}{k} + S_\epsilon \qquad 4.21$$

where S is the modulus of the mean rate of strain tensor, $C_{1\epsilon}$ = 1.44, $C_{2\epsilon}$ = 1.92, $C_{3\epsilon}$ = -0.33, σ_k = 1.0, and σ_ϵ = 1.3.

It uses a wall function to capture the boundary layer allowing a course mesh within the boundary layer. The boundary layer should be developed that the y^+ is between 30 and 100 to ensure correct predictions from the wall function (Tu et al. 2008). This allows for mesh refinement in other areas of interest as a large amount of elements are not required to capture boundary layer effects.

The main advantages of the model are: it is well established and the most widely validated turbulence model requires significantly lower number of nodes near the wall due to the use of wall functions, and the simplest and most robust turbulence model where only initial and/or boundary conditions are required. The disadvantages are: limited to flow types which have been validated for, fails to fully capture the boundary layer, and not suited for geometries with high curvature due to under

prediction of separation. It is best used for applications with flow over bodies with low curvature and free stream analysis around a body.

4.4.2 k-ω Turbulence Model

Similarly to the k-ε model, k-ω uses the kinetic energy (k) function. However, instead of using the energy dissipation (ε) it uses the energy frequency (ω) to find the eddy viscosity. This method is integrated all the way to the wall thus eliminating the need for a wall function. Due to the assumptions this method is based upon, a small ω must be assumed as the flow approaches the free stream. This can cause errors within the free stream results.

$$\bar{u}\frac{\partial \omega}{\partial x} + \bar{v}\frac{\partial \omega}{\partial y} = \frac{\partial}{\partial y}\left(\frac{v_t \partial \omega}{Pr_\omega \partial y}\right) + \alpha\frac{\omega \tau_t}{k\rho}\frac{\partial \bar{u}}{\partial y} - \beta\omega^2 \qquad 4.22$$

where, $\bar{u}$ is the mean velocity in x direction, $\bar{v}$ is the mean velocity in y direction, Pr_ω is constant (usually 2), α = 5/9, β = 3/40, τ_t is the turbulent shear stress, and v_t is the eddy viscosity.

The advantages of this method are: it captures the complete boundary layer flow field and is well suited for complex curvature and wake. Meanwhile, the disadvantages are: it requires a fine mesh near the wall in order to accurately capture the boundary layer, accuracy decreases as the flow approaches the free stream and requires a small y^+ value as no wall function is typically used (Note: newer CFD software versions include wall functions enabling greater flexibility). The model is ideal for boundary layer analysis and for surfaces with high curvature, although it can have issues further away from the surface.

4.4.3 Shear Stress Transport (SST) Model

To overcome the shortcomings of both the k-ε and k-ω methods, Menter (1994) proposed a model that combined the accuracy of the k-ω model near the wall and the

k-ε model in the free stream. Essentially, a hybrid of both models is used with the introduction of blending functions to ensure a smooth transition between the two models. The SST model combines the standard k-ω for more accurate near wall treatment with an automatic changeover from a wall function to a low Re formulation based on grid spacing and the standard k-ε which is excellent in predicting the flow behaviour in the free stream.

The differences between these turbulence models were stated in Jade et al. (2010) where the advantages of both k-ε and k-ω models are driven from the SST model. Chng et al. (2007) explained that although SST requires higher simulation run time and a finer grid at the boundary layer compared to the k-ε and k-ω models, their disadvantages are compensated by less work on the grid adaption in order to accurately capture the flow features for complex geometries.

The advantages offered are: the models accurately predict the flow within the boundary layer and in the free stream captures the separation effectively by fully solving the boundary layer and widely applicable to many flow analysis types. The disadvantages are: SST can lack the flexibility to adjust to the required method at the correct location, involves extra terms in the RANS equations increasing the solving time, and requires a small y^+ value as no wall function is used. (Again it should be noted that newer versions incorporate the ability to use a wall function depending on the mesh density and operation parameters). This model is applicable to most CFD applications, with strong credential for boundary layer analysis and flow past bodies. Therefore, the SST was the main turbulence model used in the project.

4.5 Discretisation

Discretization is essentially converting the partial differential equations (i.e. the RANS equations) and auxiliary conditions into a system of discrete algebraic equations (Tu, 2008). In all cases of discretisation process, the solutions are approximate (MARNET-CFD, 2002). The Control volume method is based on the integral form of the conservative transport equations applied to the control volumes.

The finite-volume method (ANSYS-CFX) adopted in the CFD package used in this study discretises the integral of the conservation equation directly in the physical space. The computational domain is divided into finite number contiguous volumes. The domain is divided into a number of control volumes, with the variables within the volumes calculated at their centroids, and the use of interpolation to obtain values at the boundaries. Quadrature formulae are applied to approximate the surface and volume integrals, giving algebraic equations for each control volume in terms of adjacent nodal values. As the finite volume method works with the control volumes and not at grid intersection points, it has the capacity to accommodate any type of grid. Thus, the finite-volume method is capable of computing both structured and unstructured meshes (Tu, 2008). It also does not require a body fitted coordinate system for mesh transformation.

As stated earlier, the control volume integration is the key of this method. Within the control volume, the bonding surface areas of the element are linked to the derivatives of the flow field variables. The volume integral is carried out by applying Gauss' divergent theorem to the transport equation resulting in a discretised form of the equation. This is then expressed in an algebraic form, which is solved through approximation process.

4.6 CFD Simulation Setup

4.6.1 Geometry

The geometry used in this study was kept the same as that used in the experimental work (Chapter 3). The model scale numerical simulations were conducted with various forward speeds, lateral separations, and longitudinal separations as shown in Table 1.1 in Chapter 1. The definitions of these ratios are given in Chapter 3.

The SUBOFF geometry used to represent the smaller AUV has a diameter of 0.18m and a length of 1.44m giving a length to a diameter (L/D) ratio of 8. Initial CFD work

was carried out in conjunction with a larger body having diameter ratio of 2.23:1 in comparison to the SUBOFF geometry, which has similar dimensions to the vehicles tested in Chapter 3. This enabled the CFD simulation model to be validated against the experimental results obtained and presented in Chapter 3, while providing sufficient difference between the sizes of the two vehicles to enable the study to quantifying the flow and pressure regime around the larger body and its effects on the smaller vehicle. This initial diameter ratio was due to limitations imposed by the dimensions of AMC's towing tank and force balance arrangement used in the captive model testing. The smaller model had to be large enough to accommodate the force balance and generate sufficiently large forces and moments to enable the recording of sensible data, while together the two vehicles had to be sufficiently small to fit within the towing tank without causing blockage or encroaching into the boundary layer regions of the tank.

The validated CFD model was then be used to simulate the interaction between vehicles having a diameter ratio of 12:1 by scaling up the larger vehicle, which is representative of an AUV operating in close proximity to a typical diesel electric submarine. This enabled the interaction effects and the location of adverse pressure regimes to be quantified, thus providing suitable operational envelop for the AUV around the submarine hull.

In order to carry out validation, the SUBOFF geometry within the 2.23:1 simulations were modelled with and without the aft mounted sting (the latter is shown in Chapter 3), which enabled the simulations to replicate the effects of the sting on the pressure and flow profile of the SUBOFF model experienced in the experimental work. This includes the increase in the aft pressure field especially on the upper side of the vehicle due to the stagnation point created by the vertical sting attachment, while the additional length at the aft end due to the horizontal force balance (refer to experimental configuration in Chapter 3 for details) moves the pressure recovery further aft.

4.6.2 Domain Generation

As the testing was conducted within AMC's Towing Tank (AMCTT), the CFD domain was setup to replicate the tank as closely as possible. This ensured replication of any effects due to blockage, bottom proximity, or wake reflection. Based on validated simulations conducted by Wilson-Haffenden (2009) and Ackermann (2008), a domain of three length forward and five lengths aft of the model were used (refer to Figure 4.5). Wilson-Haffenden (2009) noted that although it is advisable to have a larger domain aft of the body, the additional refining required in the far field region aft of the vehicle to avoid high aspect ratio elements adversely affected the computational time with marginal gains in accuracy. The domain geometry was created within ANSYS Workbench by importing the respective geometries of the two vehicles.

As stated earlier, the SUBOFF geometry for the 2.23:1 ratio was modelled with and without the aft mounting sting, with the former enabling validation against experimental data. The 12:1 model was modelled without the sting, as it was developed from the validated mesh model.

4.6.3 Boundary Condition

For the 2.23:1 ratio simulation, in order to ensure that the simulation accurately represented the experimental configuration for validation purposes, the tank and vehicle conditions were applied to all relevant boundaries, including the surfaces of the domain and the models. The fluid domain in this study was created based on dimensions of the towing tank providing a true representation of the tank (refer to Figure 4.5).

An inlet was created at the forward end of the domain where the flow velocity was defined as purely axial with initial medium intensity turbulence (5%). The aft end of the domain was defined as an opening with zero pressure outlets. A no-slip wall was assigned to the vehicle surfaces (both for the larger body and the SUBOFF geometries), while the bottom and outer (side) surfaces of the domain were defined as

no-slip walls to represent the tank walls. This enabled the influence of the boundary layer regions of the tank to be replicated.

Once the mesh model was validated, the sting was removed to eliminate its influence on the interaction between the vehicles, while the top, bottom, and outer surfaces of the domain were all defined as free-slip walls. The free-slip condition assumes no shear force, eliminating any wall effects, thus representing the interaction between vehicles in unrestricted waters.

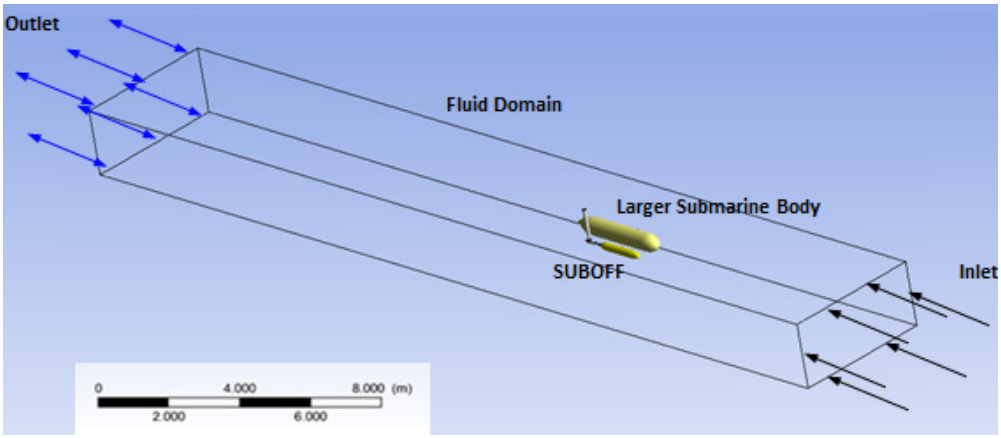

Figure 4.5: CFD Simulation Domain.

4.6.4 Mesh Quality

The quality of the mesh plays a direct role on the solver convergence and solution of every CFD simulation, regardless of the flow solver used. In addition, the solver will be more robust and efficient when using a well-constructed mesh.

Mesh generation constitutes one of the most important steps during the pre-processing stage of a CFD analysis. This involves the subdivision of the domain into a number of smaller, non-overlapping subdomains in order to solve the flow physics within the domain geometry resulting in the generation of a mesh (grid) of cells (elements or control volumes) (Tu et al. 2008). Essentially the discrete values of the variables within each volume, such as velocity, pressure, temperature, and other parameters, are calculated at their centroids, with interpolation used to obtain values at the boundaries

to transfer from node to node in order to describe the fluid flow. It is for these reasons that the selection of gridding technique is extremely important, as the quality of the grid can have a significant influence on the accuracy of results as well as the stability of the simulation. It is therefore imperative that the user understands the strengths and limitations of the different meshing methods and the applicability of each to various geometries and flow fields.

Structured grid methods take the form of a regular repeated pattern referred to as a block (Fell, 2009 and Lou et al. 2000). This grid makes use of quadrilateral elements in 2D and hexahedral elements in 3D in a rectangular array. The vertices of an element are addressed by a triple of indices. As each vertex is defined by the indices, advanced structured grid generators utilise sophisticated elliptic equations to optimise the shape of a mesh for orthogonally and uniformity. In contrast, unstructured mesh elements are assembled cell by cell in a position of best fit with no continuity of mesh lines required (Ackermann, 2008). The connectivity information for each cell face is therefore stored in a table. The most typical cell shape is that of a tetrahedron, but other forms including hexahedral cells may also exist. Unstructured grids adapt well to geometries and flow fields with high curvature. The key advantages of using unstructured mesh are:

- automated grid generation requires significantly less effort by the user to define the mesh;
- able to generate a valid mesh for most geometry; and
- well suited to inexperienced user and still deliver sufficiently accurate results.

For this research, unstructured grids were used to validate and predict the interaction effects through CFD simulations.

As discussed in Widjaja et al. (2007) and Tu et al. (2008), the quality of a mesh is determined by the shape of its individual cells and their capability to correctly predict the flow. This can be ascertained by checking mesh quality parameters prior to simulation, verification of the simulation mesh through mesh independent studies and flow visualisation, and validation against experimental or existing data. For this

analysis, a semi-automated unstructured mesh was applied on the SUBOFF and the larger body as shown in Figure 4.6 and Figure 4.7 (figures are cropped sections of the bodies to showcase the mesh). The pre-simulation checks included some key factors that affect the quality of each element, which included the level of skew, aspect ratio, element volume, minimum angle, and determinants.

The generated mesh had a maximum and minimum element volume of 1.08E-02 m^3 and 1.50E-12 m^3 respectively, indicating a stable mesh with no inverted elements. The minimum angle within each element was approximately 22 degrees, which was greater than both the required minimum of 9 degrees and the preferred minimum of 18 degrees as specified by ANSYS (2011). For areas of high curvature such as the forward and aft end of the SUBOFF model, a minimum angle of approximately 22 degrees was considered satisfactory. The minimum determinant of the elements within the mesh was approximately 0.79, which easily exceeded the required and recommended minimum determinant values of 0.20 and 0.40 respectively (ANSYS, 2011).

Each CFD solver will have different tolerances for various mesh parameters, which must be met to ensure a stable simulation and accurate results. As the initial mesh for the fluid domain clearly exceeded ANSYS recommendation, the mesh was deemed acceptable to commence verification and validation studies.

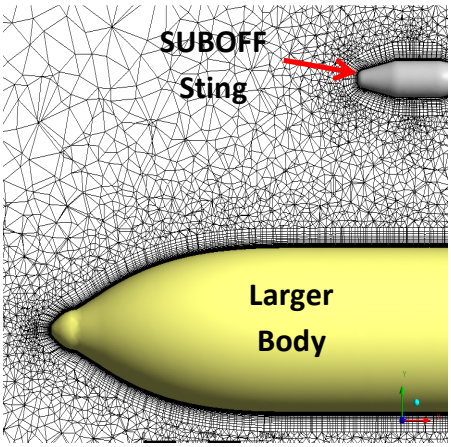

Figure 4.6: Mesh grid stern section with ratio 2.23:1.

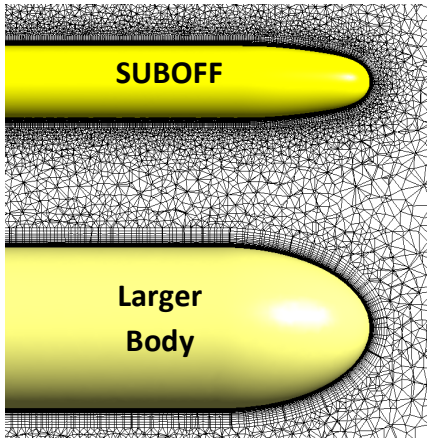

Figure 4.7: Mesh grid forward section with ratio 2.23:1.

4.6.5 Mesh Model

In order to obtain good CFD results, it is essential to have a well laid out grid around a clearly defined geometry. Therefore, the meshing process should include a clear and logical refinement strategy to improvise the capability of the grid to capture the flow generated around the vehicles. Thus, the mesh surrounding each vehicle was divided into the following four sections:

- forward region;
- aft region;
- surrounding body; and
- interaction zone.

The forward and aft sections required finer mesh due to larger pressure/velocity gradient compared to the midship section due to the larger curvature of the surface, which would also be prone to flow separation. The interaction zone too required fine mesh due to the variations in flow and pressure influenced by the interaction as well as the relatively small gap between the vehicles. The area surrounding each vehicle required a sufficient number of prism layer cells to ensure that the boundary layers around the vehicles are well resolved.

The mesh was developed through the following iteration process in order to achieve a suitable mesh domain to:

i. identify the AUV geometry shape used;
ii. create the domain around the geometry;
iii. create mesh topology;
iv. identify the mesh generation method and generate mesh;
v. analyse the mesh quality and refine the mesh method and the mesh;
vi. finalise the mesh and run the simulation;
vii. check the results for convergence, reliability, and accuracy of parameters during the simulation, and if required upgrade mesh topology repeating the process until convergence; and

viii. analyse the results and match with comparable data, repeating steps as required until results are within acceptable error intervals.

4.7 Grid Dependence Study

A grid dependence study was carried out for each individual section to optimise the local mesh, before conducting a study for the combined domain to obtain the most efficient and accurate mesh combination. A number of mesh densities and sizes were tested, with both parameters gradually increased with the drag and side forces and the yaw moment of the bodies monitored until acceptable convergence was achieved, i.e. the change in the results is less than 5% for an increase of mesh density by 50% (Tu et al. 2008). These were carried out in conjunction with an analysis of the flow regime within the domain to ensure that the mesh is capable of accurately capturing the flow around the vehicles, with emphasis on areas of curvature, separation, and stagnation. The turbulence model used in the simulations was SST.

Figure 4.8 shows the changes in the drag coefficient for different meshes sizes from 0.15 to 2.4 million. For the grid dependence study, the SUBOFF was fixed at longitudinal and lateral separation ratios of 0.34 and 3.06 respectively. The results deviated approximately 52% when the mesh density was increased from 0.15 million elements to 1.5 million elements, but only 5% when the grid density was further refined to 2.4 million elements. The 2.4 million element mesh was used in this investigation in order to obtain better flow visualisation and wake capture, although the 1.5 million element mesh is sufficiently accurate to obtain the hydrodynamic coefficients of the vehicles. The side force coefficient and yaw moment coefficient with respect to the mesh density in Figure 4.9 and 4.10 respectively show a similar trend to the drag force coefficient confirming the above. Therefore, the 1.5 million element mesh was deemed sufficiently accurate for the investigation.

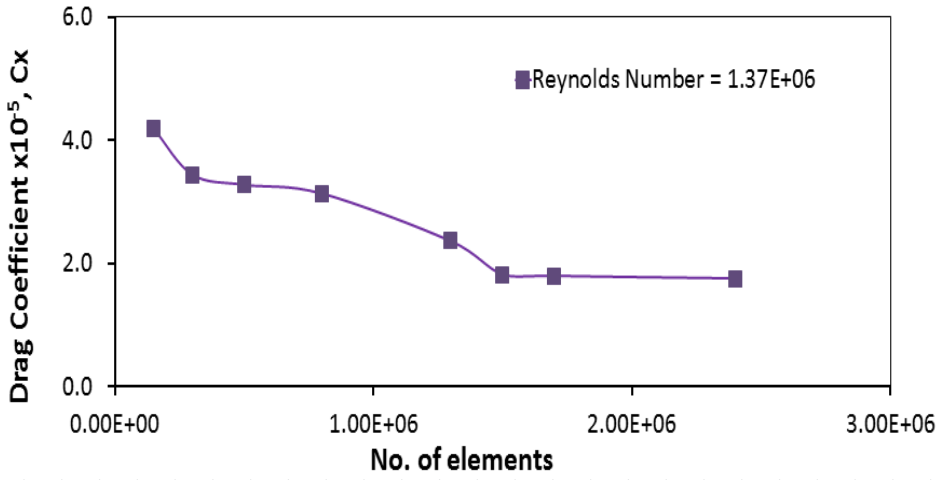

Figure 4.8: Drag coefficient for different mesh sizes for the SUBOFF at longitudinal and lateral separation ratios of 0.34 and 3.06 respectively.

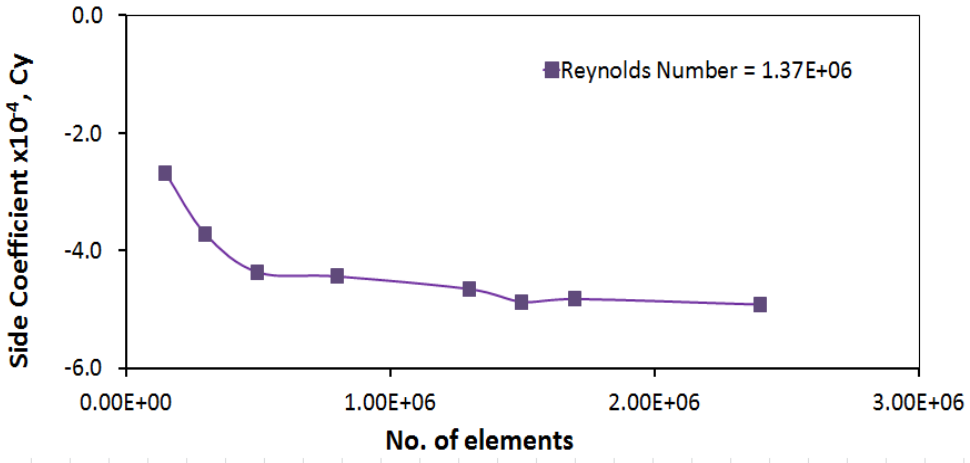

Figure 4.9: Side coefficient for different mesh sizes for the SUBOFF at longitudinal and lateral separation ratios of 0.34 and 3.06 respectively.

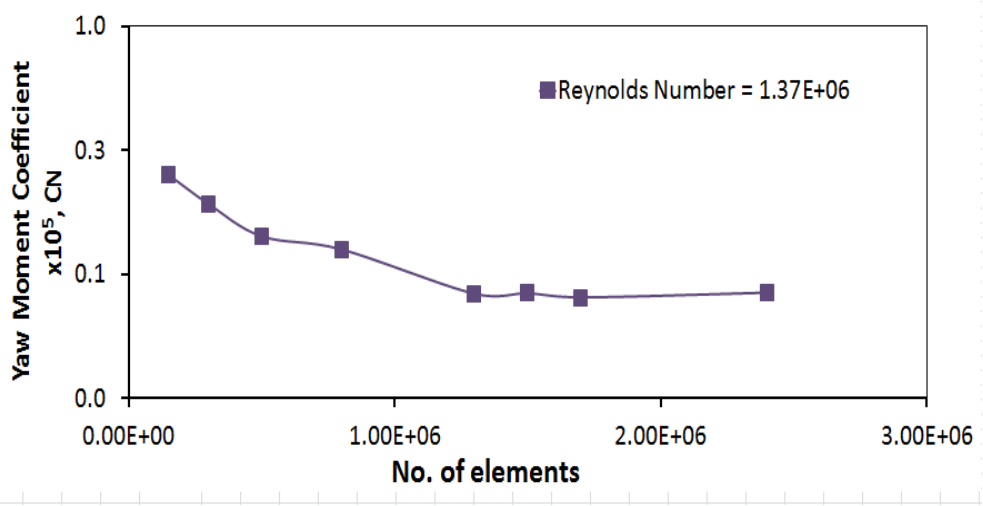

Figure 4.10: Yaw moment coefficient for different mesh sizes for the SUBOFF at longitudinal and lateral separation ratios of 0.34 and 3.06 respectively.

4.8 y^+ Sensitivity

A y^+ study was carried out to investigate the dependency of the drag and side predictions with respect to y^+. To validate the results, a comparison was done using the result obtained on the SUBBOFF geometry from the experimental work at a lateral separation ratio of 4.12, longitudinal separation ratio of 0, and Re = 1.62E+06.

From the experimental work, the drag and side forces on the SUBOFF were 1.877N and -0.4041N respectively. Figure 4.11 and Figure 4.12 show the relative error in the drag and side forces against the experimental values at seven different values of y^+ using the SST turbulence model. At the smaller y^+, the drag and side forces percentage differences compared to the experimental values were 13.1% and 3.1% respectively. As the y^+ increases from five to 20, the percentage difference for drag gradually decreases while the side force increases.

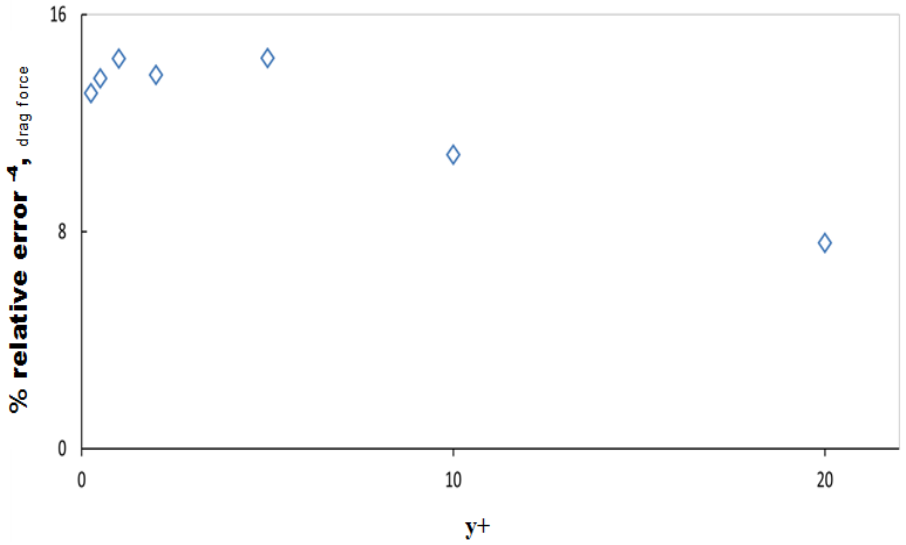

Figure 4.11: Drag force relative error vs. y^+ at the longitudinal separation 0, lateral separation ratio 3.06, and Reynolds Number 1.62E+06.

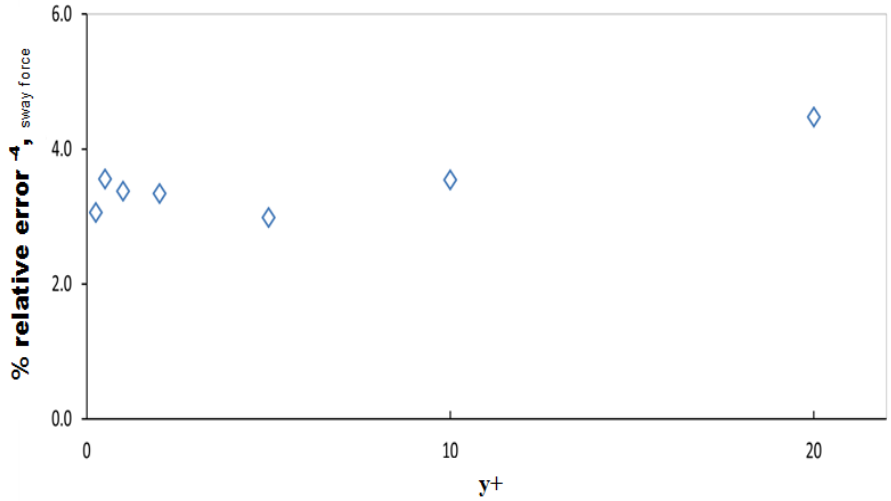

Figure 4.12: Side force relative error vs. y^+ at the longitudinal separation 0, lateral separation ratio 3.06, and Reynolds Number 1.62E+06.

The results show that the drag and side force predictions were sensitive to the wall treatment used. The low Re wall treatment model used to resolve the boundary layer gave results that were in close agreement for y^+ values of less than two. Increasing variation in the predictions were observed as the y^+ increased beyond five. At the y^+ of 20, which relied on the wall function model, the results were found to have differences of up to 45% compared to the predictions at y^+ of one. Although the

percentage difference to the y^+ of 1 solution for drag gradually decreases while the side force increases, the y^+ of 1 solution deemed to be more accurate as it explicitly models the boundary layer around the model. The wall function, which reduces the computational requirement, is desirable only if it matches closely to the y^+ of 1 solution. Thus, it was concluded that the wall function model is insufficiently accurate for the purpose of this study. Thus, the maximum y^+ of the first mesh layer around the vehicles for the simulation runs presented for the remainder of this thesis were maintained below two as it was a close agreement of the y^+ of 1 solution.

Chapter 5

Results and Discussion

5.1 General

In this Chapter, the influence of Re, together with the various lateral and longitudinal separation ratios, on the hydrodynamic coefficients of the AUV (SUBOFF geometry) in close proximity to the Larger Submarine body are examined. The interactions between the two underwater bodies were investigated via both CFD and EFD for a diameter ratio of 2.23:1, and via CFD for a diameter ratio of 12:1 at different longitudinal and lateral separations, and a range of speeds. As both experimental and computational methods have their own avoidable and unavoidable uncertainties, it is essential to validate and compare the CFD and EFD results for better prediction.

The combination of CFD and EFD for the diameter ratio 2.23:1 study also allowed validation of the CFD methodology to be established and to provide confidence in the CFD predictions for the diameter ratio 12:1 work. In addition to the estimates of the coefficients, flow visualisation of the CFD results was conducted to identify a suitable trajectory for the AUV to approach and leave the larger body. With comparison between the diameter ratios and the effects of lateral and longitudinal separations, the trajectory which gives the lowest interaction forces and moment are presented and their implications to AUV Submarine interoperations are discussed.

5.2 Investigation Programme

The variables investigated included the length based coefficients of drag and side forces, and the yaw moment action on the SUBOFF geometry, with the moment calculated at the SUBOFF's centre of buoyancy, at 0.72m aft of the SUBOFF nose tip. The lateral separation and longitudinal separation are taken as the separation gap between the nose tips of the two bodies with 'positive' and 'negative' identifying the

AUV in front of and behind the larger vehicle respectively. The longitudinal and lateral distances are non-dimensionalised as follows:

$$\text{Longitudinal Separation Ratio, RLong} = \frac{\text{Distance SUBOFF nose tip to origin}}{L_{\text{Larger Submarine Body}}} \quad 5.1$$

$$\text{Lateral Separation Ratio, RLat} = \frac{\text{Lateral Separation Gap}}{D_{\text{Larger Submarine Body}}} \quad 5.2$$

Table 5.1: Summary of model parameters

2.23:1 Diameter Ratio (CFD and Experimental)		
	Units	**Descriptions**
SUBOFF	m	diameter: 0.18, length: 1.44
Larger Submarine body	m	diameter: 0.41, length: 2.94
Speed	m/s	0.75, 1.00, 1.50, 2.0
Reynolds number (SUBOFF Length)	- ($x10^6$)	1.21, 1.62, 2.42, 3.23
Longitudinal Separation, RLong.	mm	-2500, -2000, -1500, -1000, 0, 500, 1000, 1500, 2000
Lateral Separation, RLat.	mm	326.5, 398, 543
12:1 Diameter Ratio (CFD)		
SUBOFF	m	diameter: 0.181, length 1.56
Larger Submarine body	m	diameter: 2.18, length 15.79
Speed	m/s	1.000
Reynolds number (SUBOFF Length)	- ($x10^6$)	1.611
Longitudinal Separation, RLong.	m	-13.43, -10.75, -8.06, -5.37, 0, 2.72, 5.37, 8.06, 10.75
Lateral Separation, RLat.	m	3.33, 3.71, 4.49

A summary of the test parameters, including the longitudinal and lateral separations, are given in Table 5.1. Since the SUBOFF dimensions were maintained throughout the test cases, the overall length of the SUBOFF model (1.44m) was used as the characteristic length scale for the Reynolds number and non-dimensionalisation of the hydrodynamic forces and moments experienced by the SUBOFF model.

5.3 Diameter Ratio 2.23:1 (CFD and EFD)

5.3.1 Varying Longitudinal Separations

Yawing Moment Interaction

Figure 5.1 gives the yaw moment action on the SUBOFF for different longitudinal positions relative to the larger body (Larger Submarine body) at a constant lateral separation ratio of 3.06. In general, it can be classified into 3 different trends, SUBOFF experiences bow yawing towards larger body, neutral, and stern yawing towards larger body. At the stern of the Larger Submarine body, the SUBOFF experiences the highest moment. When the SUBOFF is at midship of the Larger Submarine body, the yaw moment is near to zero before reaching a maximum value at the nose tip region of the Larger Submarine body. When the SUBOFF moves away from the nose tip of the Larger Submarine body, the yaw moment has less interaction. Therefore, from the graph presented, there is no moment action to the SUBOFF if it is positioned away from the bow of the Larger Submarine body.

Side Forces Interaction

Figure 5.2 shows the side drag force coefficients on the SUBOFF geometry to varying longitudinal separation ratio between the two bodies and Re, at the lateral separation ratio of 3.06. Due to the low pressure region between the vehicles, the side force acts to attract the two bodies together (in the negative direction) and increases as the SUBOFF approaches the front of the Larger Submarine body, with the maximum occurring as it just passes the nose of the larger vehicle. When the front half of the SUBOFF is no longer at the nose tip of the Larger Submarine body, the side force gradually reduces as the SUBOFF moves away from the larger body.

Drag Forces Interaction

Figure 5.3 shows the drag force coefficients on the SUBOFF geometry with respect to varying longitudinal separation ratio between the two bodies and Re, at the lateral separation ratio of 3.06. The drag coefficient of the SUBOFF is initially as it is approaching a relatively high pressure field aft of the larger vehicle. This decreases as the SUBOFF enters the low pressure region around the middle and aft area of the larger body. However, the drag again increases as it moves along the length of Larger Submarine body and enters the higher pressure region in the forward area of the latter.

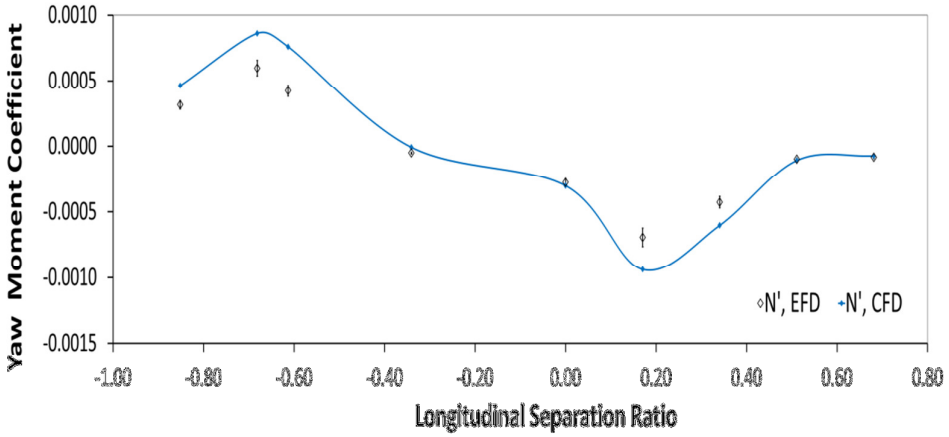

Figure 5.1: Yaw moment coefficient of SUBOFF vs. R_{Long}.

R_{Lat} = 3.06 at Re_{SUBOFF} = 1.62E+06 (without sting for the 2.23:1 diameter ratio) with 10% error bar representing the experimental uncertainty.

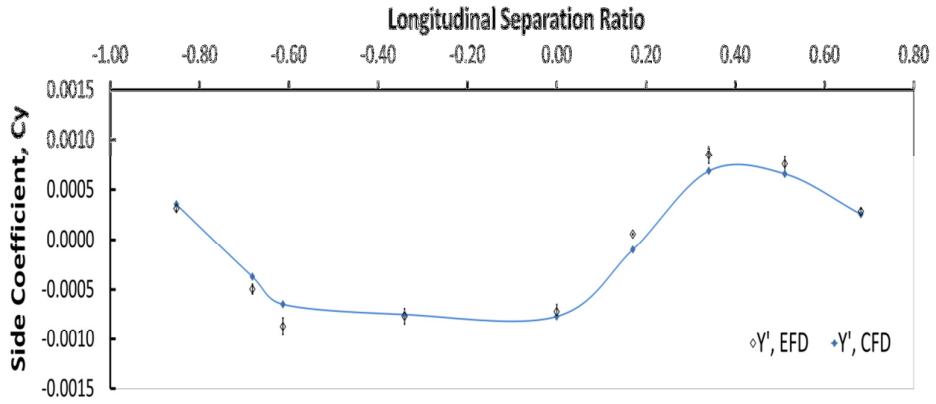

Figure 5.2: Side coefficient of SUBOFF vs R_{Long}.

R_{Lat} = 3.06 at Re_{SUBOFF} = 1.62E+06 (without sting for the 2.23:1 diameter ratio) with 10% error bar representing the experimental uncertainty.

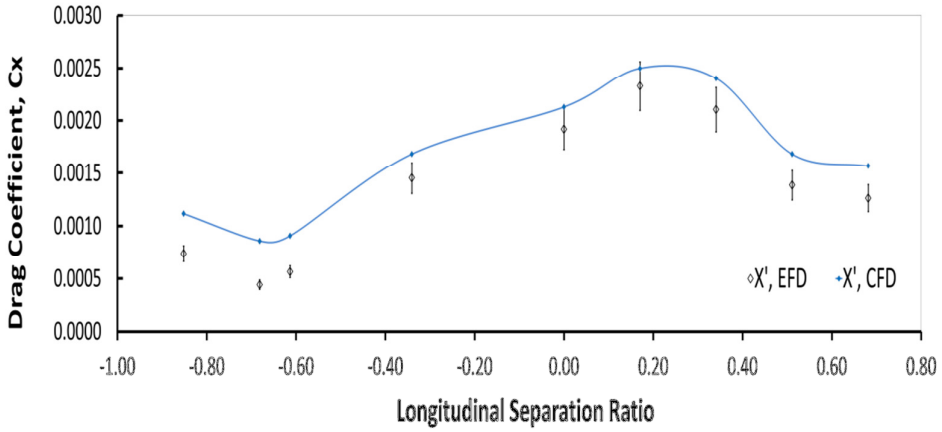

Figure 5.3: Drag coefficient of SUBOFF vs R_{Long}.

R_{Lat} = 3.06 at Re_{SUBOFF} = 1.62E+06 (without sting for the 2.23:1 diameter ratio) with 10% error bar representing the experimental uncertainty.

Flow Visualisation

Figure 5.4 shows a series of pressure contour plots around the two bodies for different longitudinal separations at a Re = 1.62E+06, with the lateral separation ratio fixed at 3.06. Figure 5.4 (a) shows the position where the SUBOFF approaching from the stern of Larger Submarine body. The high pressure field which is generated from the

nose tip of the SUBOFF reacts with the high pressure field aft of the larger body yawing the SUBOFF away from the latter.

As the SUBOFF enters the low pressure field developed by larger body, it begins to experience a moment that tends to yaw its nose towards the larger body. This moment increases as the SUBOFF moves along the body (refer to Figure 5.4 (b)), with strong interaction causing attraction at the nose tip and repulsion at the stern area. At this position, the chance of collision is high.

The yaw moment decreases as the SUBOFF progresses into the lower pressure region around the midsection of the larger body (refer to Figure 5.4 (c)). From the contour plot in Figure 5.4 (d), it is seen that the pressure field between the two bodies is negative when they are side by side. This together with the higher surrounding pressure results an attraction force between the two bodies. As the SUBOFF progresses into the forward section of the larger body (refer to Figure 5.4 (e)), the negative pressure field distributes evenly along the length of the larger body, significantly decreasing the yaw moment on the SUBOFF.

As the SUBOFF moves past the nose (refer to Figure 5.4 (f)) of the larger body, the positive pressure field acts on the forward section of the SUBOFF, causing the SUBOFF nose tip to yaw away from larger submarine body. Once the front half of the SUBOFF passes the nose tip of the Larger Submarine body, the negative pressure is seen to act only on the stern of the small body (refer to Figure 5.4 (g)), which will result in a moment that continues to yaw the bow away from the larger body as verified by the yaw moments plotted in Figure 5.5. As the SUBOFF moves ahead of the larger body (refer to Figures 5.4 (h) and (i)), the SUBOFF moves away from the pressure fields generated by the larger and the interaction gradually reduces to a negligible value.

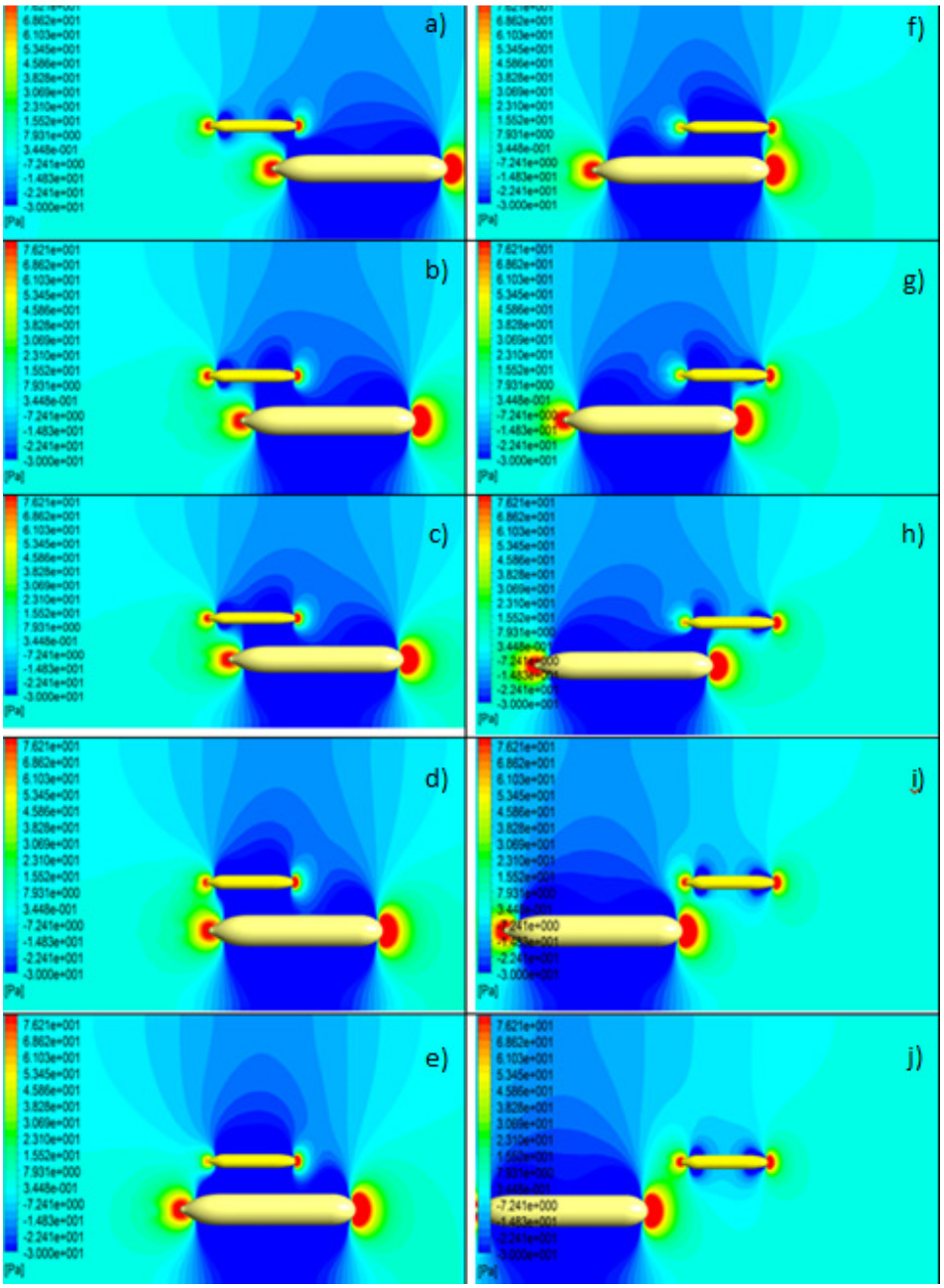

Figure 5.4: Pressure Visualisation of the two bodies as the smaller body (without sting) passes the larger body, with a Lateral Separation of 3.06 at Re = 1.62E+06. Longitudinal Separation at: a) -0.85; b)-0.68; c) -0.61; d) -0.51; e) -0.34; f) 0; g) 0.17; h) 0.34; i) 0.51, and j) 0.68.

Influence of the Sting Section

Figures 5.5, 5.6, and 5.7 respectively show the yaw moment, side force and drag force obtained through CFD simulations action on the SUBOFF as a function of longitudinal separation; with and without the sting used in the experimental setup. It is shown that the sting has negligible effect on the yawing moment and side force interaction behaviour on the SUBOFF. Only the drag interaction behaviour is affected by the sting. These findings correlate with Dress (1990), who found that when using a stern mounted sting arrangement, the overall drag of the body being tested will be reduced due to the increase in the apparent slenderness ratio which in turn reduces drag.

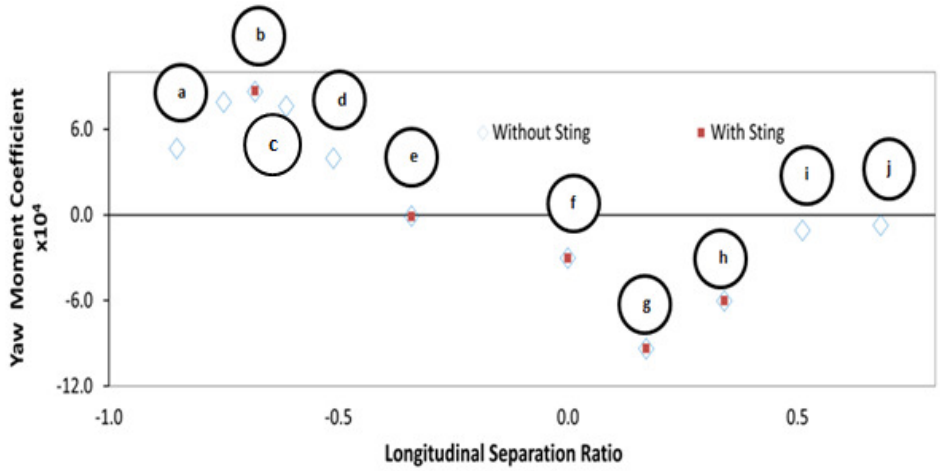

Figure 5.5: Yaw Moment Coefficient vs. Longitudinal Separation Ratio for Lateral Separation Ratio = 3.06 and Reynolds Number 1.62E+06. The numbered labels represent the positions of the visual plot in Figure 5.4.

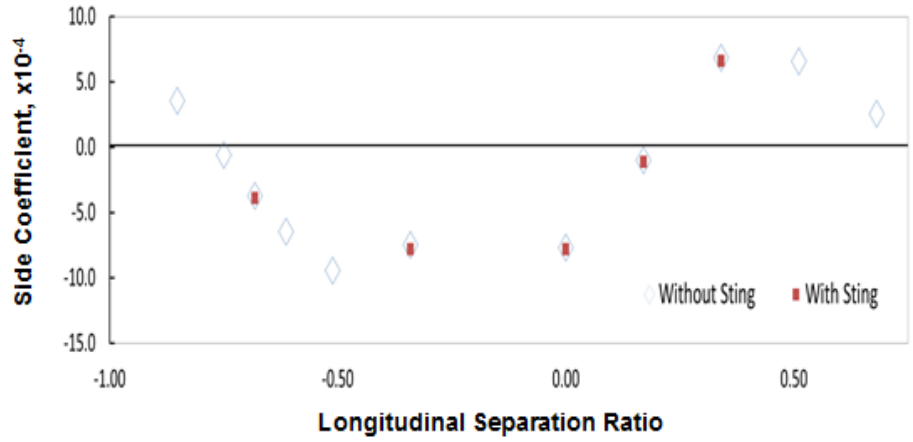

Figure 5.6: Side Force Coefficient vs. Longitudinal Separation Ratio for Lateral Separation Ratio = 3.06 and Reynolds Number 1.62E+06.

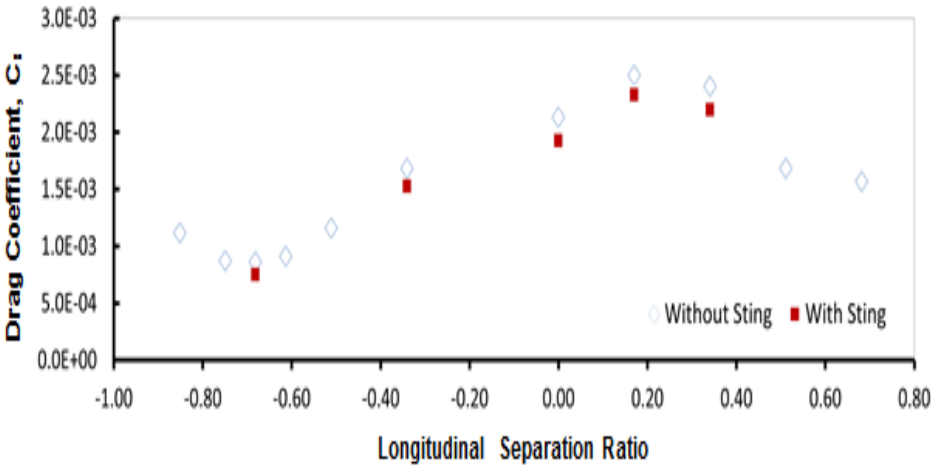

Figure 5.7: Drag Force Coefficient vs. Longitudinal Separation Ratio for Lateral Separation Ratio = 3.06 and Reynolds Number 1.62E+06.

The pressure plots in Figure 5.8, show the pressure contours as the SUBOFF moves along the larger body length. However, in this case, with the sting attachment at the stern of the SUBOFF. Comparing these with Figure 5.14 without the sting attachment, Figure 5.8 shows the effect of the sting on the SUBOFF pressure field at the aft end, which effectively reduces the drag, although the effects on the moment and side forces are much less prominent. The trends for all forces and moments for both cases are similar.

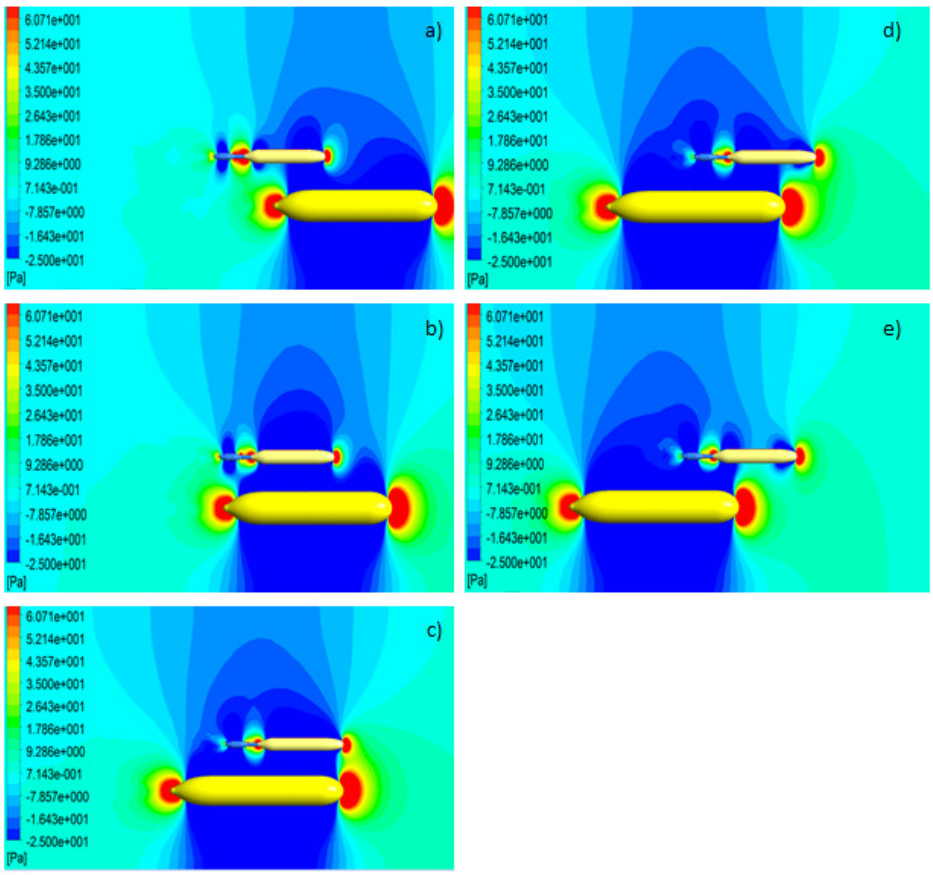

Figure 5.8: Pressure Visualisation of the with sting configuration for Lateral Separation 3.06 at Re = 1.62E+06 with varying Longitudinal Separation; a) -0.68; b) -0.34; c) 0; d) 0.17; and e) 0.34.

5.3.2 Varying Lateral Separation

Figures 5.9, 5.10, and 5.11 respectively show the yaw moment, side force, and drag force on the SUBOFF as a function of lateral separation ratio between the two bodies at different longitudinal separation ratios. As expected, they show that the magnitude of the yaw moment and side force decreases as the lateral separation increases. However, a general trend of the drag force was not observed. Figure 5.13 shows that the SUBOFF is still well within the pressure fields generated by the larger body, which could indicate that the larger lateral separation ratios need to be investigated in order to determine an observable trend for the drag force interaction on the SUBOFF as a function of lateral separation.

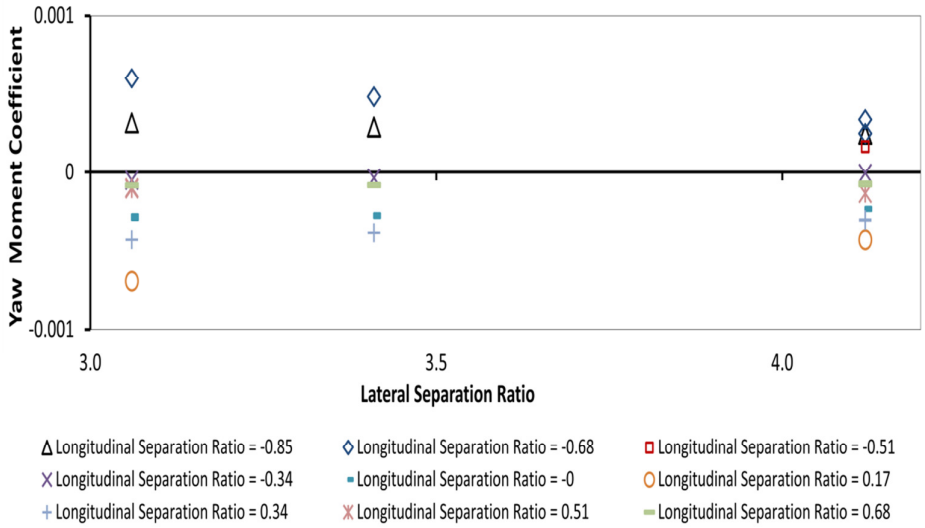

Figure 5.9: Yaw Moment Coefficient vs. Lateral Separation Ratio at Reynolds Number 1.62E+06.

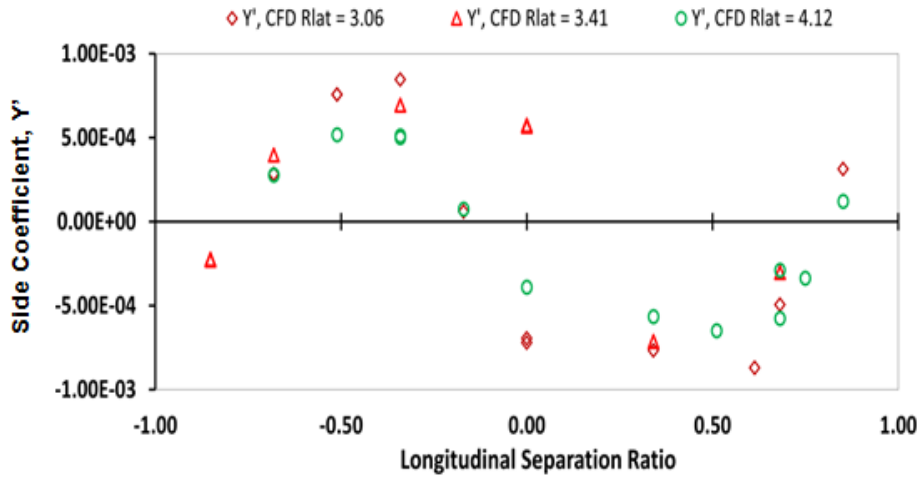

Figure 5.10: Side coefficient vs. $R_{Long} = 0$ at $Re_{SUBOFF} = 1.62E+06$ for varying lateral position.

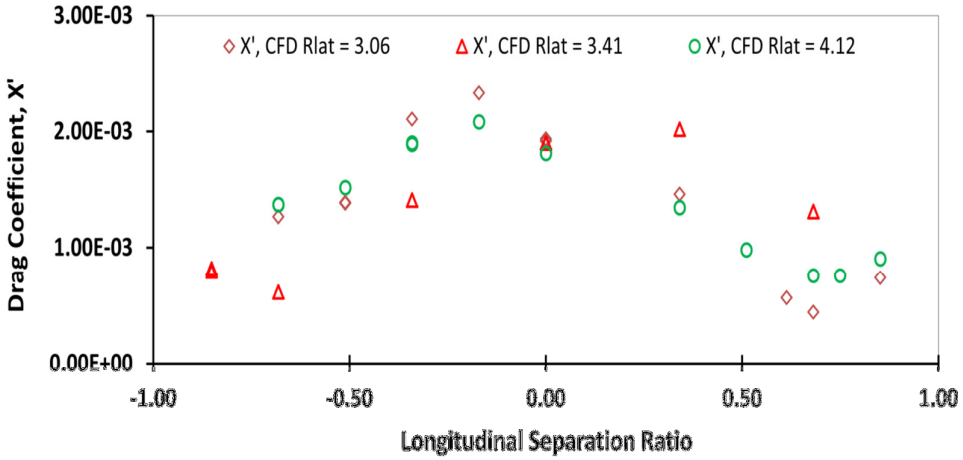

Figure 5.11: Drag coefficient vs. $R_{Long\ at}$ Re_{SUBOFF} = 1.62E+06 for varying lateral position.

Reynolds Dependency

Figures 5.12, 5.13 and 5.14 respectively show the yaw moment, side force, and drag force action on the SUBOFF as a function of lateral separation between the two bodies for different Reynolds numbers. The longitudinal separation ratio is fixed at 0. The moment and force interactions were found to decrease when the bodies were travelling at lower Reynolds numbers.

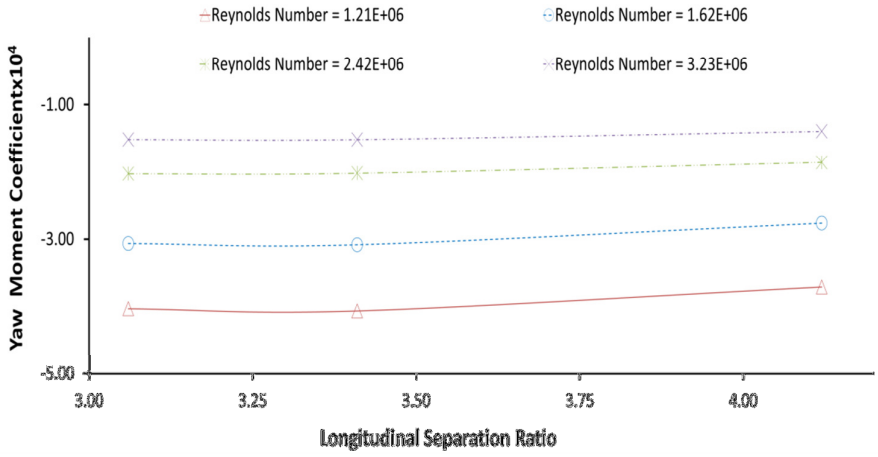

Figure 5.12: Yaw Moment Coefficient vs. Lateral Separation Ratio for Longitudinal Separation Ratio = 0.

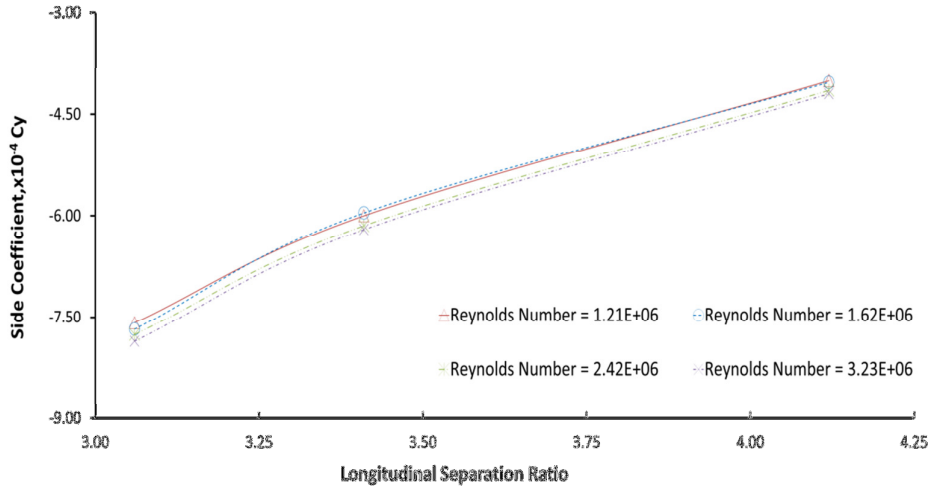

Figure 5.13: Side Coefficient vs. Lateral Separation Ratio for Longitudinal Separation Ratio = 0.

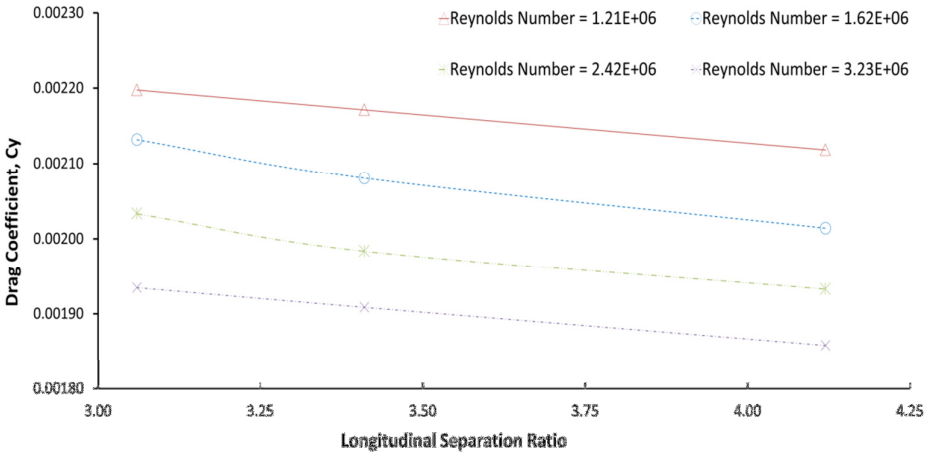

Figure 5.14: Drag Coefficient vs. Lateral Separation Ratio for Longitudinal Separation Ratio = 0.

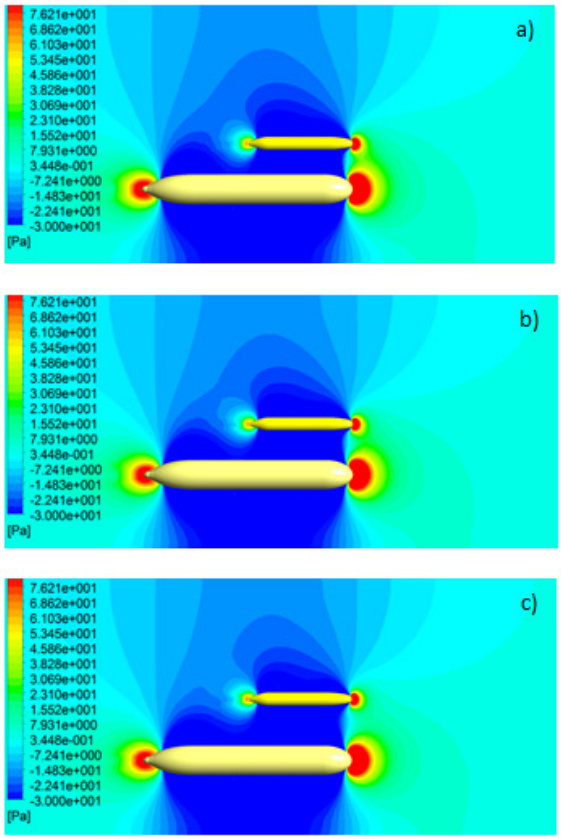

Figure 5.15: Pressure Visualisation for Longitudinal Separation Ratio 0, Re = 1.62E+06 with varying Lateral Separation; a) 3.06; b) 3.41; and c) 4.12.

5.4 Diameter Ratio 12:1 vs 2.23:1 (CFD)

Figures 5.16, 5.17, and 5.18 give the yaw moment, side force, and drag force respectively, on the SUBOFF as a function longitudinal separation ratio for the 12:1 and 2.23:1 diameter ratios between the vehicles at R_{Lat} = 3.06 and Re = 1.62E+06. With the 12:1 body, the observed drag force, side force and yaw moment were lower compared to the 2.23:1 body. This is explained by Figure 5.19, which shows the flow contours around the two bodies for the 12.1 diameter ratio. A comparison of the flow visualisation plots between Figure 5.19 (12.1 diameter ratio) and Figure 5.4 (2.23:1 diameter ratio) shows that the gradients in the pressure field experienced by the smaller (SUBOFF) body are lesser for the 12:1 diameter ratio, thus the experienced interaction forces and moments are lesser compared to the 2.23:1 diameter ratio.

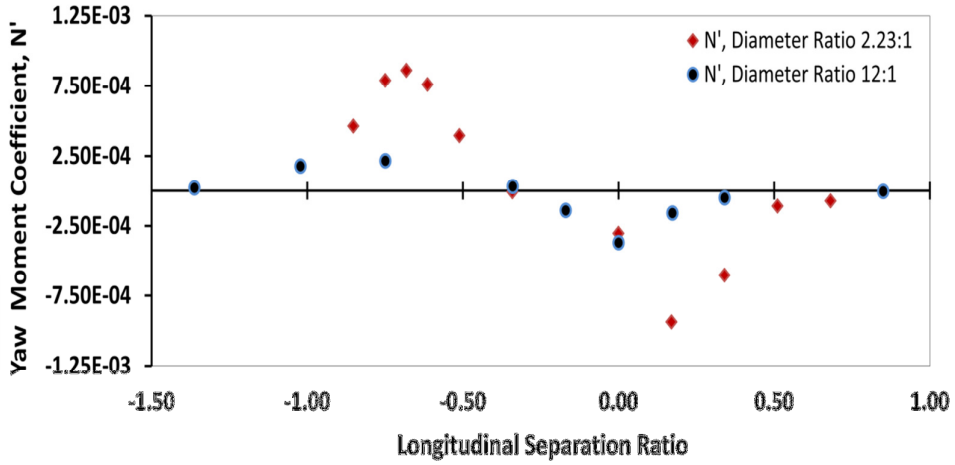

Figure 5.16: Yaw Moment coefficient vs. R_{Lat} = 3.06 at Re_{SUBOFF} = 1.62E+06 for different diameter ratio.

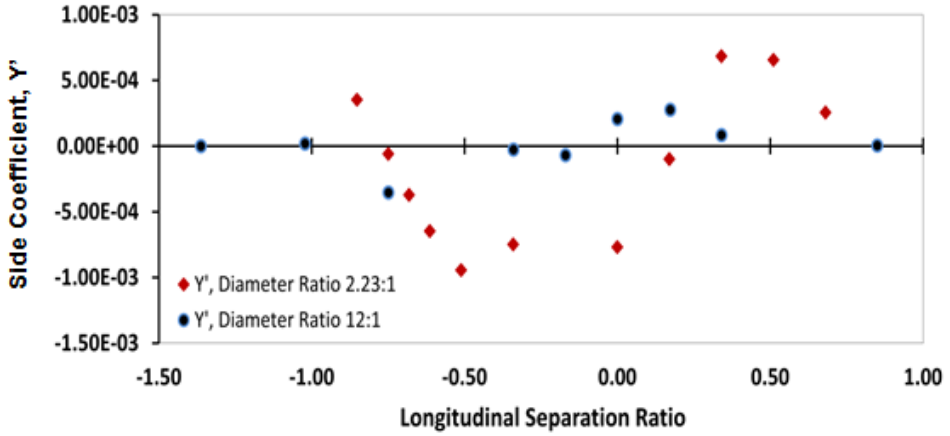

Figure 5.17: Side coefficient vs. R_{Lat} = 3.06 at Re_{SUBOFF} = 1.62E+06 for different diameter ratio.

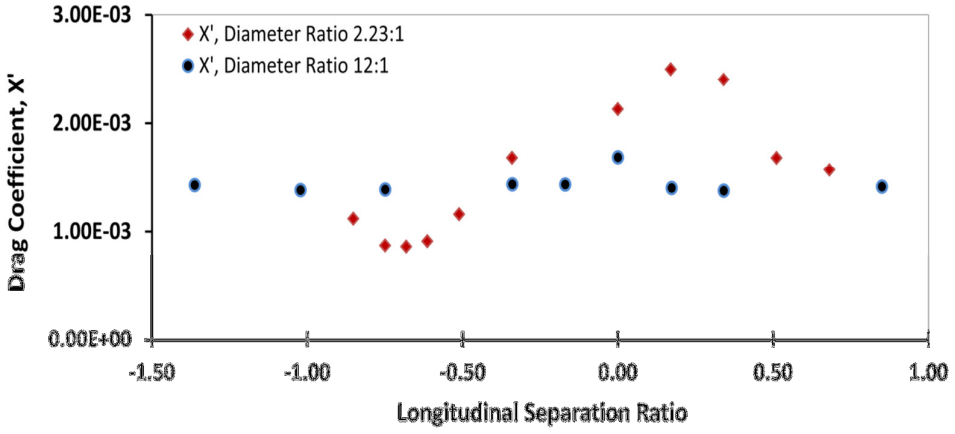

Figure 5.18: Drag coefficient vs. R_{Lat} = 3.06 at Re_{SUBOFF} = 1.62E+06 for different diameter ratio.

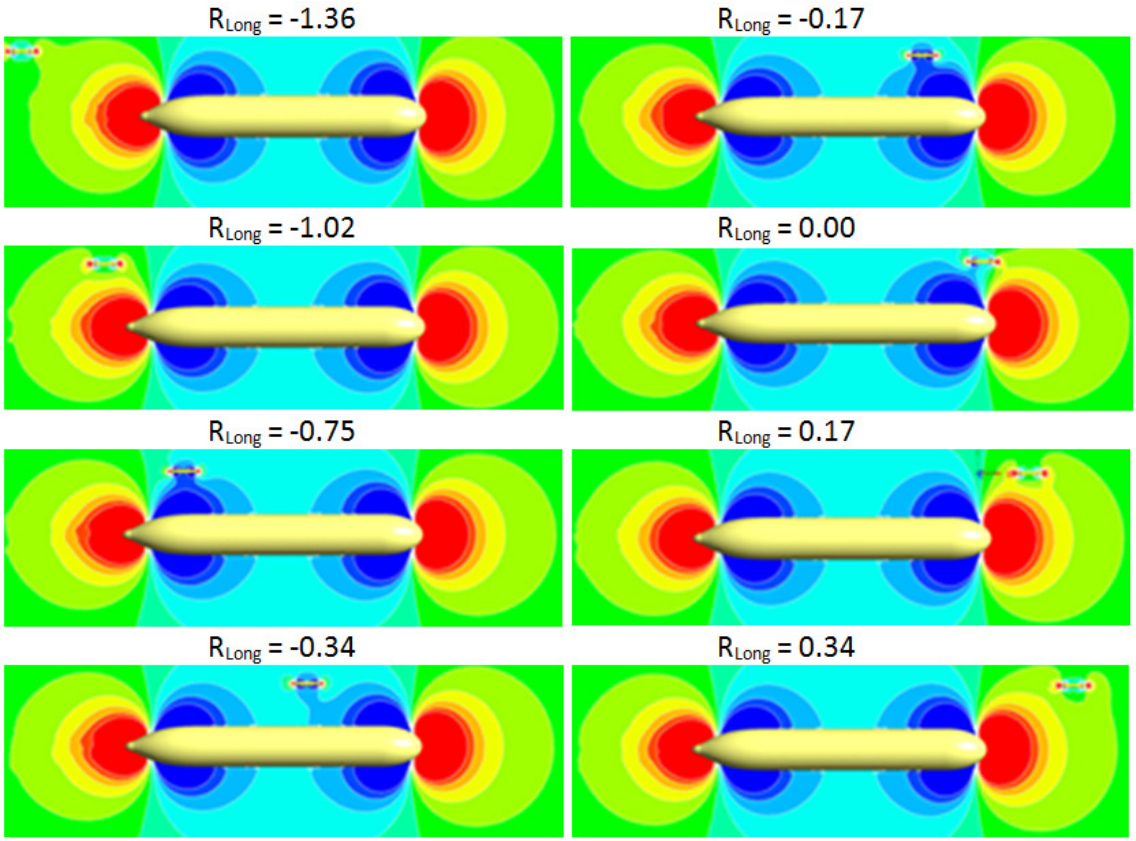

Figure 5.19: Pressure Visualisation for Lateral Separation 3.06 at Re = 1.62E+06 with varying Longitudinal Separation for the 12:1 diameter ratio vehicles. The red, blue and green colour spectrums denote high, low and neutral pressure regions respectively.

5.5 12:1 Diameter Ratio Results

The 12:1 diameter ratio represents the size differences between an AUV and a conventional submarine. Figures 5.20, 5.21, and 5.22 give the yaw moment, side force, and drag force on the SUBOFF as a function of longitudinal separation ratio for different later separation ratios at a diameter ratio of 12:1. The behaviour of the yaw moment, side force, and drag force interaction for the 12:1 diameter ratio are similar to the 2.23:1 diameter ratio (refer to Chapter 5.3). The moments yaw the SUBOFF bow towards the larger body at the stern region of the larger body and act to yaw the SUBOF bow away from the larger body at the fore region of the larger body. The side forces attract the SUBOFF as it passes the larger body. The magnitudes of the drag

force, side force, and yawing moment behaviour decrease as the lateral separation ratio increases.

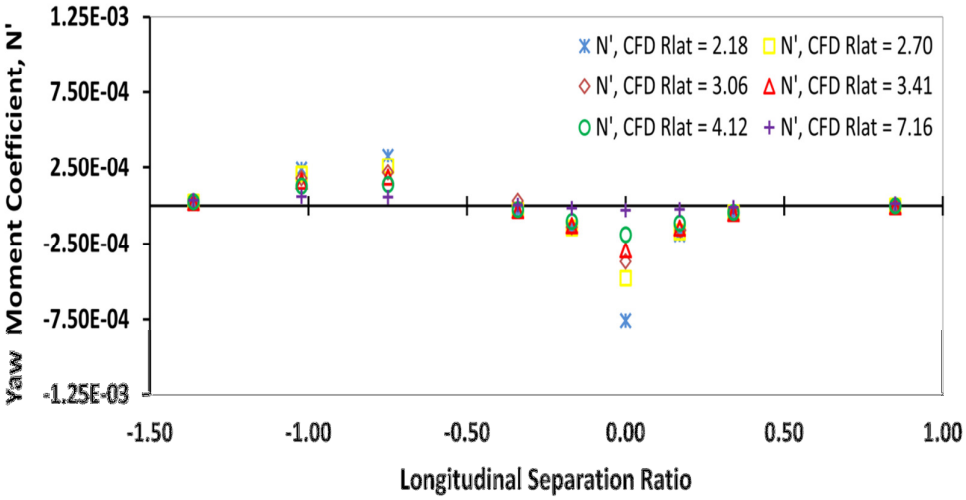

Figure 5.20: Yaw Moment coefficient vs. $R_{Long\ at}$ Re_{SUBOFF} = 1.62E+06 for varying lateral separation ratios at a vehicle diameter ration of 12:1.

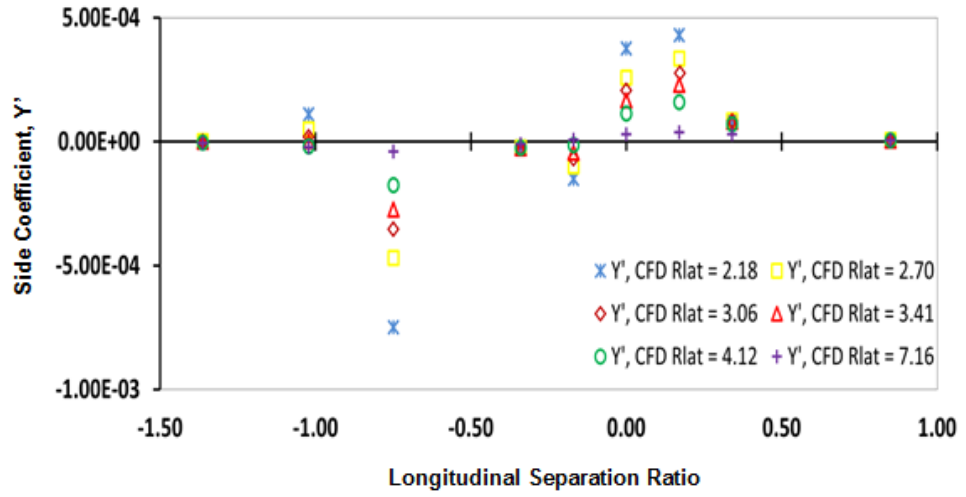

Figure 5.21: Side coefficient vs. $R_{Long\ at}$ Re_{SUBOFF} = 1.62E+06 for varying lateral separation ratios at a vehicle diameter ration of 12:1.

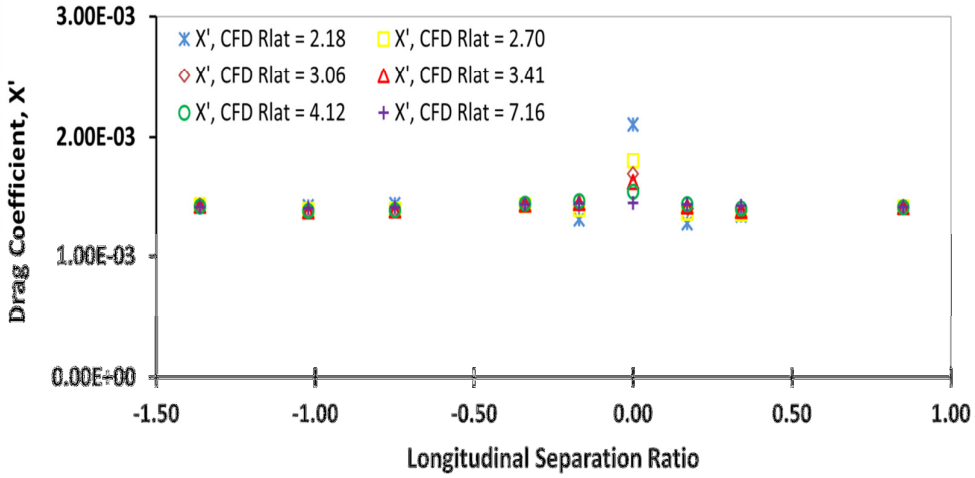

Figure 5.22: Drag coefficient vs. $R_{Long\ at}$ Re_{SUBOFF} = 1.62E+06 for varying lateral separation ratios at a vehicle diameter ration of 12:1.

Figure 5.23 shows the pressure contours around the SUBOFF and the larger body for different combinations of longitudinal separation ratios and lateral separation ratios. The observed effects of the pressure fields on the interaction behaviour of yawing moment, side force, and drag force as a function of longitudinal separation are similar to the 2.23:1 diameter ratio (refer to Chapter 5.3). Additional lateral separation ratios were investigated for the 12:1 diameter ratio compared to the 2.23:1 diameter ratio scenario. It was observed that at the lateral separation ratio of 4.12, the SUBOFF resides around the perimeter of the dominant pressure fields of the larger body. Above the lateral separation ratio of 4, the SUBOFF becomes less exposed to the pressure fields of the larger body and therefore less susceptible to the interaction effects, as observed in Figures 5.20, 5.21, and 5.22. However, the actual threshold separation ratio will depend on the forward speed of the larger body and its shape, as they will influence the pressure contours.

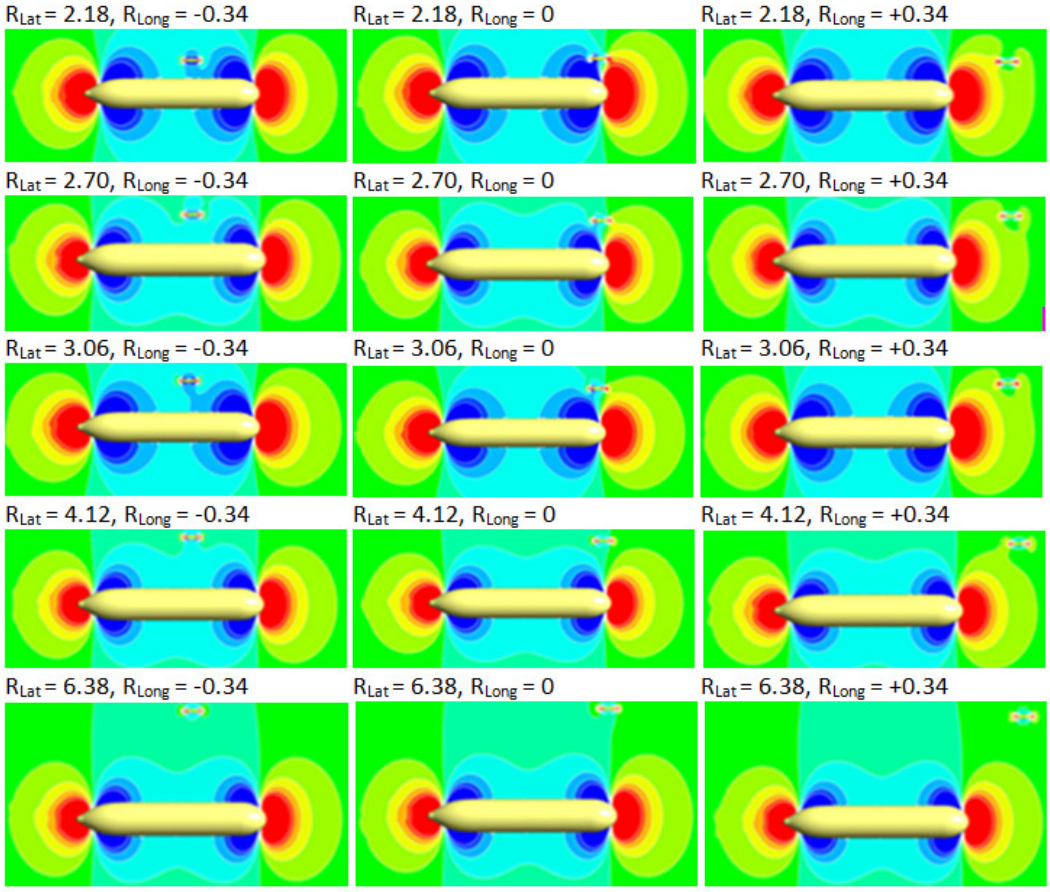

Figure 5.23: Pressure plot for Varying Lateral and Longitudinal Separation Ratio at Re = 1.62E+06 at a vehicle diameter ration of 12:1. The red, blue and green colour spectrums denote high, low and neutral pressure regions respectively.

5.6 Trajectory for minimal interaction forces and moment

Based on the observed trends in the results, an AUV approaching a larger body from either the bow or the stern is undesirable due to the large fluctuations in the hydrodynamic interaction behaviour (especially the side force and yaw moment) as the AUV moves along the length of the larger body. These fluctuations were however less noticeably when the AUV was around the midsection of the larger body that is close to R_{Long} of -0.25. The interaction effects were also found to be inversely proportionate to R_{Lat}. This suggests that a possible path for the AUV to approach or depart the larger body would be from the side of the midship of the latter in order to minimise the adverse effects of the interaction (refer to Figure 5.24). However, there

are other factors such as the wake fields generated from appendages, cross flow, propeller wake, and speed limits that will influence the direction of approach and departure.

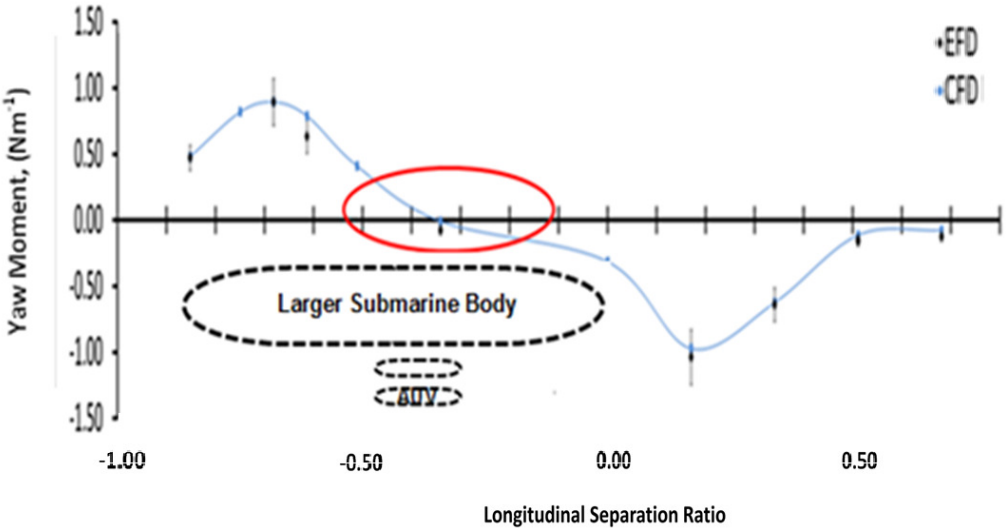

Figure 5.24: Proposed AUV approach from the side of Larger Submarine Body. EFD and CFD yaw moment results plotted for R_{Lat} = 3.06 and Re = 1.62E+06.

Chapter 6

Conclusions and Recommendations

6.1 Summary

This research was conducted to quantify the behaviour of the hydrodynamic interaction forces and moments (drag force, side force, and yawing moment) on an AUV operating in proximity to a larger underwater vehicle and the regions where the adverse interaction effects are minimal. Given that the AUV is smaller and more susceptible to the interaction effects, it is the focus of this thesis.

When an AUV is operating in close proximity to a larger vehicle, interaction with the complex flow patterns generated from the latter can potentially affect the ability of the AUV to maintain its trajectory, which may result in mission failure including collision between the vehicles. Therefore, it is important that underwater vehicle operators understand the interaction behaviour between two vehicles of different sizes in order to avoid the adverse interaction regions. In Chapter 2, the review of available literature showed that numerous studies had been carried out to investigate the interaction behaviour between surface ships. However, the understanding of the interaction effects between underwater vehicles remains limited and thus forms the motivation of this thesis.

This investigation utilised CFD and EFD techniques to obtain the forces and moments action on the AUV due to its interaction with the flow field of the larger vehicle. The EFD results from captive model tests in the AMC towing tank were used to validate CFD simulation models consisting of two vehicles having a diameter ratio of 2.23:1 at a number of different longitudinal and lateral separations, and speeds. Both vehicles were travelling at the same forward speed for the test cases. The validated CFD model was then extended to the case with a 12:1 vehicle diameter ratio, which is a closer representation of the size difference between an AUV operating in proximity to a typical conventional submarine.

The commercial CFD package ANSYS CFX using RANS-based simulations with the Shear Stress Transport (SST) turbulence model was able to accurately predict the interaction forces and moments action on the AUV. The validation at the vehicle diameter ratio of 2.23:1 using measurements from the experimental trials at the AMC Towing Tank required the influence of the mounting sting and the physical towing tank boundary conditions.

6.2 Conclusions

The modelling and verification process showed that the RANS based SST simulation model was able to adequately simulate the interaction effects of the two bodies. The CFD was validated against experimental data from the AMC towing tank, which required the modelling of the experimental setup. The effect of the mounting sting was clearly modelled, showing that it affected the drag force but had minimum effects on the sway force and yaw moment.

The interaction forces and moments on the AUV were found to change depending on the AUV's longitudinal position relative to the larger vehicle. The surge and sway forces and the yaw moment changed as the smaller vehicle approached the larger vehicle from the sterns, gradually moving along its length, and finally overtaking the latter. The summaries of the finding as below:

- The surge force is minimum when the small vehicle's midship section is adjacent to the larger vehicle stern and maximum in the region where the same section of the small vehicle is adjacent to the bow of the larger vehicle.

- When the midship section of the smaller and larger vehicles is adjacent, the yaw moment is small. However, the yaw moment is bowed towards the larger vehicle for the tested cases when the midship section of the smaller vehicle is aft of the larger vehicle. The yaw moment bows away from the larger vehicle for cases where the smaller vehicle's midship section is forward of the larger vehicle.

- The sway force is towards the larger vehicle when the midship sections of both vehicles are adjacent and when the smaller vehicle's midship section is between the bow and stern of the larger vehicle. The sway force is away from the larger vehicle when the smaller vehicle midships is aft of the larger vehicle stern and forward of the larger vehicle bow due to the higher pressure generated in those regions.

The variation of interaction forces and moments with relative longitudinal position between the vehicles will influence the operations of the smaller vehicle and presents the risk of collision with the larger body, particularly in cases where there is a relatively large yaw moment and sway force. Hence, the results suggest that using an approach and departure trajectory within the region of the midship section of the larger body, it will minimise the combined sway force and yaw moment effects. This will in turn reduce the interaction affects and the possibility of collision and mission failure.

An increase in lateral separation was found to decrease the magnitude of the interaction forces and moments action on the AUV throughout the range of longitudinal separations investigated. An increase in lateral separation significantly reduces the interaction effects, although the actual separation may depend on other factors such as the vehicle shape and configuration, and mission requirements.

The form of the interaction forces and moments as a function of longitudinal and lateral separations were found to be similar between the diameter ratio configurations, i.e. 2.23:1 and 12:1. However, the magnitude of interaction forces and moments were much smaller for the 12:1 diameter ratio compared to the 2.23:1 diameter ratio due to the relatively bigger difference in the pressure field size of the two vehicles. In addition, the interactions were found to decrease when the bodies were travelling at lower Reynolds numbers.

The work provides data on the effects of the relative diameter ratios, longitudinal and lateral separation, and forward speeds. However, when designing the vehicles and planning missions, it is also important to consider the affects from:

- shape and appendages that will affect the pressure and wake fields, as well and the reaction of the smaller AUV;
- mission requirements and environmental influences that can result in affects cross flow and out of plane forces; and
- propeller.

It is important that designers and operators are aware of these effects to ensure that the vehicle control system is able to adapt to compensate for these effects and is able to manoeuvre safely around these hazards.

6.3 Further Work

The work presented in this thesis forms a foundation for future work in the investigation, design, and operation of AUVs in close proximity to larger underwater vehicles. These include:

- further longitudinal and lateral separations between the two vehicles are examined in order to determine the spatial extent of the interaction forces and moments induced by the larger vehicle;

- extension of investigation to a greater range of diameter ratios to identify its effect on the hydrodynamic interaction behaviour;

- considering the effects of relative speeds between vehicles and transient flow effects on the interaction behaviour;

- the effects of appendages such as control surfaces and sails on the interaction between the vehicles, which includes the effect on the pressure and wake fields generated and the forces and moments created due to the appendages; and

- the effects of the propellers of the two bodies on the interaction and the trajectory of the AUV.

The safety and effectiveness of AUVs operating in close proximity of larger underwater vehicles will require a number of aspects to be considered, including the shape and form of the vehicles, the relative speeds, environmental influences, appendages, and propulsion effects. The work carried out in this project provides one part of the solution, identifying regions of high and low which are danger to the AUV and quantifying the affects due to changes in location, speed, and size. It provides the designer and operators with information on safety and characteristics that will assist in working towards safer operations.

References

Ackerman, S. (2008). Prediction of Suboff Hydrodynamics using ANSYS CFX Software. Launceston: National Centre of Maritime Engineering and Hydrodynamics.

Anderson. (1995). Computational Fluid Dynamics: The Basics with Application. New York: McGraw-Hill.

An, E., and Smith, M.S. (1998). An Experimental Self-Motion Study of the Ocean Explorer AUV in Controlled Sea States. IEEE Journal of Oceanic Engineering, 23(3), 274-284.

Anderson, B. J., Campanella. G. F., Walker, G. J., (1995). Development of a Horizontal Planar Motion Mechanism for Determining Hydrodynamic Characteristics of Underwater Vehicles, Twelfth Australian Fluid Dynamics Conference, University of Sydney

ANSYS CFX. (2011). ANSYS CFX User Manual.

ANSYS-ICEM CFD. (2011). ANSYS-ICEM CFD User Manual.

Apsley, D.(2004), Turbulence Modelling in CFD

Asakawa, K., Kojuma, J., Kato, Y., Matsumoto, S., Kato, N., Asai, T., and Iso, T. (2002). Design Concept and Experimental Results of the Autonomous Underwater Vehicle AQUA EXPLORER 2 for the Inspection of Underwater Cables.Advanced Robotics, 16(1), 27-42.

ATI, (2010). Multi-Axis Force/Torque Sensor Catalogue, ATI Industrial Automation, Apex.

Atkins, D. (2006). The Experimental Testing of the Mullaya. Tasmania: Australian Maritime College

Blasius, H. (1908). Grenzschichten in Flüssigkeiten mit kleiner Reibung (Boundary layers in fluids with little friction), Zeitschrift für Mathematik und Physik

Brady, L. (2007). Hydrodynamics of Autonomous Underwater Vehicle's through CFD Investigations, Australian Maritime College, Launceston, Tasmania.

Bull, P. (1996). Validation of CFD Predictions of Nominal Wake for the Suboff Fully Appended Geometry. 21st Symposium on Naval Hydrodynamics, National Academic Press.

Burcher, R., & Rydill, L. (1998). Concepts in Submarine Design, Cambridge University Press.

Chase, M. S. (1911). Results of Experimental Tank Tests on Models of Submarines, RINA Transactions, London

Chng, T., Widjaja, R., Kitsios, V., and Ooi, A. (2007). RANS Turbulence Model Optimisation based on Surrogate Management Network. 16th Australian Fluid Mechanics Conference. Brisbane.

Dawson. E., Anderson. B., Van Steel. S., Renilson. M., Ranmuthugala. D., (2010). An Experimental Investigation into the Near Surface Effects of Near-Surface Operation on the Wave-Making Resistance of SSK Type Submarines, MAST 2010

DeMoss, J. A. (2007). Drag Measurements on an Ellipsoidal Body. Blacksburg: Virginia Polytechnic Institute.

Douglas, J.F., Gasiorek, J.M, and Swaffield, J.A (2000), Fluid Mechanics, 4th Edition, Prentice Hall.

Dress, D. (1990). Drag Measurements on a Modified Prolate Spheroid Using a Magnetic Suspension Balance System. Journal of Aircraft, 27(N6), 523-528.

Evans, J., and Nahon, M. (2004). Dynamics modelling and performance evaluation of an autonomous underwater vehicle. Ocean Engineering, 31, 1835-1858.

Feldman, J. (1987) Straight-line and Rotating Arm Captive-Model Experiments to Investigate the Stability and Control Characteristics of Submarines and Other Submerged Vehicles. Bethesda: David W. Taylor Ship Research and Development Center.

Fell, B. (2009). Structured Mesh Optimisation and CFD Simulation of the Fully Appended DARPA Suboff Model. Launceston: National Centre of Maritime Engineering and Hydrodynamics.

Fitzgerald, B. (2009) Prediction of Hydrodynamic and Manoeuvring Characteristics of the AUV Mullaya through CFD and Experimental Work. Tasmania: Australian Maritime College

Gertler, M. (1950). Resistance Experiments on a Systematic Series of Streamlined Bodies of Revolution, the David W. Taylor Model Basin, Washington D.C.

Gorski, J. (2002). Present State of Numerical Ship Hydrodynamics and Validation Experiments. Journal of Offshore Mechanics and Arctic Engineering, 124(2), 74-80. Bethesda, Maryland: David Taylor Research Centre.

Groves, N. C., Huang, T. T., Chang, M. S. (1989). Geometric Characteristics of DARPA SUBOFF Models, David Taylor Research Centre, Bethesda.

Hama, F. R. (1957). An Effective Tripping Device, Journal for Aeronautical Sciences. Hoerner, S. F. (1958). Fluid-Dynamic Drag. New Jersey

Husaini, M., Samad, Z., Rizal, M. (2009) CFD Simulation of Cooperative AUV Motion. P.Pinang. University Sains Malaysia.

ITTC. (1948). The Use of Turbulence Producing Devices in Model Experiments, International Towing Tank Conference. London

ITTC. (1999). ITTC- Recommended Procedures and Guidelines: Testing and Extrapolation Methods, General Uncertainty Analysis in EFD Uncertainty Assessment Methodology. (7.5-0201-02) International Towing Tank Conference.

ITTC. (2002). ITTC- Recommended Procedures and Guidelines: Model Manufacture Ship Models. (7.5-01 -01-01) International Towing Tank Conference.

ITTC. (2002b). ITTC- Recommended Procedures and Guidelines: Testing and Extrapolation Methods: Resistance- Uncertainty Analysis, Example for Resistance Tests. (7.5-02 02-04) International Towing Tank Conference.

Jagadeesh, P., Murail, K., and Idichandy, V.G. (2008). Experimental Investigation of Hydrodynamic Force Coefficients over AUV Hull Form. Ocean Engineering, 36(2009), 113-118.

Joubert, P. (2004). Some Aspects of Submarine Design: Part 1 Hydrodynamics. Melbourne: DSTO Platforms Science Authority.

Kelvin, Lord. (1887), Ship Waves, Transactions IME, London 82

Landry, P. (1997). Air-to-Air Refuelling Aerodynamic Interaction. British Columbia: University of British Columbia.

Leong, Z, Q. (2011). CFD and Experimental Investigation into the Hydrodynamic Coefficients of AUV Mullaya. Launceston: National Centre of Maritime Engineering and Hydrodynamics.

Lewandowski E. M. (1994). The Effects of Aspect Ratio, Section Shape, and Reynolds Number on the Lift and Drag of a Series of Model Control Surfaces, Stevenson Institute of Technology, Hoboken, New Jersey

Lewis, E. V. (1988). Principles of Naval Architecture - Resistance, Propulsion and Vibration (Vol. II), SNAME, Jersey City

Liu, H. L., Huang, T. T. (1998). Summary of DARPA SUBOFF Experimental Data, David Taylor Research Centre, Bethesda.

Lou,H., Buam, J., & Lohner, R. (2000). The Computation of CompressibleTurbulent Flows on Unstructured Grids. USA: George Mason University.

Malalasekera, K., & Versteeg, P. (2007). Computational Fluid Dynamics: The Finite Volume Method. Prentice Hall.

Mohammadi, B. (1997). A new Optimal Shape Design Procedure for Inviscid and Viscous Turbulent Flows. International Journal for Numerical Methods in Fluids, Vol 25, 183-203.

Moinuddin, K., Joubert, P., & Chong, S. (2004). Skin Friction CFD Calculation for Complex Flow: Turbulent Flow along an External Corner. Victoria University of Technology, Melbourne.

Prandtl, L. (1921). Ergebnisse der Aerodynamischen Versuchsanstalt zu Goettingen. Abhandlungen aus dem Aerodynamischen Institut, Aachen

Prestero, T., 2001. Verification of a six-degree of freedom simulation model for the Remus autonomous underwater vehicle. Master Thesis, MIT.

Pride, M. (2007). CFD Modelling and Validation of the AUV Mullaya. Tasmania: Australian Maritime College.

Rajamani, G. (2006). CFD Analysis of Air Flow Interactions in Vehicle Platoons. Melbourne: RMIT University.

Rawson. K. J., Tupper. E. C., (2001). Basic Ship Theory, Butterworth-Heinemann, Oxford

Roddy, R. F. (1990). Investigation of the Stability and Control Characteristics of Several Configurations of the DARPA SUBOFF Model From Captive Model Experiments, David Taylor Research Centre, Bethesda.

Schlichting, H. and Gersten, K., *Boundary Layer Theory*, 8th Ed., Springer, Berlin, 2000.

Todd, F. H. (1948). Subject 4 - Turbulence stimulation in model test. Fifth International Conference of Ship Tank Superintendents, (pp. 98-135). London.

Toxopeus, S. (2008). Viscous-flow calculation for bare hull DARPA SUBOFF submarine at incidence. International Shipbuilding Progress 55(2008) 227-251.

Tu, J., Yeoh, G., & Lui, C. (2008). Computational Fluid Dynamics: A Practical Approach.Burlington: Butterworth-Heinermann

Sarkar, T, Sayer, P.G, Fraser, S.M. (1997), A Study of Autonomoue Underwater Vehicle Hull Forms Using Computational Fluid Dynamics, International Journal for Numerical Methods in Fluid, Vol. 25, 1301-1313

Schubauer, G. B., Skramstad, H. K. (1943). Laminar Boundary Layer Oscillations and Stability of Laminar Flow, National Bureau of Standards Research Paper 1772

Van Steel, S. (2010). Investigation into the Effect of Wave Making on a Submarine Approaching the Free Surface, Australian Maritime College, Launceston.

Weihs, D., Ringel, M., & Victor, M. (2006). Aerodynamic Interactions Between Adjacent Slender Bodies, AIAA Journal, Vol. 44(3), 481-484.

White, F. M. (2011). Fluid Mechanics (Seventh ed.), McGraw-Hill, New York

Widjaja, R., Anderson, B., Chen, L., & Ooi, A. (2007). RANS Simulations of Suboff Bare Hull Model. Melbourne: Maritime Platforms Division Defence Science and Technology Organisation.

Wilcox, D.C. (1994). Turbulence Modelling for CFD, DCW Industries, California, USA

Zhang, H., Xu, Y., and Cai, H. (2010) Using CFD Software to Calculate Hydrodynamic Coefficients. Journal of Marine Science and Application, 9, 149-155.

APPENDIX A

Near Wall Modelling Theory

The modelling of flow near the wall is extremely important in fluid flow analysis. This Appendix outlines the equations used by ANSYS-CFX to define each sub-division of the boundary layer.

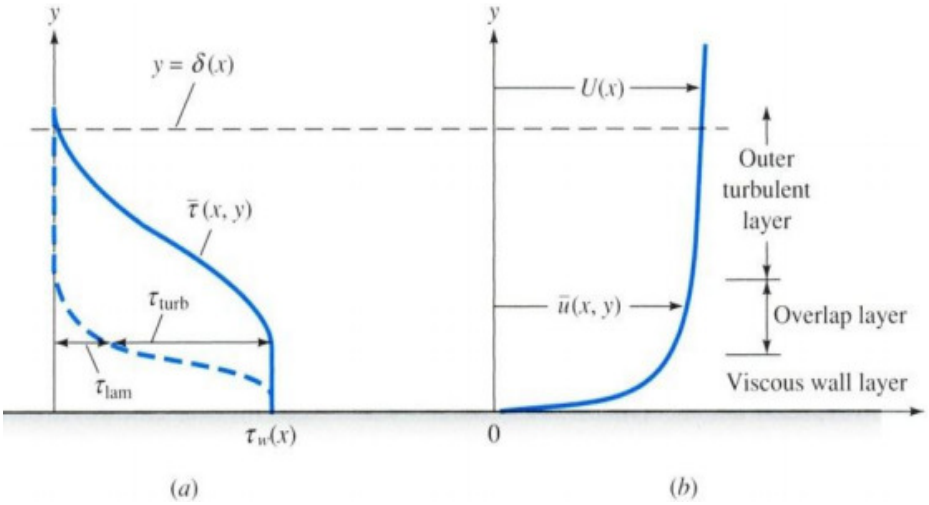

Figure A1: Velocity and shear distribution near a solid boundary (a) shear (b) velocity

In the viscous wall layer, the flow is not yet influenced by the free stream and is dominated by viscous stresses. Therefore, the mean flow velocity is proportional to the distance y from the wall, the fluid density ρ, the viscosity of the fluid μ, and the wall shear stress τ_w (Malalasekera et al., 2007). Through dimensional analysis it is shown that,

$$u^+ = \frac{u}{u_t} = f\left(\frac{\rho u_t y}{\mu}\right) = f(y^+)$$

This equation is called the law of the wall and introduces two important non-dimensional terms, u^+ and y^+, where u_t is the frictional velocity and is defined as;

$$u_t = \left(\frac{T_w}{\rho}\right)^{1/2}$$

The frictional velocity in the outer layer is independent of viscosity, but is dependent on other properties as shown below;

$$(U - u)_{outer} = g(\delta, \tau_w \rho y)$$

And by dimensional analysis

$$\frac{U-u}{u_t} = g\left(\frac{y}{\delta}\right)$$

This equation is known as the velocity defect law which along with the law of the wall are used to model the flow in each layer.

Viscous Wall Layer

The viscous sub-layer is in practice extremely thin ($y^+ < 5$) and it may be assumed that the sheer stress remains approximately constant and equal to the wall shear stress τ_w throughout the layer (Malalasekera et al., 2007). Therefore;

$$\tau(y) = \mu\frac{\partial U}{\partial y} \cong \tau_w$$

Upon integration with boundary conditions and non-dimensionalising the equations it is seen that;

$$u^+ = y^+$$

This shows that there is a linear relation between the velocity u and the distance from the wall y. This is why the viscous wall layer is also known as the linear sub layer.

Overlap Layer

In this region both the viscous and turbulent forces are present. Malalasekera et al. (2007) explains that the shear stresses (τ) vary slowly with the distance from the wall. And using the mixing length equations it is possible to derive an equation relating y^+ and u^+.

$$u^+ = \frac{1}{k}ln(y^+) + B$$

This equation is known as the log law and for this reason the overlap layer is often referred to as the log law layer (Malalasekera et al., 2007).

Outer Turbulent Layer

For larger values of y (y/δ> 0.2) the velocity defect law is applicable. However this equation needs modification so that at the overlap region the velocity defect law and the log law are equal. Tennekes et al. (1972) show that a matched overlap is obtained by assuming the following logarithmic form:

$$\frac{U-u}{u_t} = -\frac{1}{k} ln\left(\frac{y}{\partial}\right) + A$$

APPENDIX B

Uncertainty Analysis

The uncertainty analysis for the physical model scale experiment results was conducted as per ITTC Procedure 7.5-02-02-03 (ITTC, 2002). This procedure accounts for the uncertainty in the parameters associated with the model geometry and instrumentation for the measurement of carriage speed, towing tank water temperature and density and the force measurement. A summary of the parameters included in the uncertainty analysis and the associated accuracy and bias limits is shown in Tables B1a and B1b. Other parameters required to perform the analysis are provided in Table B2. The quantification of the uncertainty requires repeat tests to be conducted for a selected case. The surge force results from the repeat tests for the present study are shown in Table B3. The partial derivatives to be evaluated in the uncertainty computations and their values for a test speed of 1.5m/s are provided in Table B4. The above data is used to compute the precision limit (95% confidence) and the total uncertainty of the surge force coefficient (95% confidence) (refer to Tables B5 and B6, respectively). The uncertainty analysis for sway force and yaw moment were calculated using a similar process.

Table B1a: Accuracy and bias limits

Measurement Accuracy and Bias			
Definition	Symbol	Accuracy	Bias Limit
Model Geometry			
Model Length	B_L	1.00E-03	2.00E-03
Carriage Speed			
Pulse Count	B_C	-	2.36E+00
Optical Encoder	B_{C1}	1.00E+00	1.00E+00
AD Converter 1	B_{C2}	1.50E+00	1.50E+00
AD Converter 2	B_{C3}	1.50E+00	1.50E+00
Voltage to Frequency Converter	B_{C4}	2.50E-01	2.50E-01
Wheel diameter	B_D	1.00E-03	1.00E-03
Time Base	$B_{\Delta t}$	1.03E-05	1.03E-05
Velocity	B_U	-	5.65E-03
Tank Water Temperature and Density			
Thermometer reading	B_T	5.00E-01	5.00E-01
Temp-density relationship	B_{P1}	9.20E-02	9.20E-02
Convert temp to density	B_{P2}	7.00E-02	7.00E-02
ITTC density assumption	B_{P3}	3.00E+00	3.00E+00
Density	B_P	-	3.00E+00

Table B1b: Accuracy and bias limits

Resistance Measurement			
Accuracy of Calibration Weights	B_{RX1}	5.00E-05	5.66E-05
Mass/Voltage relationship SEE	B_{RX2}	3.07E-02	3.07E-02
Load cell misalignment	B_{RX3}	2.50E-01	1.08E-05
AD Converter	B_{RX4}	0.00E+00	0.00E+00
Inclination of model due to speed	B_{RX5}	2.50E-01	1.08E-05
Resistance	B_{RX}	-	3.07E-02
Coefficient of Total Resistance	B_{CT}	-	4.31E-05

Table B2: Model and Condition Parameters

Parameters			
Length overall	L_{OA}	1.556	m
Gravity	g	9.81	m/s^2
Density - reference	P_{ref}	1000	kg/m^3
Water Temp - test	t	18	deg
Water Density - test	ρ	997	kg/m^3
Pulse count	c	600	-
Time based circuitry	Δt	0.1	s
Carriage wheel diameter	D_W	0.555	m

Table B3: Surge force results from the repeat tests for the test speed of 1.5m/s

Multiple Run Data Set					
Run No.	U (m/s)	Rx (g)	Rx (N)	Cx	$(Cx-Cx_{mean})^2$
1	1.5	116.000	1.138	0.00042	4.20E-12
2	1.5	116.820	1.146	0.00042	2.51E-11
3	1.5	112.960	1.108	0.00041	7.98E-11
4	1.5	115.950	1.137	0.00042	3.49E-12
Mean	1.5	115.433	1.132	0.00042	
Standard deviation					6.13E-06

Table B4: Partial derivatives to be evaluated in the uncertainty computations and their values for the test speed of 1.5m/s

Partial Derivatives		
Partial Derivative - Resistance Coefficient	Symbol	Value
$\frac{R_x}{0.5\rho U^2}\left(-\frac{1}{L^2}\right)$	$\frac{\partial C_T}{\partial L}$	-4.17E-04
$\frac{R_x}{0.5\rho L^2}\left(-\frac{2}{U^3}\right)$	$\frac{\partial C_T}{\partial U}$	-5.56E-04
$\frac{R_x}{0.5L^2U^2}\left(-\frac{1}{\rho^2}\right)$	$\frac{\partial C_T}{\partial \rho}$	-4.18E-07
$\frac{1}{0.5\rho L^2U^2}$	$\frac{\partial C_T}{\partial R_X}$	3.68E-04
Partial Derivative - Velocity		
$\frac{\pi D}{8000\Delta t}$	$\frac{\partial U}{\partial c}$	7.11E-04
$\frac{c\pi}{8000\Delta t}$	$\frac{\partial U}{\partial D_W}$	2.36E
$\frac{c\pi D}{8000}\left(-\frac{1}{\Delta t^2}\right)$	$\frac{\partial U}{\partial \Delta t}$	-4.26E
Partial Derivative - Density		
$\lvert 0.0552 - 0.0154t^2 + 0.000120t^2 \rvert$	$\left\lvert\frac{\partial \rho}{\partial t}\right\rvert$	0.183

Table B5: Precision limit of the surge force coefficient

Precision Limit (95% Confidence)		
Precision Limit	Symbol	Value
Multiple Sample Precision Limit	P_{CTM}	6.13E-06
Single Sample Precision Limit	P_{CTS}	1.23E-05

Table B6: Uncertainty of the surge force coefficient

Total Uncertainty - Resistance Coefficient (95% Confidence)			
Uncertainty	Symbol	Value	%Cd
Multiple Sample Total Uncertainty	U_{CTM}	4.35E-05	10.44
Multiple Sample Total Uncertainty	U_{CTS}	4.48E-05	10.75

APPENDIX C

Publication

1. Mat Saad, KA, Ranmuthugala, D, Duffy, J and Leong, ZQ, 'The hydrodynamic effects on an underwater vehicle in close proximity to a larger moving vehicle', *11th Int Naval Engineering Conference and Exhibition*, 15-17 May 2012, Edinburgh, UK, pp. 1-13. (2012) [Refereed]

2. Leong, ZQ, Mat Saad, KA, Ranmuthugala, D, and Duffy, JT, 'Investigation into the Hydrodynamic Interaction Effects on an AUV Operating Close to a Submarine', *Proceedings of the Pacific 2013 International Maritime Conference*, 7-9 October 2013, Darling Harbour, Australia, pp. 1-11. (2013) [Refereed]